Study of Local Solid Volume Fraction Fluctuations in a Liquid Fluidized Bed

by

Maedeh Marefatallah

A thesis submitted in partial fulfillment of the requirements for the degree of

Doctor of Philosophy

in

Chemical Engineering

Department of Chemical and Materials Engineering
University of Alberta

Abstract

This research aimed to investigate the local dynamic behaviour of solid–liquid mixtures through measurements of one of the important dynamic parameters of liquid fluidized beds: local solid volume fraction fluctuations. These experimental results will enhance the understanding of important interactions in a solid–liquid multiphase system: particle–particle, particle–fluid, and particle–wall interactions.

Spatially resolved experimental measurements were made using a high-speed electrical impedance tomography system combined with signal processing techniques. The important advantage of this technique over other measurement methods such as optical techniques is that it can produce reliable results even at the high solid volume fractions, e.g. values close to the maximum packing concentration, even for opaque systems.

In this study solid volume fraction fluctuations of different solid particles in a liquid fluidized bed were measured: mono-sized spherical Delrin, nylon, glass, and steel particles and water was the fluidizing medium. A wide range of particle Stokes numbers ($94 \leq St \leq 3809$) was tested by selecting specific particle sizes and densities. The results were compared with previous experimental studies. Previous works measured only cross-sectional averages of the fluctuations. Therefore, for comparison the local measurements of this study were spatially averaged. The comparison showed an acceptable agreement in the level of Root Mean Square (RMS) fluctuations. Importantly, this study found that: (1) The strongest fluctuations always occurred at a narrow strip by the bed wall. Moving from the wall region towards the bed center, the magnitude of RMS fluctuations decreased. (2) The magnitude of local fluctuations was linked to

the particle Stokes number (St), such that, at any given radial position, the RMS fluctuations increased by increasing St. However, the shapes of the local RMS profiles did not change significantly with St. (3) Only limited agreement was observed among the trends of the measurements and the predictions of four existing mathematical and semi-empirical models.

Furthermore, the solid fraction fluctuations obtained in the liquid fluidized bed were analyzed in both the time and frequency domains. Power spectra analysis showed that by moving from the center of the bed to the wall region the slopes and profiles of power spectra do not change significantly. However, the amplitude increases over the whole frequency domain. The slopes of decay in power spectra revealed a two-dimensional turbulent flow coexisting with an external force. Further analysis confirmed that this external force is associated with void fraction waves traveling in the bed. Results obtained over a wide range of bulk solid fractions showed that the dominant frequency of these waves decreases with increasing solid fraction. Local experimental data presented in this study enhance the understanding of the small- and large-scale fluctuations in a solid–liquid fluidized bed.

Unlike the previous studies which were limited to cross-sectional-averaged values, this study provides experimental data with a higher spatial resolution. This local information not only can be used to examine the current mathematical models but also can validate and improve computational models of liquid fluidization. This will enhance the current simulation works of two-phase systems and thus multiphase flows in general.

Preface

All the experimental design, data collection, and data analysis conducted in this thesis (Chapter 2, 3, and 4) are my original work, as well as the literature review in Chapter 1. Parts of the technical apparatus used for data collection in this thesis (Chapter 2, 3 and 4) was refurbished and modified by me with the assistance of Dr. Sean Sanders.

Chapter 2 of this thesis is published as Marefatallah, M., Breakey, D., and Sanders, R.S. (2019). Study of local solid volume fraction fluctuations using high speed electrical impedance tomography: Particles with low Stokes number. Chem. Eng. Sci. *203*, 439–449. https://doi.org/10.1016/j.ces.2019.03.075

Chapter 3 of this thesis is in preparation for submission as Marefatallah, M., Breakey, D., and Sanders, R.S. (2019). Experimental Study of Local Solid Volume Fraction Fluctuations in a Liquid Fluidized Bed: Particles with a wide range of Stokes numbers.

Chapter 4 of this thesis is in preparation for submission as Marefatallah, M., Breakey, D., and Sanders, R.S. (2019). Spectral Analysis of Local Solid Volume Fraction Fluctuations in Fluidization of Particles with Low and High Stokes numbers: An Experimental Study.

For Chapter 2, 3, and 4, I was responsible for drafting the articles' manuscripts and Dr. David Breakey assisted with the data interpretation and manuscript edits. Dr. Sean Sanders was the supervisory author and was involved with concept formation and manuscript composition.

Dedication

To Amirali

Acknowledgements

First, I would like to thank Dr. Sean Sanders, my supervisor, for the encouragements, guidance, and support he provided me with throughout my PhD program. I am grateful to him for all the opportunities he made possible for me during these years that allowed me to expand my knowledge in new fascinating areas of research and also my academic and teaching experience. During the semesters that I had the opportunity to work as the teaching assistant for his undergraduate fluid mechanics course I learnt how to communicate with students and how to transfer knowledge to the next generation of engineers while keeping them interested in the course materials.

I want to thank Dr. David Breakey for his fresh ideas and great insights on the data interpretations of this work and for the time he spent in our very long meetings to discuss the fundamental ideas behind my research. I wish him great success in his career path as a young researcher. I believe we need more passionate scientists like him in academia who are willing to help their peers grow.

I also would like to thank Dr. Jean-Sébastien Kroll-Rabotin for his friendship and great discussions we had at the beginning of my PhD program. I learnt a lot from him over the time he spent as a post-doctoral fellow in our research group at the U of A. I always admired his knowledge of the physics and fundamentals of the chemical engineering processes.

I want to thank Simon (Yijia) Sun and Aref Fozooni for their assistance with my experiments in the lab. Also, thanks to my other colleagues in the Pipeline Transport Process (PTP) Research Group for their valuable feedbacks on my research work, especially Ameneh Shokrollahzadeh, Yogesh Agrawal, Nitish Ranjan Sarker, Rouholluh Shokri, and Cesar Montilla Perez. Special thanks to Terry Runyon for her continuous help throughout my years as a graduate student at the U of A.

Sincere thanks to Dr. Olivier Masbernat, the external examiner of my PhD defense, who travelled all the way from France to Canada to attend my PhD defense. His insights, comments and suggestions on my work were extremely valuable to me and I am grateful that I had this opportunity to meet him in person and discuss my research work with him.

I would like to acknowledge the Natural Sciences and Engineering Research Council of Canada (NSERC), Canadian Natural Resources Limited, Nexen Inc., Paterson & Cooke Canada Inc., Shell Canada Energy, Saskatchewan Research Council, Suncor Energy Inc., Syncrude Canada Ltd., Teck Resources Ltd., and Total American Services through the NSERC Industrial Chair in Pipeline Transport Processes for funding this project.

Finally, I would like to express my deepest appreciation to my husband, Amirali; without his continuous support and encouragements I would not have been able to travel this journey and accomplish this goal. I am also deeply grateful to my brother, Mahdi, and my parents who always believed in me and supported me during the difficult moments.

Table of Contents

List of Tables

List of Figures

Chapter 1. Introduction and Background

1.1. Introduction

Multiphase flow is a term referring to a flow system where two or more phases are present. Multiphase flows are widely used in different industrial processes ranging from oil and gas to food and pharmaceutical processes (Gidaspow, 1994; Kremer and Hancock, 2006; Xia and Sun, 2002). Flow behaviour prediction is important in the design, process control, and troubleshooting of these processes (Gidaspow, 1994). Over the past few decades, researchers have tried different approaches to model complicated multiphase flow systems, an example being the mixture that is extracted from oil wells and transported to a central processing plant using pipelines. This mixture typically consists of oil, gas, water, and in some cases sands and clay materials (Sanders et al., 2000). An important step towards modeling these multiphase systems is modeling a simpler case of two-phase flow, such as solid–liquid systems where particles represent the dispersed phase and the continuous phase is a Newtonian liquid. Solid–liquid systems are seen in many industrial situations such as sediments in water (Drew, 1983), solid–liquid industrial separation in hydrocyclones (Tarleton and Wakeman, 2005), and thickening of clay suspensions in oil sands tailings management (Masliyah et al., 2004).

Solid–liquid fluidized beds

A common example of a solid–liquid system is the liquid fluidized bed. Fluidization is known as an operation involving solid particle suspension in a fluid carrier (Kechroud et al., 2010). A fluidized bed is usually a circular vessel in which solid particles are placed. Underneath the particles is a mesh plate (distributor) which holds the particles in place and lets the fluid flow pass through. Fluid (in this case liquid) is then pumped upward through the bed. The liquid flow results in a frictional pressure drop over the bed of solid particles (Gidaspow, 1994). By increasing the liquid flowrate, the “minimum fluidization” condition is reached, at which point the fluid flow can support the weight of the particles in the bed (Gidaspow, 1994). By further increase in the liquid flowrate, the bed expands, and a fluidization state in which particles are fully suspended in the fluid is reached.

The combination of the turbulent fluid flow and trapped particles in a fluidized bed results in a high level of mixing. This makes fluidized beds the process unit of choice for industrial process designs when effective heat and/or mass transfer is required. Examples of these industrial processes are liquid-fluidized bed heat exchangers, adsorption, mineral extraction, and biochemical reactors (Epstein, 2002).

Although liquid fluidization is widely used in different industrial units, many aspects of its flow behaviour and important interactions are still not fully known. Therefore, fluidized beds are currently mostly being operated based on empirical methods (Zhang et al., 2012). Development of reliable models that can be used in the design and operation of these systems requires more insight into particle–particle, particle–fluid and particle–wall interactions and their relative dominance at different operating conditions. Furthermore, local instantaneous experimental measurements of dynamic parameters of the system are required to validate such models. Example of these parameters are volume fractions and velocities of both solid and liquid phases.

Beyond their industrial applications, fluidized beds provide ideal conditions to study the dynamic behaviour of solid–liquid systems because they can operate over a wide range of particle and fluid properties (e.g. solid volume fraction, solid density, and fluid viscosity). Specifically particle–particle, particle–fluid, and particle–wall interactions can be investigated by studying liquid fluidized beds (Gevrin et al., 2008). There are numerous studies that employed fluidized beds to investigate the dynamic behaviour of multiphase flow (especially solid–liquid) systems (Gevrin et al., 2008; Hashemi, 2013; Kechroud et al., 2010; Zenit and Hunt, 2000; Zenit et al., 1997). Similar to these works, this project aims to use a fluidized bed as a case study to provide more insights into one of the important dynamic parameters of solid–liquid flows: solid phase volume fraction.

1.1.1. Research objectives

This work aims to provide local experimental measurements of solid fraction fluctuations in a liquid fluidized bed over a wide range of solid properties and fluidization conditions. The local measurements of the fluctuations of solid phase fraction in a liquid fluidized bed will enhance our knowledge about the particle–particle, particle–fluid and particle–wall interactions. These

interactions are important keys to understand flow behavior not only in a liquid fluidized bed but also in other two-phase flow systems such as particle-laden turbulent flows. Furthermore, these measurements will provide information that can be used for validation of computational models. To our knowledge, all the experimental measurements of the solid fraction fluctuations in a liquid fluidized bed are cross-sectional average values and no information about the local magnitude of these fluctuations has been provided in the literature.

1.1.2. Thesis outline

The outline of the remainder of this thesis is provided below:

Chapter 2. Study of Local Solid Volume Fraction Fluctuations Using High Speed Electrical Impedance Tomography: Particles with Low Stokes Number

In the first phase of this thesis project we conducted measurements of the local solid volume fraction fluctuations for Delrin spherical particles with a low Stokes number. The experimental setup used by Hashemi (2013) was refurbished, modified and improved in this phase.

The results of this chapter, along with earlier work by Hashemi (2013) showed that the distribution of the fluctuations was non-uniform along the bed cross-section. In addition, the preliminary analysis of the power spectra done in this phase of the research showed that there appears to be a relationship between the bulk solid volume fraction and the structure of the turbulent flow (2D vs 3D) in the fluidized bed. Results showed that further measurements were needed at lower frequency ranges to fully capture this relationship – which were then made and reported in Chapter 4

Chapter 3. Experimental Study of Local Solid Volume Fraction Fluctuations in a Liquid Fluidized Bed: Particles with a wide range of Stokes numbers

This chapter shows the experimental measurements conducted on three additional particle types: nylon, glass, and steel. The results of this chapter, along with those presented in Chapter 2 cover a wide range of particle Stokes numbers ($94 \leq St \leq 3809$). The local Root Mean Square (RMS) of solid fraction fluctuations are presented and compared with existing models. Results of

this chapter show that the magnitude of the local solid volume fraction fluctuations is dependent on the particle properties, especially particle Stokes number. Since none of the existing models considers particle properties, the values predicted by these models do not match the measurements.

Chapter 4. Spectral Analysis of Local Solid Volume Fraction Fluctuations in Fluidization of Particles with Low and High Stokes numbers: An Experimental Study

In this chapter, local measurements were further analyzed in the frequency- and time-domains. Frequency-domain information enhances understanding of the nature of the small- and large-scale fluctuations.

Results of this chapter expanded our knowledge about the fluctuations at different locations in the bed, i.e. medium to high-frequency fluctuations had significantly higher amplitudes at the near- wall region. Furthermore, the power spectra analysis suggested that by increasing the bulk solid fraction the flow in the fluidized bed behaves more like a 2D turbulent flow. This 2D flow is a result of 3D flow combined with an external force, i.e. instability void fraction waves.

1.2. Background

In this section, a review of the studies on different dynamic parameters in a fluidization system is provided. Additionally, different techniques that have been used to measure phase volume fractions in two-phase flow systems are reviewed. After discussing the outcomes of some of the more important experimental works in which solid volume fraction in a fluidized bed were measured, the models that predict this parameter are also reviewed.

1.2.1. Dynamic parameters in fluidized beds

Many researchers have conducted experimental and/or numerical studies of solid–liquid fluidized beds and have, in particular, examined the parameters that determine the dynamics of the dispersed and continuous phases (Gevrin et al., 2008; Hashemi, 2013; Kechroud et al., 2010; Zenit and Hunt, 2000; Zenit et al., 1997). Some of these important parameters, including liquid

velocity fluctuations and solid volume fraction fluctuations are described in greater detail in this section.

Kinetic Theory of Granular Flow (KTGF)

The kinetic theory of granular flow is an approach in modeling of solid–fluid flow systems using the main concepts and expressions involved in the kinetic theory of dense gases (Huilin et al., 2001). In the last sixty years, the application of kinetic theory of dense gases to solid suspensions was studied by many researchers, see for example Gidaspow et al. (2004) and Huilin et al. (2001) for an overview.

One of the important parameters involved in the modeling of two-phase solid–fluid systems is the solid phase pressure. There are many theoretical models developed to predict solid phase pressure in a two-phase system based on KTGF (Batchelor, 1988; Buyevich and Kapbasov, 1994; Gidaspow, 1994; Koch, 1990). These models involve parameters related to the properties of both solid and liquid phases. In addition to the solid phase volume fraction and fluid phase velocity, there are three important parameters which capture the similarities and differences between the solid–fluid system and a dense gas system: granular temperature, radial distribution function, and coefficient of restitution. These three parameters are usually defined based on solid phase volume fraction or velocity (Batchelor, 1988; Campbell, 2006; Gidaspow et al., 2004; Koch, 1990).

The comparison between the predictions of KTGF based models show that these models predict a very wide range of particle pressures and very different values for any given condition (Zenit et al., 1997). Also, none of the models are able to predict the available experimental values (Zenit et al., 1997). These findings suggest that development of a model that can predict particle pressure over the wide range of bulk solid fraction is still required. To do so, direct measurement of the particle pressure, along with other dynamic parameters that contribute to the theoretical models, is required. These parameters include fluctuations of volume fractions and velocities of both liquid and solid phases. Two of these parameters are discussed in the following section: continuous phase velocity fluctuations and solid fraction fluctuations.

Continuous phase velocity fluctuations

In a liquid fluidized bed, both phases are involved in vigorous fluctuating motion, which results in fluctuations in volume fraction and velocity of both the solid and liquid phases (Buyevich and Kapbasov, 1994; Zenit and Hunt, 2000). The frequency and magnitude of these fluctuations are important for optimal design, good process control, and also for a realistic simulation of liquid fluidized beds (Kechroud et al., 2010). Examples of parameters obtained from simulations include the solid and liquid mass and heat transfer, and granular pressure in the bed (Del Pozo et al., 1993; Zenit and Hunt, 2000). The focus of this section is on the experimental measurement and modeling of the continuous phase velocity fluctuations.

Kechroud et al. (2010) studied continuous phase velocity fluctuations in a solid–liquid fluidized bed. They conducted their measurements above the top of a fluidized bed and used glass particles with different particle sizes (Kechroud et al., 2010). Their results showed that the amplitude of liquid velocity fluctuation increased as the particle diameter increased. In addition, the solid fraction affected the liquid velocity fluctuations. The RMS of axial liquid velocity fluctuations reached its maximum value at the bed void fraction of 0.7. The RMS of axial liquid velocity fluctuations reached zero at high solid volume fractions. The comparison between their results and the limited experimental results available in the literature showed good agreement between the results of the measurements conducted inside the bed with the ones obtained from the measurements at the top of the bed (Kechroud et al., 2010).

In addition, Kechroud et al. (2010) provided a hypothesis that there is a strong relationship between the solid volume fraction and liquid velocity fluctuations in a liquid fluidized bed. This hypothesis was made based on the comparison between their results and the solid volume fraction fluctuations measured by Zenit and Hunt (2000). This comparison showed a high degree of similarity between the trends of both fluctuations vs. bulk solid fraction in the bed (Kechroud et al., 2010). Hashemi (2013) also confirmed the above-mentioned hypothesis by comparison between his results of solid fraction fluctuations for 2 mm and 4 mm glass beads with liquid velocity fluctuations measurements made by Kechroud et al. (2010). At the present time, it is not known if these two fluctuating components are always directly correlated; and the conditions

over which the two are correlated will require further investigation. Such investigations are outside of the scope of this study.

Solid volume fraction fluctuations

The magnitude of solid volume fraction fluctuations is one of the important parameters involved in Computational Fluid Dynamics (CFD) modeling of two-phase flow systems. Many CFD simulations of liquid fluidized beds (Cheng and Zhu, 2005; Cornelissen et al., 2007; Doroodchi et al., 2005; Gevrin et al., 2010; Lettieri et al., 2006; Roy and Dudukovic, 2001; Zhang et al., 2012) use a two-dimensional Eulerian-averaged approach using models based on KTFG. In these simulations, there are important local parameters involved in a closed set of equations (including the equations for continuity and momentum transport). These parameters are the local volume fractions and velocities of both the solid and liquid phases, all of which undergo fluctuations. Among these parameters, the study of the fluctuating component of the solid fraction is important for the following reasons:

1. The magnitude of solid fraction fluctuation has a strong relationship with the interphase interaction force per particle (Buyevich, 1997). This force is responsible for the small-scale random fluctuations (Buyevich, 1997) which are in turn the main reason why the heat and mass transfer rates are high in a fluidized bed (Buyevich and Kapbasov, 1994).

2. There is a close relationship between local fluctuating solid fraction and fluctuating fluid velocity (related to the granular temperature and fluctuating kinetic energy of the solid phase) (Gevrin et al., 2008). Therefore, models predicting the fluctuating component of the solid fraction can contribute to the assessment of the proper closure laws for equations of conservations in an Eulerian-Eulerian model (Buyevich and Kapbasov, 1994; Derksen and Sundaresan, 2007; Hrenya and Sinclair; van Wachem and Almstedt, 2003).

3. In CFD simulations, important assumptions are made related to the boundary conditions (e.g. uniformity of the flow at the entrance of the bed (Cornelissen et al., 2007)), the models chosen for interphase momentum transfer (which are empirical-based

drag laws (Reddy and Joshi, 2009)), the equations chosen for the radial distribution function, and the values assigned to parameters such as coefficients of restitution. Local instantaneous measurements solid volume fraction, for example, are required to examine and validate these assumptions for different system designs and operating conditions. The ability to benchmark CFD simulations against experimental measurements of fluctuating parameters will improve the CFD models of solid–liquid systems and therefore will improve modeling of multiphase flows in general (Cornelissen et al., 2007).

As described above, the study of the solid volume fraction fluctuations will enhance our knowledge about solid–liquid interactions in a liquid fluidize bed. This knowledge is an essential key for development of models that can capture solid–liquid flow behaviour. Experimental measurements also can be used to validate simulations of liquid fluidized beds. Experimental studies and modeling that have measured and predicted solid fraction fluctuations are discussed in detail in Section 1.2.2.

1.2.2. Solid phase volume fraction: measurements and models

In this section, measurement techniques that have been used for the phase (solid or fluid) volume fraction in two-phase flow systems are reviewed. We also reviewed the models that aim to predict solid volume fraction fluctuations in a fluidized bed. The measurements of the local solid fraction fluctuations made in this study can be used to examine these models.

Two-phase flow measurement techniques

Over the years different techniques have been employed to measure phase fractions in two-phase flows (both solid volume fraction and “void” fraction, aka. the continuous phase). Most of these measurements were conducted on gas-solid systems (Issangya et al., 2000). For the measurement of the void fraction fluctuations, different techniques such as fiber optic probes, X-ray, and gamma ray imaging, static pressure transducers, high-speed video imaging, capacitance sensors, and resistance or conductance probes have been used (Costigan and Whalley, 1997; Issangya et al., 2000; Jones and Delhaye, 1976; Lowe and Rezkallah, 1999). In a

few experimental works conducted on solid–liquid systems, some of the above-mentioned techniques were also applied (Kato et al., 1981; Renganathan and Krishnaiah, 2005; Ishida and Tanaka, 1982; Limtrakul et al., 2005; Yamazaki et al., 1992; Kumar et al., 1996; Lee and Lasa, 1987). The methods used in these studies, however, were either limited to cross-sectional averaged measurements (Kato et al., 1981; Lee and Lasa, 1987; Renganathan and Krishnaiah, 2005), dilute suspensions (Ishida and Tanaka, 1982), or suspensions of fine, micron-sized particles (Yamazaki et al., 1992). In the studies measuring local solid fraction (Kumar et al., 1996; Yamazaki et al., 1992), the methods were either limited to time-averaged instead of instantaneous measurements (Kumar et al., 1996) or were complicated by the need for strict safety precautions (in the case of gamma ray radiation) which are costly (Kumar et al., 1996). Lastly, the measurements using fiber optic probes are relatively invasive, as the local measurements require the probe to travel through the suspension (Yamazaki et al., 1992)

Measurements of solid fraction fluctuations in a liquid fluidized bed

The first study that measured the solid fraction fluctuations in a liquid fluidized bed used a non-invasive optical technique (light transmission, photography and videotape) (Didwania and Homsy, 1981). The purpose of this study was to quantify different flow regimes in a solid–liquid fluidized bed (Didwania and Homsy, 1981). Unfortunately, their reported measurements for the magnitude of the fluctuations were limited (i.e. $\overline{\mathrm{C}} \geq 0.44$).

Zenit and Hunt (2000) conducted extensive measurements of the solid fraction fluctuations in a solid–liquid fluidized bed for different particle sizes and densities over a range of solid volume fractions. They used an impedance volume-fraction meter (IVFM) to measure the fluctuations (Zenit and Hunt, 2000). IVFM is a non-invasive technique, but it only provides a cross-sectional average of the instantaneous solid fractions (Zenit and Hunt, 2000) and does not provide any local information regarding the fluctuations. Their results showed that the RMS solid fraction fluctuation is a function of bulk solid fraction and particle properties, especially particle Stokes number. Stokes number definitions are described in greater detail in the following section. The RMS solid fraction fluctuation increases when the bulk solid volume fraction is increased, having

a local and an overall maximum around 30% and 45%. At high bulk solid volume fractions ($0.45 \leq \overline{C}$) increasing $\overline{C}$ resulted in lower values of RMS fluctuations.

Zenit and Hunt (2000) compared their experimental results with the mathematical model of Buyevich & Kapbasov (1994). The predicted trend and shape of the changes in RMS solid fraction fluctuations agreed with Zenit and Hunt's (2000) results but the absolute value of fluctuations was over-predicted by the model. In addition, based on the model of Buyevich & Kapbasov (1994), the solid fraction fluctuations are not a function of particle properties. However, the particle diameter and density clearly affect the magnitude of fluctuations, as demonstrated in the experimental results of Zenit and Hunt (2000), whose results showed that the differences between predicted and measured values increase as the particle Stokes number decreases.

Particle Stokes number

Many researchers have described the different mechanisms that contribute to the production of solid fraction fluctuations. These mechanisms are: particle–fluid interactions, direct particle collisions (Abbas et al., 2010; Buyevich and Kapbasov, 1994), and particle–wall interactions (Hashemi, 2013). Based on these findings it is clear that there is a complex competition among the contributions of different mechanisms in the suspension dynamics (Gevrin et al., 2008). Furthermore, based on the results obtained by Zenit and Hunt (2000), the main mechanism responsible for fluctuations can vary depending on the fluidization conditions and particle properties. Therefore, the dominance of each phenomenon at different system conditions needs to be investigated. Beside the importance of solid fraction, particle inertia is a determining factor in predicting the relative contributions of fluid–particle and particle–particle interactions (Gevrin et al., 2008). Particle inertia can be characterized using the particle Stokes number (Abbas et al., 2010). This dimensionless number compares the particle relaxation time and the fluid characteristic time scale (Abbas et al., 2010):

$$\mathrm{St} = \frac{\tau_p}{\tau_f} \tag{1.1}$$

The particle relaxation time (τ_p) and fluid time scale (τ_f) can have different definitions based on the flow regimes, system configurations, and the length scales of fluid field of the interest. This results in many different definitions for the Stokes number. Some examples of Stokes numbers used in the literature are:

$$St_s = \frac{1}{18}\frac{\rho_s}{\rho_f}\left(\frac{d_p}{\eta}\right)^2 \tag{1.2}$$

where ρ_s, ρ_f, d_p, and η are solid density, fluid density, particle size, and Kolmogorov length scale (Hashemi et al., 2014). This Stokes number includes the fluid turbulent length scale with which the suspended particles primarily interact (Hashemi et al., 2014).

Ozel et al. (2017) defined Stokes number to account for the Non-Stokesian drag regime:

$$St_t = \frac{8\rho_s}{3\rho_f C_{Dt}} \tag{1.3}$$

where C_{Dt} is drag coefficient of a single particle at the particle terminal settling velocity.

Another definition for the particle Stokes number is defined based on terminal settling velocity and can be expressed as (Zenit and Hunt, 2000):

$$St_t = \frac{\rho_s}{\rho_f}\frac{Re_t}{9} \tag{1.4}$$

where Re_t is the particle Reynolds number at the particle's terminal settling velocity (Zenit and Hunt, 2000):

$$Re_t = \frac{\rho_f u_t d_p}{\mu_f} \tag{1.5}$$

where u_t is the particle terminal velocity. This Stokes number is scaled to the mean slip velocity. In the current study the definition of Stokes number provided in Eqn 1.4 is used since this is the definition used by other researchers who studied solid volume fraction fluctuations in a liquid fluidized bed (Gevrin et al., 2010; Zenit and Hunt, 2000). We reported this Stokes number for the particles used in this study so the results can be compared with the available data from the

literature. However, this definition of the Stokes number might not be the best choice to describe the particle–fluid interactions in a fluidization system. For example if the particle Reynolds number changes significantly, this Stokes number might not be able to capture the impact of the turbulent kinetic energy at high particle Reynolds numbers in comparison with the pseudo-turbulence caused by the particle agitations in the fluid phase (Fox, 2014).

At very high particle inertia ($\mathrm{St_t} \rightarrow \infty$), the suspension behaves like a dry particle system in which the trajectories of particles are not affected by fluid flow (Abbas et al., 2010). It is predicted that at these conditions, the dominant mechanism responsible for solid fraction fluctuations is direct particle collisions (Zenit and Hunt, 2000). On the other hand, since the strength of particle collisions decreases when the particle inertia decreases (Zenit and Hunt, 1999), at low particle Stokes numbers, the effect of the interstitial fluid and viscous drag becomes important (Gevrin et al., 2008; Zenit and Hunt, 2000).

In addition to determining the main mechanism responsible for fluctuations, the particle and fluid properties will dictate the magnitude of these fluctuations. The very few works done to investigate the parameters influencing the magnitudes of the fluctuations show that particle diameter and density (particle Stokes number) have an important effect (Gevrin et al., 2008; Hashemi, 2013; Zenit and Hunt, 2000; Zenit et al., 1997), along with solid fraction.

The two studies discussed in this section (Didwania and Homsy, 1981; Zenit and Hunt, 2000) were limited to the cross-sectional average of the solid fraction fluctuations. In order to fully capture the nature of the fluctuations in a fluidized bed, there is still a need to measure these fluctuations at different radial positions.

Local measurement of solid fraction fluctuations in a liquid fluidized bed

Preliminary measurements of the local solid fraction fluctuations in a liquid fluidized bed were made by Hashemi (2013) for three sizes of spherical glass particles (2, 3 and 4 mm). He used Electrical Impedance Tomography (EIT) for his measurements. The main advantage of the EIT technique compared to the methods discussed earlier is that it can operate on concentrated and

even opaque suspensions. Furthermore, unlike measurement techniques involving ionizing radiation, EIT does not require the same level of safety precautions for its use.

The solid fraction and volume fraction fluctuations maps for different particle sizes and different bulk solid fraction showed that the magnitude of fluctuations is higher near the bed wall (Hashemi, 2013). Hashemi suggested two underlying reasons for the increase in the magnitude of fluctuations near the wall: particle–wall collisions and the higher shear experienced by particles in this region (Hashemi, 2013). Furthermore, the cross-sectional-averaged solid fraction fluctuations results of Hashemi's (2013) study showed good agreement with the results of Zenit and Hunt (2000) over a wide range of solid fractions.

Electrical impedance tomography

Electrical Impedance Tomography (EIT) is an imaging technique which is based on measurements of a mixture's electrical impedance using an array of sensors. One of the applications of this technique is solid fraction measurement which is derived from the measured impedance using Maxwell's equations (Dyakowski et al., 2000). Numerous researchers have used electrical tomography methods to measure different parameters in multiphase flow systems (Azzi et al., 2010; Azzopardi et al., 2008; Bolton et al., 2004; Fangary et al., 1998; Zhu et al., 2003). Electrical tomography is a relatively fast, robust and non-invasive method (Dyakowski et al., 2000). In addition, one of the important advantages of electrical tomography is that it is not dependent on the optical properties of the suspension (Norman and Bonnecaze, 2005).

Since the goal of this project is to study the dynamic behaviour of a solid–fluid flow, an Industrial Tomography System (ITS) Z8000 EIT system was used. This instrument consists of a ring of sensors in which the electrodes are located at equal intervals around the bed periphery. Electrical current is induced between one pair of adjacent electrodes and then the differential potentials between all remaining pairs of neighboring electrodes are measured (see Figure 1.2). This procedure is repeated for all pairs of adjacent electrodes (Dyakowski et al., 2000).

From the differential potential measurements a resistivity (and conductivity) map can be reconstructed. In this study, the Modified Sensitivity Back-Projection (MSBP) reconstruction

algorithm has been used (Industrial Tomography Systems, 2014). MSBP uses a nonlinear approximation to reconstruct the conductivity map from the voltage measurements obtained by EIT (i.e. conductivity is inversely related to voltage) (Jia et al., 2014). This program is commercially available and built into the ITS processing unit. The ITS z8000 tomography unit and its principles of operation are explained in detail elsewhere (Jia et al., 2014; Wang, 2002; Wei et al., 2015).

After obtaining the resistivity distribution maps from the voltage measurements, solid fraction maps are obtained from the conductivity distribution maps using Maxwell's equations (Dyakowski et al., 2000). The EIT mesh of the vessel's cross-section comprises 316 pixels of equal area. In each of pixel, the solid fraction can be measured. The resistivity maps are then converted to the solid fraction maps using the Maxwell equation (Dyakowski et al., 2000).

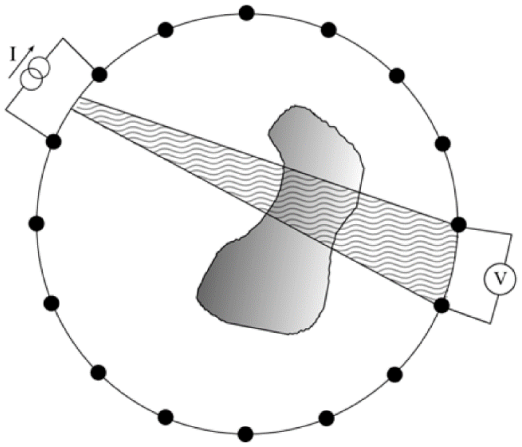

Figure 1.1. Schematic of the plane of sensors for an ERT system. Adapted from Dyakowski et al. (2000).

Models predicting solid volume fraction fluctuations in a fluidized bed

(Buyevich, 1971) proposed a simple model for the prediction of small-scale random fluctuations of the solid fraction based on the Lattice model of dispersed mono-sized spherical particles. The model is as follows:

$$\overline{C_r'^2} = \overline{C_r}^2 \left(1 - \frac{\overline{C_r}}{C_{max}}\right) \tag{1.6}$$

where C_r' is the fluctuating component of the local solid volume fraction, $\overline{C_r}$ is the local mean solid volume fraction, and C_{max} is solid volume fraction at the close-packed state. The main assumption of this model is that the system is macroscopically uniform. Therefore, this model will not be applicable to an unsteady state system or in the near-wall region (Buyevich, 1971). Buyevich and Kapbasov (1994) proposed two other models for the prediction of the local small-scale random solid fraction fluctuations in a fluidized bed. These mathematical models are developed based on the thermodynamic theory of fluctuations. Although more complicated than the first model (Eqn 1.6), they are still only a function of the local mean solid fraction of particles and the maximum packing concentration (C_{max}). The first model is based on Carnahan and Starling's (1969) model, i.e. equation of state for non-attracting rigid spheres:

$$\overline{C_r'^2} = \overline{C_r}^2 \left[1 + 2\overline{C}\frac{4-\overline{C_r}}{(1-\overline{C_r})^4}\right]^{-1} \tag{1.7}$$

Since Carnahan and Sterling's model is based on the chaotic behavior of gas molecules and is not necessarily applicable for the case of a mixture with a high concertation of particles, Buyevich and Kapbasov (1994) suggested an alternative model employing the Enskog model of dense gases (non-ideal gas equation of state) (Luo, 1998):

$$\overline{C_r'^2} = \overline{C_r}^2 \left[1 - \left(\frac{\overline{C_r}}{C_{max}}\right)^{1/3}\right]\left[1 + \frac{1}{3}\left(\frac{(\overline{C_r}/C_{max})^{1/3}}{1-(\overline{C_r}/C_{max})^{1/3}}\right)\right]^{-1} \tag{1.8}$$

The magnitudes of the fluctuations predicted by the models shown in Eqn 1.7 and 1.8 deviate significantly from each other at $\overline{C} \geq 0.45$. At a given bulk solid fraction, Eqn 1.6 predicts higher values of fluctuations compared to Eqns 1.7 and 1.8.

It is important to note the key assumptions applied in developing Eqns 1.7 and 1.8. The first is that the mixture is macroscopically uniform which is only valid for either the case of homogeneous fluidization or the homogenous (dense) regions of an inhomogeneous fluidization system. The second assumption is that momentum transfer occurs through direct particle–particle collisions and the fluctuations are almost isotropic. This limits the application of the

model to mixtures of relatively large particles (i.e these models are not valid for mixtures of fine particles or colloidal suspensions).

Gevrin et al. (2010) proposed a semi-empirical model to predict the fluctuations of the solid phase fraction. This model was based on another semi-empirical scaling law proposed in their previous work, which predicted the fluctuating kinetic energy of the solid phase as a function of bulk solid fraction (Gevrin et al., 2008):

$$\overline{q_p^2} \propto {u_t}^2 [C_{D0} \bar{C} \, (1 - \bar{C})^{-4.7} \,]^{2/3} \left(1 - \frac{\bar{C}}{C_{max}}\right)^{2nC_{max}} \tag{1.9}$$

where q_p^2 is the global (averaged over the volume) fluctuating kinetic energy of the solid phase, u_t is the particle terminal settling velocity, C_{D0} is Schiller and Nauman's drag coefficient (for a single particle and based on the slip velocity), $\bar{C}$ is the bulk solid volume fraction, and n is the Richardson-Zaki exponent. Eqn 1.9 was originally obtained based on a global energy balance for a fluidized bed. In the next step, the effect of particle collisions, especially at high solid fraction, was taken into account by replacing the vertical slip velocity with a characteristic velocity (the last term in the RHS of Eqn 1.9 arises from this consideration). Gevrin et al. (2008) also presented proportionality coefficients (for three types of particles) based on their simulation results for the fluctuating kinetic energy. In their later work, Gevrin et al. (2010) obtained the following equation based on the relationship between the solid fraction fluctuations and the fluctuating kinetic energy of the solid phase:

$$\overline{C'} \propto \frac{2[C_{D0} \bar{C} \, (1-\bar{C})^{-4.7} \,]^{1/3} \left(1 - \frac{\bar{C}}{C_{max}}\right)^{nC_{max}}}{3(n-1)(1-\bar{C})^{n-2}} \tag{1.10}$$

The main assumption for this model was that macroscopic relations such as the Richardson-Zaki equation are also valid at the local fine scale (Gevrin et al., 2010). This limits the applicability of this model to the homogenous fluidization systems.

The models shown in Eqns 1.6, 1.7, 1.8, and 1.10 need to be validated with experimental data of the local solid fraction fluctuations measured in a liquid fluidized bed. These measurements are

not easy to perform especially for dense and/or opaque suspensions (Derksen and Sundaresan, 2007).

1.2.3. Scope of the current study

This work aims to obtain local high quality experimental data of solid fraction fluctuations in a solid–liquid fluidized bed to further investigate the effects of particle diameter, particle density and bulk solid fraction on the magnitude of local solid fraction fluctuations. The experiments are designed to cover a wide range of particle Stokes numbers to allow for quantification of its effect on the magnitude of local solid fraction fluctuations.

The initial work by Hashemi (2013) was expanded to cover a wide range of particle Stokes numbers. Hashemi's work (2013) provided a good foundation for the study of local solid fraction and fraction fluctuations. However, his study was limited to glass beads with a narrow Stokes number range. In order to study the effect of particle Stokes number on the magnitude of local fluctuations, experiments were conducted using spherical particles with different particle density and sizes to cover a wide range of Stokes numbers. Table 1.1 summarizes the properties of particles used in different experimental studies of the dynamic behaviour of fluidized beds. Based on these works we designed our experiments to utilize a 10.16 cm fluidized bed and four particle types: Delrin, nylon, glass, and steel. Properties of these particles provided in the following chapters.

We used an industrial electrical impedance tomography (EIT) data acquisition system along with a dual-plane sensor to measure the solid fraction distributions in the fluidized bed. The EIT measures the instantaneous solid particles distribution map within the sensor plane. The local solid fraction fluctuations are then calculated based on the 8000 measurement frames.

1.2.4. Contribution of the present study

By reviewing the works done by different researchers to study the dynamic behavior of solid–liquid fluidized bed, we can come to some conclusions. First, there is a low level of understanding of the dynamic parameters of these systems. Huge differences exist between the predictions of

Table1.1. Summary of the properties of different particles and beds used in the literature for experimental studies of the dynamic behaviour of fluidized beds

Materials	d_p (mm)	D_{bed} (cm)	Measured parameter	References
Glass	2.06, 3.00, 3.96, 6.00	10.16, 5.08	Collisional particle pressure; solid volume fraction fluctuations	(Zenit et al., 1997), (Zenit and Hunt, 2000)
Glass	2.00, 4.00, 6.00, 8.00	9.3	Liquid velocity fluctuations	(Kechroud et al., 2010)
Glass	2.00, 3.00, 4.00	10.16	Local solid volume fraction fluctuations	(Hashemi, 2013)
Steel	4.50	10.16, 5.08	Collisional particle pressure; solid volume fraction fluctuations	(Zenit et al., 1997), (Zenit and Hunt, 2000)
Nylon	6.35	10.16, 5.08	Collisional particle pressure; solid volume fraction fluctuations	(Zenit et al., 1997), (Zenit and Hunt, 2000)
PVC rods	3.41*	10.16, 5.08	Collisional particle pressure; solid volume fraction fluctuations	(Zenit et al., 1997), (Zenit and Hunt, 2000)

*Equivalent diameter

important parameters such as the collisional particle pressure and the solid fraction fluctuations obtained from different models and the experimental measurements, both in terms of trends and magnitudes.

The experimental and numerical studies discussed in this chapter provided some insight into the behaviour of highly concentrated solid–liquid flows. However, most of the existing measurements were based on cross-sectional average parameters which give no local information of solid fraction or fraction fluctuations in the flow domain. Such local information is necessary, especially in determining the mechanism(s) responsible for generating solid fraction fluctuations (Hashemi, 2013).

The results of this study will provide new insight into the dynamic nature of highly concentrated solid–liquid flows. One of the significant differences between these results and the results obtained previously is that by means of the EIT method, we will be able to measure the local solid fraction fluctuations while all the existing experimental data are cross-sectional averaged parameters (except for Hashemi's work (2013) which was limited to one type of particle). The analysis of the local fluctuations in frequency- and time-domains will provide information about the mechanisms that produce these fluctuations. Furthermore, the results presented here expand the knowledge of the large- and small-scale fluctuations and their dominance at different fluidization conditions. In addition, the results can be used to validate the existing models for solid fraction fluctuations, e.g. Buyevich (1971), Buyevich and Kapbasov (1994), and Gevrin et al. (2010). To our knowledge, this is the first study that measures local volume fraction fluctuations for such a wide range of particle properties.

1.3. References

Abbas, M., Climent, E., Parmentier, J.-F., and Simonin, O. (2010). Flow of particles suspended in a sheared viscous fluid: Effects of finite inertia and inelastic collisions. AIChE J. *56*, 2523–2538.

Azzi, A., Azzopardi, B.J., Abdulkareem, N.H., Hilal, N., and Hunt, A. (2010). Study of fluidization using Electrical Capacitance Tomography. Proceedings of the 7th International Conference on Multiphase Flow ICMF 2010, (Florida, USA).

Azzopardi, B.J., Jackson, K., Robinson, J.P., Kaji, R., Byars, M., and Hunt, A. (2008). Fluctuations in dense phase pneumatic conveying of pulverised coal measured using electrical capacitance tomography. Chem. Eng. Sci. *63*, 2548–2558.

Batchelor, G.K. (1988). A new theory of the instability of a uniform fluidized bed. J Fluid Mech *193, 1988*, 75–110.

Bolton, G.T., Hooper, C.W., Mann, R., and Stitt, E.H. (2004). Flow distribution and velocity measurement in a radial flow fixed bed reactor using electrical resistance tomography. Chem. Eng. Sci. *59*, 1989–1997.

Buyevich, Yu.A. (1971). On the fluctuations of concentration in disperse systems The random number of particles in a fixed volume. Chem. Eng. Sci. *26*, 1195–1201.

Buyevich, Yu.A. (1997). Particulate pressure in monodisperse fluidized beds. Chem. Eng. Sci. *52*, 123–140.

Buyevich, Yu.A., and Kapbasov, Sh.K. (1994). Random fluctuations in a fluidized bed. Chem. Eng. Sci. *49*, 1229–1243.

Campbell, C.S. (2006). Granular material flows – An overview. Powder Technol. *162*, 208–229.

Carnahan, N.F., and Starling, K.E. (1969). Equation of State for Nonattracting Rigid Spheres. J. Chem. Phys. *51*, 635–636.

Cheng, Y., and Zhu, J.-X. (Jesse). (2005). CFD Modelling and Simulation of Hydrodynamics in Liquid-Solid Circulating Fluidized Beds. Can. J. Chem. Eng. *83*, 177–185.

Cornelissen, J.T., Taghipour, F., Escudié, R., Ellis, N., and Grace, J.R. (2007). CFD modelling of a liquid–solid fluidized bed. Chem. Eng. Sci. *62*, 6334–6348.

Costigan, G., and Whalley, P.B. (1997). Slug flow regime identification from dynamic void fraction measurements in vertical air-water flows. Int. J. Multiph. Flow *23*, 263–282.

Del Pozo, M., Briens, C.L., and Wild, G. (1993). Particle-particle collisions in liquid-solid and gas-liquid-solid fluidized beds. Chem. Eng. Sci. *48*, 3313–3319.

Derksen, J.J., and Sundaresan, S. (2007). Direct numerical simulations of dense suspensions: wave instabilities in liquid-fluidized beds. J. Fluid Mech. *587*.

Didwania, A.K., and Homsy, G.M. (1981). Flow regimes and flow transitions in liquid fluidized beds. Int. J. Multiph. Flow *7*, 563–580.

Doroodchi, E., Galvin, K.P., and Fletcher, D.F. (2005). The influence of inclined plates on expansion behaviour of solid suspensions in a liquid fluidised bed—a computational fluid dynamics study. Powder Technol. *156*, 1–7.

Drew, D.A. (1983). Mathematical Modeling of Two-Phase Flow. Annu. Rev. Fluid Mech. *15*, 261–291.

Dyakowski, T., Jeanmeure, L.F.C., and Jaworski, A.J. (2000). Applications of electrical tomography for gas-solids and liquid-solids flows-a review. Powder Technol. *112*, 174–192.

Epstein, N. (2002). Applications of Liquid-Solid Fluidization. Int. J. Chem. React. Eng. *1*, 1–16.

Fangary, Y.S., Williams, R.A., Neil, W.A., Bond, J., and Faulks, I. (1998). Application of electrical resistance tomography to detect deposition in hydraulic conveying systems. Powder Technol. *95*, 61–66.

Fox, R.O. (2014). On multiphase turbulence models for collisional fluid–particle flows. J. Fluid Mech. *742*, 368–424.

Gevrin, F., Masbernat, O., and Simonin, O. (2008). Granular pressure and particle velocity fluctuations prediction in liquid fluidized beds. Chem. Eng. Sci. *63*, 2450–2464.

Gevrin, F., Masbernat, O., and Simonin, O. (2010). Numerical study of solid–liquid fluidization dynamics. AIChE J. *56*, 2781–2794.

Gidaspow, D. (1994). Multiphase Flow and Fluidization: Continuum and Kinetic Theory Descriptions (Academic Press).

Gidaspow, D., Jung, J., and Singh, R.K. (2004). Hydrodynamics of fluidization using kinetic theory: an emerging paradigm. Powder Technol. *148*, 123–141.

Hashemi, S.A. (2013). Velocity and concentration fluctuations in concentrated solid-liquid flows. PhD thesis. University of Alberta.

Hashemi, S.A., Sadighian, A., Shah, S.I.A., and Sanders, R.S. (2014). Solid velocity and concentration fluctuations in highly concentrated liquid–solid (slurry) pipe flows. Int. J. Multiph. Flow *66*, 46–61.

Hrenya, C.M., and Sinclair, J.L. Effects of particle-phase turbulence in gas-solid flows. AIChE J. *43*, 853–869.

Huilin, L., Gidaspow, D., and Manger, E. (2001). Kinetic theory of fluidized binary granular mixtures. Phys. Rev. E *64*, 061301.

Industrial Tomography Systems (2014). ITS Tomography Toolsuite v7.32 User's manual (Manchester, UK: Industrial Tomography Systems Plc).

Ishida, M., and Tanaka, H. (1982). An optical probe to detect both bubbles and suspended particles in a three-phase fluidized bed. J. Chem. Eng. Jpn. *15*, 389–391.

Issangya, A.S., Grace, J.R., Bai, D., and Zhu, J. (2000). Further measurements of flow dynamics in a high-density circulating fluidized bed riser. Powder Technol. *111*, 104–113.

Jia, J., Wang, M., and Faraj, Y. (2014). Evaluation of EIT systems and algorithms for handling full void fraction range in two-phase flow measurement. Meas. Sci. Technol. *26*, 015305.

Jones, O.C., and Delhaye, J.-M. (1976). Transient and statistical measurement techniques for two-phase flows: A critical review. Int. J. Multiph. Flow *3*, 89–116.

Kato, Y., Uchida, K., Kago, T., and Morooka, S. (1981). Liquid holdup and heat transfer coefficient between bed and wall in liquid solid and gas-liquid-solid fluidized beds. Powder Technol. *28*, 173–179.

Kechroud, N., Brahimi, M., and Djati, A. (2010). Characterization of dynamic behaviour of the continuous phase in liquid fluidized bed. Powder Technol. *200*, 149–157.

Koch, D.L. (1990). Kinetic theory for a monodisperse gas-solid suspension. Phys. Fluids A *2*, 1711–1723.

Kremer, D.M., and Hancock, B.C. (2006). Process Simulation in the Pharmaceutical Industry: A Review of Some Basic Physical Models. J. Pharm. Sci. *95*, 517–529.

Kumar, S.B., Moslemian, D., and Dudukovic, M.P. (1996). A gamma-ray tomographic scanner for imaging voidage distribution in two-phase flow systems. Int. J. Multiph. Flow *22*, 108.

Lee, S.L.P., and Lasa, H.I. de (1987). Phase holdups in three-phase fluidized beds. AIChE J. *33*, 1359–1370.

Lettieri, P., Di Felice, R., Pacciani, R., and Owoyemi, O. (2006). CFD modelling of liquid fluidized beds in slugging mode. Powder Technol. *167*, 94–103.

Limtrakul, S., Chen, J., Ramachandran, P.A., and Duduković, M.P. (2005). Solids motion and holdup profiles in liquid fluidized beds. Chem. Eng. Sci. *60*, 1889–1900.

Lowe, D.C., and Rezkallah, K.S. (1999). Flow regime identification in microgravity two-phase flows using void fraction signals. Int. J. Multiph. Flow 25.

Luo, L.-S. (1998). Unified Theory of Lattice Boltzmann Models for Nonideal Gases. Phys. Rev. Lett. *81*, 1618–1621.

Masliyah, J., Zhou, Z.J., Xu, Z., Czarnecki, J., and Hamza, H. (2004). Understanding Water-Based Bitumen Extraction from Athabasca Oil Sands. Can. J. Chem. Eng. *82*, 628–654.

Norman, J.T., and Bonnecaze, R.T. (2005). Measurement of Solids Distribution in Suspension Flows using Electrical Resistance Tomography. Can. J. Chem. Eng. *83*, 24–36.

Ozel, A., Brändle de Motta, J.C., Abbas, M., Fede, P., Masbernat, O., Vincent, S., Estivalezes, J.-L., and Simonin, O. (2017). Particle resolved direct numerical simulation of a liquid–solid fluidized bed: Comparison with experimental data. Int. J. Multiph. Flow *89*, 228–240.

Reddy, R.K., and Joshi, J.B. (2009). CFD modeling of solid–liquid fluidized beds of mono and binary particle mixtures. Chem. Eng. Sci. *64*, 3641–3658.

Renganathan, T., and Krishnaiah, K. (2005). Voidage characteristics and prediction of bed expansion in liquid–solid inverse fluidized bed. Chem. Eng. Sci. *60*, 2545–2555.

Roy, S., and Dudukovic, M.P. (2001). Flow Mapping and Modeling of Liquid−Solid Risers. Ind. Eng. Chem. Res. *40*, 5440–5454.

Sanders, R.S., Ferre, A.L., Maciejewski, W.B., Gillies, R.G., and Shook, C.A. (2000). Bitumen effects on pipeline hydraulics during oil sand hydrotransport. Can. J. Chem. Eng. *78*, 731–742.

Tarleton, S., and Wakeman, R. (2005). Solid/ Liquid Separation: Principles of Industrial Filtration (Elsevier).

Van Wachem, B.G.M., and Almstedt, A.E. (2003). Methods for multiphase computational fluid dynamics. Chem. Eng. J. *96*, 81–98.

Wang, M. (2002). Inverse solutions for electrical impedance tomography based on conjugate gradients methods. Meas. Sci. Technol. *13*, 101–117.

Wei, K., Qiu, C., Soleimani, M., and Primrose, K. (2015). ITS Reconstruction Tool-Suite: An inverse algorithm package for industrial process tomography. Flow Meas. Instrum. *46*, 292–302.

Xia, B., and Sun, D.-W. (2002). Applications of computational fluid dynamics (CFD) in the food industry: a review. Comput. Electron. Agric. *34*, 5–24.

Yamazaki, H., Tojo, K., and Miyanami, K. (1992). Measurement of local solids concentration in a suspension by an optical method. Powder Technol. *70*, 93–96.

Zenit, R., and Hunt, M.L. (1999). Mechanics of Immersed Particle Collisions. J. Fluids Eng. *121*, 179.

Zenit, R., and Hunt, M.L. (2000). Solid fraction fluctuations in solid–liquid flows. Int. J. Multiph. Flow *26*, 763–781.

Zenit, R., Hunt, M.L., and Brennen, C.E. (1997). Collisional particle pressure measurements in solid-liquid flows. J. Fluid Mech. *353*, 261–283.

Zhang, K., Wu, G., Brandani, S., Chen, H., and Yang, Y. (2012). CFD simulation of dynamic characteristics in liquid–solid fluidized beds. Powder Technol. *227*, 104–110.

Zhu, K., Madhusudana Rao, S., Wang, C.-H., and Sundaresan, S. (2003). Electrical capacitance tomography measurements on vertical and inclined pneumatic conveying of granular solids. Chem. Eng. Sci. *58*, 4225–4245.

Chapter 2. Study of Local Solid Volume Fraction Fluctuations Using High Speed Electrical Impedance Tomography: Particles with Low Stokes Number

Material in this chapter has been published as:

Marefatallah, M., Breakey, D., and Sanders, R.S. (2019). Study of local solid volume fraction fluctuations using high speed electrical impedance tomography: Particles with low Stokes number. Chem. Eng. Sci. *203*, 439–449. https://doi.org/10.1016/j.ces.2019.03.075

2.1. Introduction

Solid–liquid fluidization can be found in a variety of industrial processes, such as liquid-fluidized-bed heat exchangers, classification and separation of particles, and as the technology of choice for many chemical- and bio-reactors (Epstein, 2002). An important advantage of fluidized beds that makes them favorable for many industrial processes is the intense mixing inside the bed, which results in effective heat and mass transfer (Buyevich and Kapbasov, 1994). In addition to these applications, liquid fluidized beds also represent interesting test cases to study the dynamic behaviour of two-phase solid–liquid flows. In particular, particle–particle and particle–fluid interactions can be studied over a wide range of solid volume fractions, particle sizes, shapes and densities (Gevrin et al., 2008).

The unsteady nature of a liquid fluidized bed results in fluctuations of the velocity and volume fraction of both the solid and liquid phases (Buyevich and Kapbasov, 1994; Zenit and Hunt, 2000). An understanding of the nature and magnitude of these fluctuations is necessary for a number of reasons. First, these fluctuations are the main cause of the high values of the mass and heat transfer coefficients in the fluidization process (Buyevich and Kapbasov, 1994), and the study of these fluctuations is important for the design, control, and troubleshooting of liquid fluidized beds (Kechroud et al., 2010). Second, solid fluctuation measurements are also needed to improve numerical simulations of fluidization processes. Additionally, the knowledge of velocity and volume fraction fluctuations can be used to better understand and characterize the dynamic behaviour of other solid–liquid systems, such as pipeline flows (Hashemi et al., 2014).

There are two categories of solid fraction fluctuations in a liquid fluidized bed (Buyevich and Kapbasov, 1994). The first consists of the large global fluctuations primarily resulting from the bulk bed behaviour, such as bubble formation and circulation within the bed. The second consists of the small-scale fluctuations that result from particle–particle collisions, particle–fluid interactions, and local hydrodynamics (driven by the arrangements of the nearby particles) (Buyevich and Kapbasov, 1994). While the large-scale fluctuations have been widely investigated in stability studies (Zenit and Hunt, 2000), there have been only a limited number of studies of

the small-scale fluctuations (Buyevich and Kapbasov, 1994; Didwania and Homsy, 1981; Gevrin et al., 2010; Hashemi, 2013; Zenit and Hunt, 2000).

A mathematical model for the small-scale solid fraction fluctuations, based on the thermodynamic theory of fluctuations, was proposed by (Buyevich and Kapbasov, 1994). This model was proposed primarily for macroscopically uniform dispersed beds. There were two main assumptions made in developing this model: that the main mechanism responsible for the momentum transfer is direct particle collisions and that the fluctuations in the bed are isotropic (Buyevich and Kapbasov, 1994). Zenit and Hunt (2000) conducted an extensive experimental study of the solid fraction fluctuations in a solid–liquid fluidized bed for different particle sizes and densities over a wide range of bulk solid fractions ($\overline{C}$). They used an impedance volume-fraction meter (IVFM) to measure the cross-sectional averaged solid fraction fluctuations (Zenit and Hunt, 2000). Although their results confirmed that the RMS of solid fraction fluctuations is a function of $\overline{C}$, as predicted by (Buyevich and Kapbasov, 1994), the magnitude of the fluctuations was lower than the predicted values for particles with relatively low densities. These results showed that the RMS of solid fraction fluctuations is not only a function of $\overline{C}$ but also of the particle properties, which were not considered in the aforementioned model. The difference between the magnitude of the fluctuations predicted by the model and the experimental data was greater for particles with low Stokes numbers, while fluctuations for large-Stokes-number particles (inertial particles) were in good agreement with the model predictions (Zenit and Hunt, 2000). The particle terminal Stokes number can be expressed as

$$St_t = \frac{\rho_s}{\rho_f}\frac{Re_t}{9} \tag{2.1}$$

where ρ_s and ρ_f are solid and fluid density, respectively, and Re_t is the particle Reynolds number at the particle terminal settling velocity (u_t):

$$Re_t = \frac{\rho_f u_t d_p}{\mu_f} \tag{2.2}$$

where d_p and μ_f are particle size and fluid viscosity, respectively.

A suspension of inertial particles behaves similarly to a dry particle system in which the particle trajectories are not affected by fluid flow (Abbas et al., 2010). Under these conditions, the assumption in the model that direct particle collisions are the dominant mechanism responsible for fluctuations is applicable (Zenit and Hunt, 2000). Zenit and Hunt's (2000) study revealed new insights concerning the nature of small-scale fluctuations but was limited to values averaged over the cross section (Zenit and Hunt, 2000). Gevrin et al., (2010) conducted numerical simulations of the dynamic behavior of a solid–liquid fluidized bed. Their two-dimensional (2D) simulations were based on the flow configurations and fluid and particle properties of the experimental work done by Zenit and Hunt (2000). Non-uniform structures of instantaneous solid fraction (horizontal stripes of high and low solid fraction regions, concentric zones of different solid fractions, and zigzag structures) were characterized in this study (Gevrin et al., 2010). Although the numerical data showed a non-uniform distribution of local solid fraction both in the vertical and radial directions, the results could be compared only with experimental results of values averaged over the bed cross section (Gevrin et al., 2010). More recently, Hashemi (2013) conducted an initial study of local solid fraction and its fluctuations using glass spheres with moderate Stokes numbers (ranging from 153 to 480). Using high-speed EIT, he obtained 2D instantaneous solid fraction maps over the bed cross section. The results showed that the magnitude of the fluctuations was highest near the bed wall due to the high shear zone at this region and particle–wall interactions (Hashemi, 2013).

The higher values for fluctuations in the near-wall region were observed for all particle sizes and bulk volume fractions tested (Hashemi, 2013). This non-uniform distribution of the solid fraction of instantaneous, local solid distributions implies that further investigation of instantaneous, local solid distributions is required, using different particle types so that a broad range of Stokes numbers can be tested.

Based on the studies conducted on small-scale fluctuations, it is evident that there is a complex and highly coupled competition among the contributions of different mechanisms, including particle–fluid interactions (Zenit and Hunt, 2000), direct particle collisions (Abbas et al., 2010; Buyevich and Kapbasov, 1994; Zenit and Hunt, 2000), and particle–wall interactions (Hashemi,

2013). Furthermore, the fluctuations can vary depending on the fluidization conditions and solid particle properties. Particle properties (i.e. Stokes number) not only play an important role in the competition among the mechanisms responsible for the fluctuations, but also dictate their magnitude (Gevrin et al., 2008; Hashemi, 2013; Zenit and Hunt, 2000).

Therefore, more studies are required to determine the mechanism(s) responsible for fluctuations at different fluidization conditions and for different particle properties. The effect of different particle properties and fluidization conditions on the magnitude of these fluctuations must still be investigated. In the present study, instantaneous solid fraction maps for particles with relatively low Stokes numbers are investigated (St = 94). Localized measurements are conducted over the cross-section of the bed consisting of 316 pixels over a wide range of ($\overline{C}$). Analyses on the localized data on the magnitude of the fluctuations as well as their spatial trends are presented. Additionally, the cross-sectional averaged data are obtained to compare the results of this study with that of the existing literature.

2.2. Experimental procedure

2.2.1. Fluidized bed setup

Experiments were conducted using a 10.16 cm (I.D.) fluidized bed located at the Pipeline Transport Processes Research Lab at the University of Alberta, Canada. A schematic of the setup is shown as Figure 2.1. The working section (fluidized bed) consists of three parts: a transparent acrylic section, which allows for visual observation of the flow structure; the EIT test section; and above that, a stainless-steel pipe section. Screens were installed at the bottom and top of the bed to contain the particles. Below the bottom screen (i.e. upstream of the bed inlet) is a flow straightening section, which is packed with large acrylic spheres (d = 1 cm) to help produce an even flow distribution into the bed. A variable-speed centrifugal pump is used to circulate water through the circuit at different velocities. The liquid flowrate was measured using an orifice plate meter installed in the horizontal section of the setup between the pump discharge and the flow straightener.

The flow loop is designed to accommodate a fluidized bed of large-size particles in the size and Stokes number range studied by other researchers (d = 2 mm to 6 mm, and St = 94-3809) (Gevrin et al., 2010; Hashemi, 2013; Kechroud et al., 2010; Zenit and Hunt, 2000; Zenit et al., 1997) throughout the possible range of bulk solid fractions ($0.05 \leq \overline{C} \leq 0.6$). The parameters that can be controlled to achieve these objectives are:

- Bed inner diameter – Larger than 15 times the largest particle size (6 mm) to minimize the strength of wall effects near the centre of the bed
- Bed height – To be sufficiently high so that both EIT sensor planes are located inside the fluidized bed for any test conditions.
- Pump type – To provide sufficient pressure head and capacity under the fluidization conditions with the highest system head losses (4.5 mm Steel particles).

Based on these considerations, the required criteria for the bed height and pump head and capacity were obtained as below:

- Bed inner diameter : D = 10.16 cm (4”)
- Bed height: h = 2 m
- Pump type: SHURflo Centrifugal Pump (COMSV773), capacity to 168 GPM, head to 83 ft.

These chosen design allows measurements over a wide range particle sizes (2 mm to 6 mm) and solid densities (1150 kg/m^3 to 7950 kg/m^3), corresponding to particle Stokes numbers 94 to 3809.

The particles used for the present study were mono-sized, spherical Delrin beads, whose properties are shown in Table 2.1. The loop was filled with tap water at room temperature, and a very small amount of NaCl (0.85 g/L) was added to increase the liquid-phase conductivity. The increase in the background conductivity significantly improves the signal-to-noise ratio of the

Table2. 1 Particle specifications for the present study

Material	d (mm)	ρ_s(kg/m^3)	u_t (cm/s)	Re_t	St_t
Delrin	3.34	1400	18.1	606	94

voltage measurements, especially at very high solid volume fraction ($\overline{C}$ ≥ 0.5). We also expect that the use of a conductive medium helps to minimize any effects of electrostatic charging on the particles by allowing the charge to rapidly dissipate. The liquid temperature was measured at the bend upstream of the inlet of the fluidized bed section and was recorded during each experiment.

2.2.2. Electrical Impedance Tomography

Over the past 20 years, researchers have used electrical tomography methods to measure different flow parameters in multiphase flow systems (Azzi et al., 2010; Azzopardi et al., 2008; Bolton et al., 2004; Fangary et al., 1998; Hashemi, 2013; Hashemi et al., 2014; Zhu et al., 2003). Electrical tomography is a relatively fast, robust, simple to operate, and non-invasive method (Dyakowski et al., 2000). In addition, one of the important advantages of electrical tomography is that it is not dependent on the optical properties of the suspension (Norman and Bonnecaze, 2005). Rather, it is an online imaging technique that is based on measurements of a mixture's electrical impedance using an array of sensors.

A high-speed EIT instrument (Z8000, Industrial Tomography Systems) was used in the present study. This instrument consists of two planes of sensors in which 16 electrodes are located at equal spacing around the bed perimeter. The width and length of each electrode are both 10 mm. Electrical current is applied between one pair of adjacent electrodes and then the differential potentials between all remaining pairs of electrodes are measured. This procedure is repeated for all pairs of adjacent electrodes around the vessel (Dyakowski et al., 2000). Ohm's law is then used to determine the conductivity between all pairs of sensors. After obtaining the conductivity distribution maps, solid volume fraction maps are derived using Maxwell's equation to obtain (Dyakowski et al., 2000):

$$C_i = \frac{2\sigma_1+\sigma_2-2\sigma_m-\frac{\sigma_m\sigma_2}{\sigma_1}}{\sigma_m-\frac{\sigma_2}{\sigma_1}\sigma_m+2(\sigma_1-\sigma_2)} \quad (2.3)$$

where σ_1, σ_2, σ_m are the liquid phase conductivity, dispersed phase conductivity, and the reconstructed conductivity measured by EIT, respectively. Here, C_i is the dispersed phase volume fraction. In this study, for the EIT reconstruction algorithm, Modified Sensitivity Back-Projection (MSBP) has been used (Industrial Tomography Systems, 2014). The SBP method was developed based on the Linear Back-Projection (LBP) principle (Kotre, 1994). MSBP uses a nonlinear approximation to reconstruct the conductivity map from the voltage measurements obtained by EIT (i.e. conductivity is inversely related to voltage). This program is commercially available and built in in ITS electrical impedance tomography unit and its principles of operation are explained elsewhere (Wang, 2002; Wei et al., 2015).

2.2.3. Data processing

Measurements were made at different bulk (global) solid fractions by operating the fluidized bed at different superficial velocities. This enabled investigation of the local solid fraction fluctuations over a wide range of $\overline{C}$, including those approaching the maximum packing fraction. At each $\overline{C}$, 8000 instantaneous solid fraction maps were recorded at a sampling rate of 1186 frames per second (fps). The solid fraction is calculated at 316 locations (pixels) within the cross section, and the resulting reconstruction map is arranged as shown in Figure 2.2 (Industrial Tomography Systems, 2014). All the pixels have equal area. The measurements at each $\overline{C}$ were repeated 10 times to ensure measurement repeatability.

The magnitude of the root mean square (RMS) of the solid fraction fluctuations, $\overline{C'}$, is calculated for each pixel using:

$$\overline{C'} = \sqrt{\frac{1}{N}\sum_{i=1}^{N}(C_i - \overline{C_r})^2} \quad (2.4)$$

where $\overline{C_r}$ is the time-averaged local solid fraction calculated from:

$$\overline{C_r} = \frac{1}{N}\sum_{i=1}^{N} C_i \quad (2.5)$$

where C_i and *N* are instantaneous solid fraction, and the number of measured C_i, respectively. As mentioned previously, N = 8000 for the tests done in this study.

2.3. Results and discussion

2.3.1. Spatial variation in solid fraction fluctuations

From the different $\overline{C}$ tested in this study, selected time-averaged solid fraction and solid fraction fluctuation maps are presented here. Figures 2.3a, 2.3c, and 2.3e show the time-averaged solid fraction maps for bulk solid fractions of $\overline{C}$ = 0.11, 0.31, and 0.53, respectively. In these figures, r is the distance from the center of the bed and R is the bed radius. Values shown in each of these figures are calculated by averaging 8000 measured frames of the instantaneous solid volume fraction maps. As shown in these figures, the time-averaged local solid fraction is approximately uniform over the bed cross section and is equal to the average solid fraction. Although it is not shown here, measurements made with no flow, i.e. under packed bed conditions gave the expected value for randomly packed spheres ($\overline{C}$ = 0.60).

Figures 2.3b, 2.3d, and 2.3f show the local RMS of the solid fraction fluctuations for bulk solid fractions of $\overline{C} = 0.11$, 0.31 and 0.53, respectively. Similar to the time-averaged solid fraction maps, each of the RMS fluctuations maps are obtained by calculating the RMS fluctuations, using Equation (2.4), for 8000 measured frames of the instantaneous solid volume fraction maps. The fluctuation maps show that the magnitude of the fluctuations is significantly higher in the near-wall region and is approximately 3-4 times higher than the magnitude of fluctuations in the center region. Similar local distributions for both time-averaged solid fraction and RMS of solid fraction fluctuations have been observed for the different $\overline{C}$ tested in this study. Higher solid fraction fluctuation values near the bed wall have also been reported for 2, 3, and 4 mm spherical glass beads (Hashemi, 2013). In addition to the high shear zone near the wall, higher fluctuations in this region are most likely due to the fact that particle–wall collisions are dominant in the near-wall zone.

The power spectral densities of the particle volume fraction fluctuations were calculated using a fast-Fourier-transform routine. The time signals and power spectra shown in Figure 2.4 are

representative data from pixels at five different radial positions in the bed cross section, for the case of $\overline{C}$ = 0.31. Each power spectrum shown in this figure is an average obtained from 10 measurements (blocks). A sample of the corresponding time signal of the solid fraction fluctuations for each power spectrum density is also shown in Figure 2.4. The y-axis of the time signal is calculated as $C_i - \overline{C_r}$. The time signals show that by moving from the center region toward the near wall region, the overall magnitude of the power spectra increases significantly. The source of this increase is most likely the dominance of particle–wall collisions in the near-wall region. Due to this dominance the maximum peak-to-peak amplitude of the fluctuations at the near-wall region is significantly higher than that at the center of the bed. The power spectra show that the maximum amplitude occurs at frequencies around 1 Hz for this concentration. Beyond this maximum, the power density decays for all the radial positions. The rate of this decay is -3 at higher frequencies. After this decay, all power spectra demonstrate a dominant white noise (measurement noise) for high frequencies (above 20 to 50 Hz). The -3 slope of decay was also observed in the numerical study done by Gevrin et al. (2010) for the fluidization system of three different particle types. This slope of the decay can be an indication of a 2D turbulent flow in the fluidized bed. This phenomenon is further discussed in Section 2.3.3.

Figure 2.5 shows the power spectrum at the center of the bed compared to that of the near-wall zone for a better comparison. Based on this figure, across all the frequencies, the amplitude of the power spectrum in the near wall region is approximately two orders of magnitude higher than that of the centre of the bed, i.e. for frequencies smaller than 10, the r/R=0.95 spectrum is essentially the r/R=0.05 spectrum shifted up. And as discussed for Figure 2.4, the slopes of the power-law decays do not change with changing radial position. Similar trends in both the time- and frequency-domains were observed for all other bulk solid fractions tested in this study. The observation that the amplitude of the power spectrum is higher in the near-wall region than the centre of the bed is expected due to the additional contribution of the particle-wall interactions in this region. The higher amplitudes of the power spectrum in this region are representative of the higher magnitudes of RMS fluctuations which is consistent with the results of Hashemi (2013) for glass particles of 2–4 mm.

The spatial trends of the RMS fluctuations are shown in Figure 2.6. To obtain each line in this figure the measured local data were azimuthally averaged for each of the three bulk solid fractions. The results show that the magnitude of the local fluctuations is different for different bulk solid fractions, but the trend with increasing r is the same.

The maximum RMS of the solid fraction fluctuations occurs at $\overline{C} = 0.31$. In the low-solid-fraction region, the RMS fluctuations increase only marginally when the bulk solid fraction is increased from $\overline{C} = 0.11$ to $\overline{C} = 0.31$, but when the bulk solid fraction is further increased to $\overline{C} = 0.53$, a much more significant decrease in fluctuations is observed. (Hashemi, 2013) reported similar trends for the radial distribution of fluctuations for glass particles. The magnitudes of the RMS of the fluctuations for the 2, 3 and 4 mm glass beads (100 < St_t< 500) used in that study were reported to be in the range of $\overline{C'}$ = 0.012 to 0.05 (Hashemi, 2013). Figure 2.6 shows that overall for the current Delrin particles ($St_t = 94$) the RMS values falls within a slightly lower range ($\overline{C'}$= 0.005 to 0.023). This is consistent with the findings of (Zenit and Hunt, 2000) that particles with lower Stokes numbers have weaker fluctuations.

2.3.2. Effect of bulk solid fraction on fluctuations

Figure 2.7 shows the representative data of the power spectra and their corresponding time signals from the same pixel for five different bulk solid volume fractions, at a radial position of r/R=0.55. Similar to Figure 2.4, the power spectra shown here are averaged over 10 blocks. As with the time signals, the spectra show that by increasing the mean solid volume fraction, the magnitude of fluctuations increases slightly for $\overline{C} \leq 0.40$, and then decreases for $\overline{C} > 0.40$. The spectra show that for all the bulk solid fractions shown in Figure 2.7, the maximum power magnitude occurs in the lowest frequency range and the measurement noise is dominant at frequencies higher than 30 Hz. Below this frequency, for all the $\overline{C}$, a -3 power law decay occurs at higher frequencies. At lower frequencies, especially for lower solid volume fractions, the spectra flatten out. With changing bulk volume fraction, the frequency where the transition between the -3 slope region and a flatter slope region occurs (f_t) also changes: $f_t \approx 4$ Hz at $\overline{C}$ = 0.11 to $f_t \approx 1$ Hz at $\overline{C} \geq$0.40. (These transitions are estimated visually.) To further study the

extent of the -3 slope region and where f_t occurs, the power spectral densities (PSD) can be multiplied by f^3 (Thais and Magnaudet, 1996). This results in a product signal that should have a slope of zero (horizontal) in the frequency range where the original power spectrum had a slope of -3. Figure 2.8 shows $\mathrm{PSD} \cdot f^3$ for $\overline{C}$ =0.11, 0.40, and 0.53. It can be seen that for $\overline{C}$ =0.11 the slope of the power spectrum was -3 in the frequency range [4–14Hz]. In contrast to the $\overline{C}$ =0.11 line, for which the positive slope in the range of [1–4Hz] indicates that the original slope was less than -3, neither the $\overline{C}$ =0.40 nor $\overline{C}$ =0.53 line drops below a slope of -3 until frequencies under 1 Hz.

2.3.3. Theoretical implications of power spectral analysis

In a three-dimensional turbulent flow, the random motions of the particles result in a -5/3 decay rate in the power spectrum at high frequencies (i.e. the Kolmogorov spectrum) (Pope, 2000). However, at high frequencies, the power spectrum of a 2D turbulent flow is predicted to exhibit a -3 power decay (Lemmin et al., 1974; Lilly, 1969). Based on the power spectra shown in Figure 2.7, it can be concluded that the turbulent flow pattern is similar to that of a 2D turbulent flow. Such a 2D turbulent flow can result from external forcing of the system by a force with a single time scale (Lemmin et al., 1974; Lilly, 1969; Sommeria and Moreau, 1982; Thais and Magnaudet, 1996). In a solid–liquid particulate fluidization system, this external force (with a low-frequency) would be associated with travelling waves manifest as void fraction fluctuations commonly considered to arise from instability of the equilibrium state of fluidization (El-Kaissy and Homsy, 1976; Gibilaro et al., 1990; Ham et al., 1990). The effect of these waves on the particle velocity field was observed in the 2D numerical study of Gevrin et al. (2010). They showed that these "aggregate" and "void fraction waves" are always present in the solid volume fraction field, but they only strongly affect the velocity field at high $\overline{C}$. Specifically, the "concentric zones" of combined lateral and vertical motion observed in the particle velocity field at low bulk solid fraction "coalesce" and result in fewer circular patterns and more vertical velocity vectors at higher bulk solid fractions (Gevrin et al., 2010).

In the present results, the fact that the frequency at which the -3 slope begins to dominate (f_t shown in Figure 2.7) decreases with increasing $\overline{C}$ indicates that the dominance of this forcing and its frequency depend on the bulk solid volume fraction, which is expected from past reports of such void fraction waves (El-Kaissy and Homsy, 1976; Gibilaro et al., 1990; Ham et al., 1990). This decreasing transition frequency would be expected to be accompanied by increasing dominance of larger length scales in the turbulent flow pattern. This observation can also be seen in the velocity fields obtained by Gevrin et al. (2010) for their particles with low and medium Stokes numbers. Based on their results, by increasing $\overline{C}$, most of the smaller circulations disappear and the particle velocity field became dominated by large-scale circular movement and more vertically aligned velocity vectors (Gevrin et al., 2010).

From a broader perspective, for any case of 2D turbulence driven by a random narrow-frequency disturbing force, an energy balance requires that a -3 slope occur at frequencies above the forcing frequency as predicted by Kraichnan (1967) and later confirmed by Lilly (1969). Further, their work expects a -5/3 slope at lower frequencies. The expected transition from a -5/3 slope to a -3 slope as frequency increases is at the frequency of the external forcing. Based on the limited data points in the low-frequency region, the power spectra shown in Figure 2.7 suggest a -5/3 power-law decay below f_t. This additional slope is best suggested by the $\overline{C}$=0.11 graph, where the sloped region between the flat region and f_t is approximately -5/3. It should be noted that the -5/3 slope is not seen at $\overline{C} \geq 0.4$ because it is probably hidden under the flat section of the spectrum. However, with the current data this result is not conclusive because of the limited frequency extent of this region.

Though not conclusive, the result is certainly consistent with the interpretation that a signal corresponding to an external force is coupled with the turbulent spectrum and drives the fluctuations. This signal ranges from 1–4 Hz for the current system and varies with $\overline{C}$. As discussed above, this high-magnitude, low-frequency signal is best understood to correspond to upward travelling void fraction waves that cause vertical motion in the bed and are more significant at high bulk solid fractions.

Corroborating evidence for the explanation that the driving force is provided by propagating void fraction waves is available by considering the variation of f_t with $\overline{C}$. Though classic analyses of the propagating void fraction waves (such as Ref. (Gibilaro et al., 1990)) have focused on propagation velocity instead of dominant frequency, experimental data for a variety of conditions provided by Ham et al. (1990) show that for a given fluidization system, the dominant frequency of these instability void fraction waves increases monotonically with the Froude number, which is defined as:

$$\mathrm{Fr} = \frac{{u_s}^2}{gd} \tag{2.6}$$

where u_s is the superficial velocity, d is particle size, and g is the acceleration due to gravity. The plot should also approach zero at the minimum fluidization velocity. Figure 2.9 plots the data for the current system, and the expected behaviour is clearly observed (note that the values for f_t are only estimated visually here explaining the integer values). Taken together, the results strongly suggest that it is correct to interpret these void fraction waves as the driver of the behaviour observed in the spectra.

2.3.4. RMS solid fraction fluctuation

In Figure 2.10, the cross-sectional averages of the RMS of solid fraction fluctuations are plotted as a function of $\overline{C}$. This averaging enables us to compare the local data obtained in this study with the available data in the literature. Therefore, the models of Buyevich and Kapbasov (1994) and the experimental data of Zenit and Hunt (2000) for 3.41 mm PVC cylinders (ρ_s = 1430 kg/m^3) are shown. This particular dataset from the Zenit and Hunt's study is shown because the Stokes numbers of the PVC cylinders and the Delrin beads are very close. The solid line in Figure 2.10 shows predictions obtained using the original version of the model by Buyevich and Kapbasov (1994):

$$\overline{C'^2} = \overline{C}^2 \left[1 + 2\overline{C}\,\frac{4-\overline{C}}{\left(1-\overline{C}\right)^4}\right]^{-1} \tag{2.7}$$

where $\overline{C}$ is bulk solid fraction, and $\overline{C'^2}$is mean square solid fraction fluctuation. The dashed line in Figure 2.10 represents the predictions obtained using the modified version of the model for high bulk solid fractions (Buyevich and Kapbasov, 1994):

$$\overline{C'^2} = \overline{C}^2 \left[1 - \left(\frac{\overline{C}}{C_{max}}\right)^{1/3}\right]\left[1 + \frac{1}{3}\left(\frac{(\overline{C}/C_{max})^{1/3}}{1-(\overline{C}/C_{max})^{1/3}}\right)\right]^{-1} \quad (2.8)$$

where C_{max} is the empirically determined value of the solid volume fraction at close packing (Buyevich and Kapbasov, 1994).

The experimental data from the present study are in good agreement with Zenit and Hunt (2000)'s measurements for PVC cylinders with a similar Stokes number. It should be noted that Zenit and Hunt (2000) used a high-pass filter to isolate small-scale fluctuations before calculating the data shown here in Figure 2.10. Such filtering did not seem necessary in the current study. The reason why their filtered data match well with the non-filtered data of this study may be due to the difference in the measurement instruments (IVFM vs EIT) or the different shapes of the particles (cylinder vs. sphere), but more investigation of this discrepancy is required.

In Figure 2.10, the mathematical model, as expected, overpredicts the RMS values for particles with low Stokes numbers, but the experimental trend is very similar to the trend predicted by the models. The maximum RMS of the solid fraction fluctuations is predicted to occur around $\overline{C}$ = 0.3 by both versions of the model. As shown in Figure 2.6, the RMS fluctuations for the Delrin beads of this study exhibit a maximum value at $\overline{C}$ = 0.31.

2.4. Conclusions

Results presented here for Delrin beads demonstrate that the cross-sectional-averaged values of the RMS of fluctuations of solid concentration in a liquid fluidized bed were in good agreement with the existing experimental data of Zenit and Hunt (2000). RMS values measured for a wide range of bulk solid fractions also followed the general trend of the Buyevich and Kapbasov (1994) model, as expected, but were lower than predicted values because of the relatively low particle Stokes number (St ≈ 100). However, the local measurement of the fluctuations showed that the

magnitude of the fluctuations can be up to 3-4 times greater than that at the center of the bed. The highest magnitude of the fluctuations was observed in the near-wall region.

Analysis of the power spectra of the fluctuations showed that, although changing the radial position did not change the slope of the decay, the power spectrum's magnitude was significantly higher in the near-wall zone. On the other hand, increasing the bulk volume fraction had a significant effect on both the magnitude of the spectrum and extent of the slopes of the decays. By increasing the bulk solid volume fraction, the transition frequency between -5/3 and -3 slopes in the spectra moved to lower frequencies (i.e. from 4 Hz to 1 Hz). The slopes of the power spectra suggest the existence of an external force coupled with the 2D turbulent spectrum. More analysis showed that this external force is most probably associated with instability void fraction waves in the fluidized bed.

The results presented here demonstrate the importance of local instantaneous volume fraction measurements in understanding the nature of the small-scale fluctuations and dynamic behaviour of liquid fluidized beds. These results can also be used for validation of numerical models of fluidization.

Additional experiments are underway to determine the local solid fraction fluctuations for particles having moderate and high Stokes numbers to quantify the effects of Stokes number on the nature and magnitude of the local solid fraction fluctuations and on the radial distribution of solids during fluidization. The comparison between the results presented in this study with that of Hashemi (2013) who used particles with higher Stokes numbers showed that increasing the particle Stokes number resulted in an increase in the magnitude of the local RMS fluctuations. This was also consistent with the findings of Zenit and Hunt (2000), for the magnitude of the cross-sectional averaged RMS fluctuations. Taken together, similar spatial trends for the local RMS fluctuations are predicted, i.e. higher RMS fluctuations near the wall region for particles with higher Stokes numbers. Also at any given radial position, an increase in the magnitude of RMS fluctuations is expected by increasing the particle Stokes number.

Furthermore, additional analyses are planned including estimation of the fluctuations' length-scales by conducting the cross-correlations between different pixels in the cross-section of the bed.

The longer-term objective is to provide more accurate models to predict the magnitude of local solid fraction fluctuations based on the bulk solid fraction and the particle Stokes number.

2.5. Figures

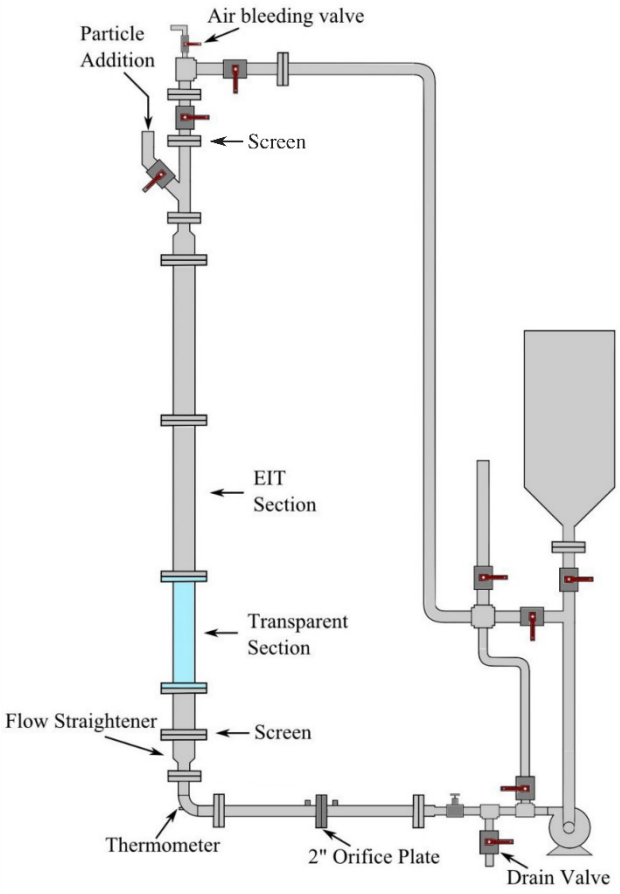

Figure 2. 1. Schematic layout of the experimental setup

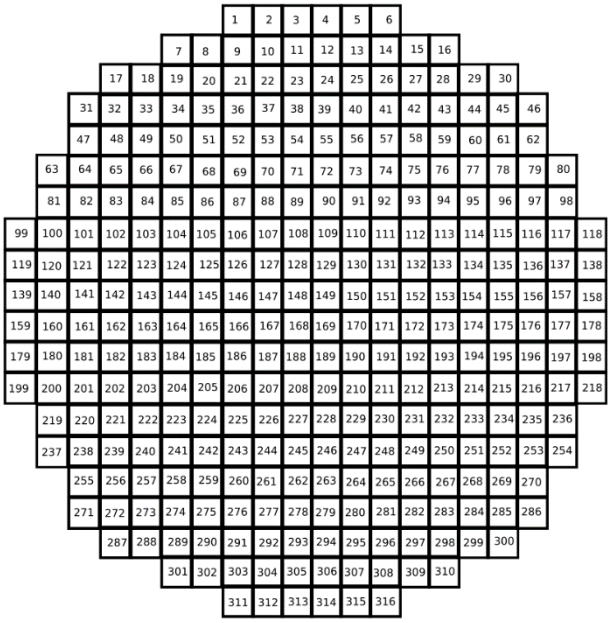

Figure 2. 2. EIT reconstruction grid (Industrial Tomography Systems, 2014)

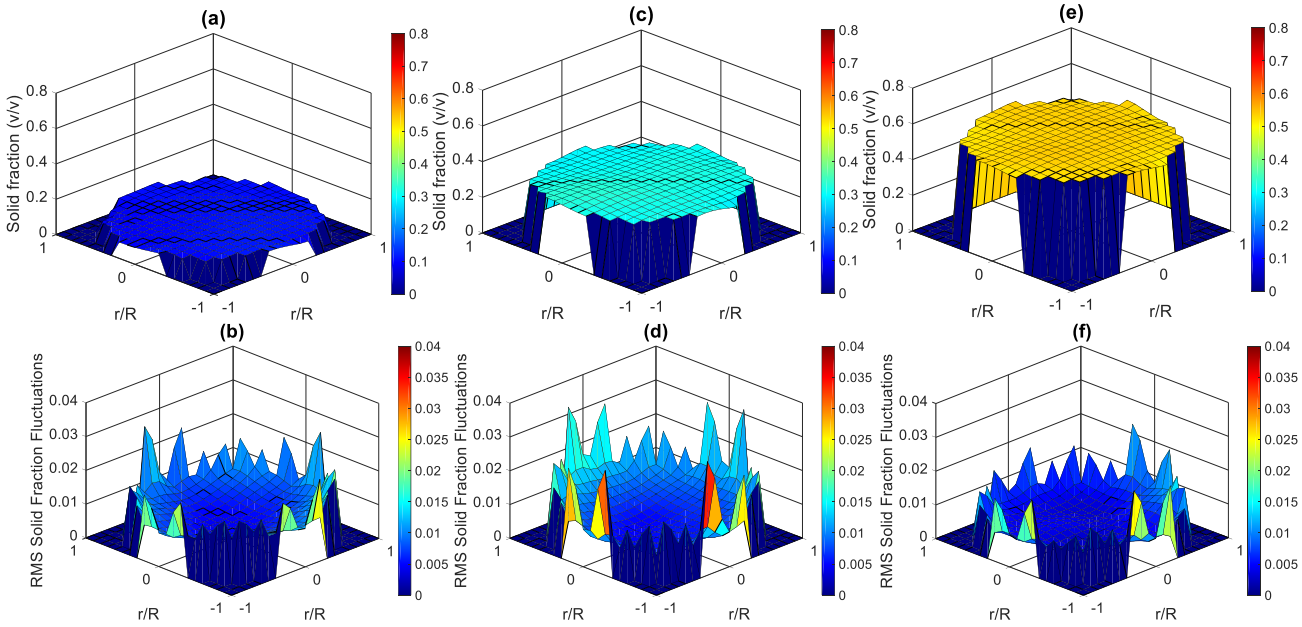

Figure 2. 3. Time averaged mean (first row) and RMS (second row) solid fraction maps: (a) and (b) $\overline{C}$= 0.11; (c) and (d) $\overline{C}$= 0.31; (e) and (f) $\overline{C}$ = 0.53.

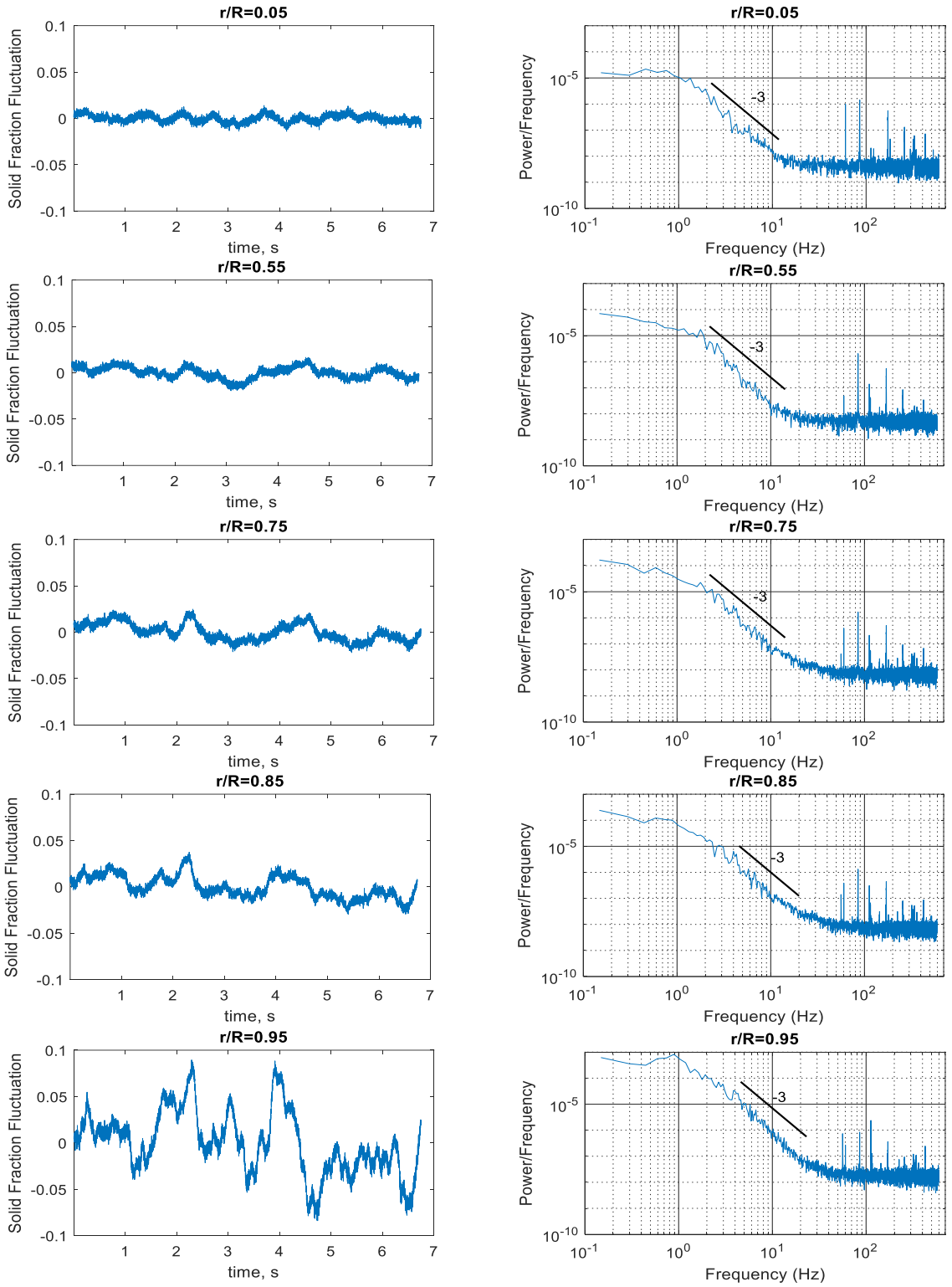

Figure 2. 4. Solid fraction fluctuations, $C_i - \overline{C_r}$, and solid fraction power spectra for $\overline{C}$ = 0.31.

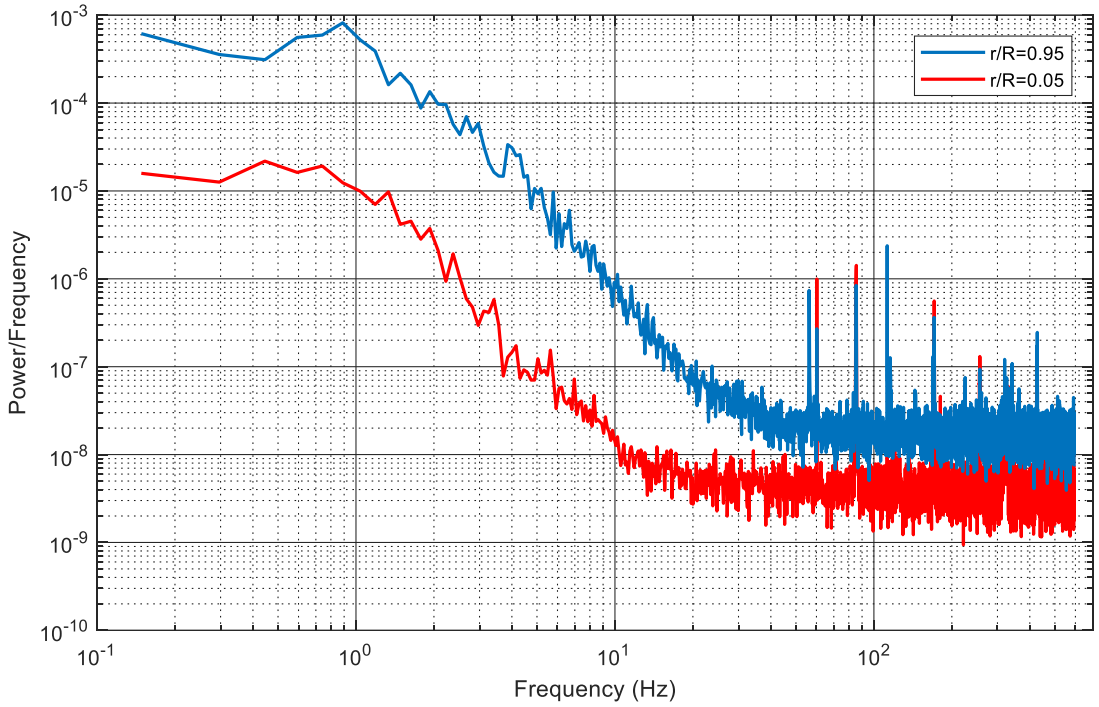

Figure 2. 5. Solid fraction power spectra for $\overline{C}$ = 0.31 at two different radial positions

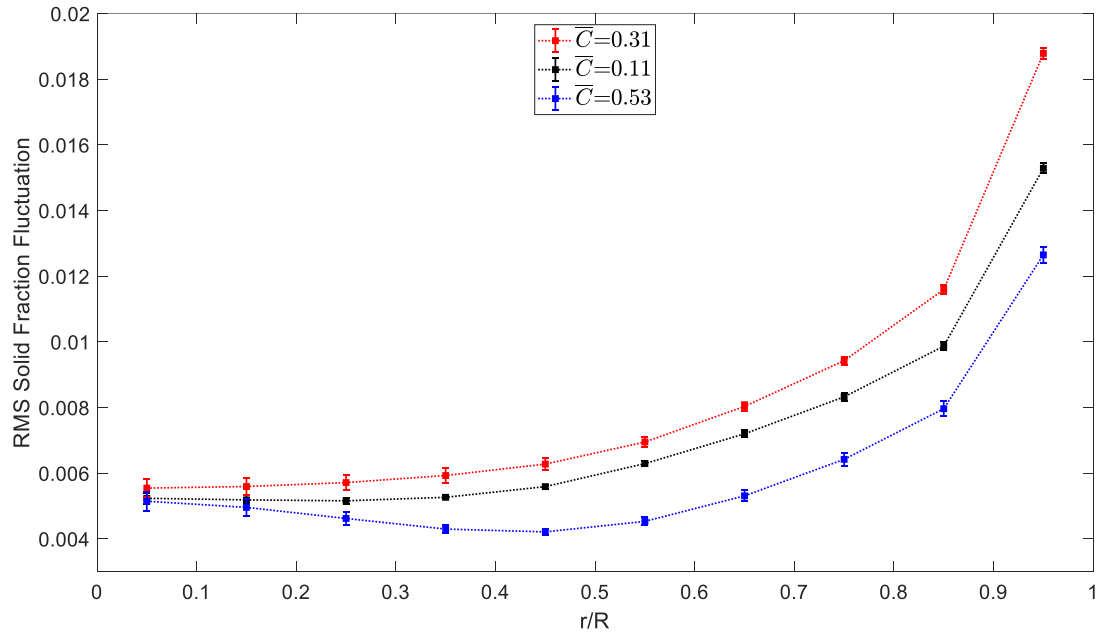

Figure 2. 6. Radial distributions of the RMS of solid fraction fluctuations for $\overline{C}$ = 0.11, 0.31, and 0.53. Error bars shown in this figure illustrate standard errors. For each data point the error bars are calculated from 10 trials.

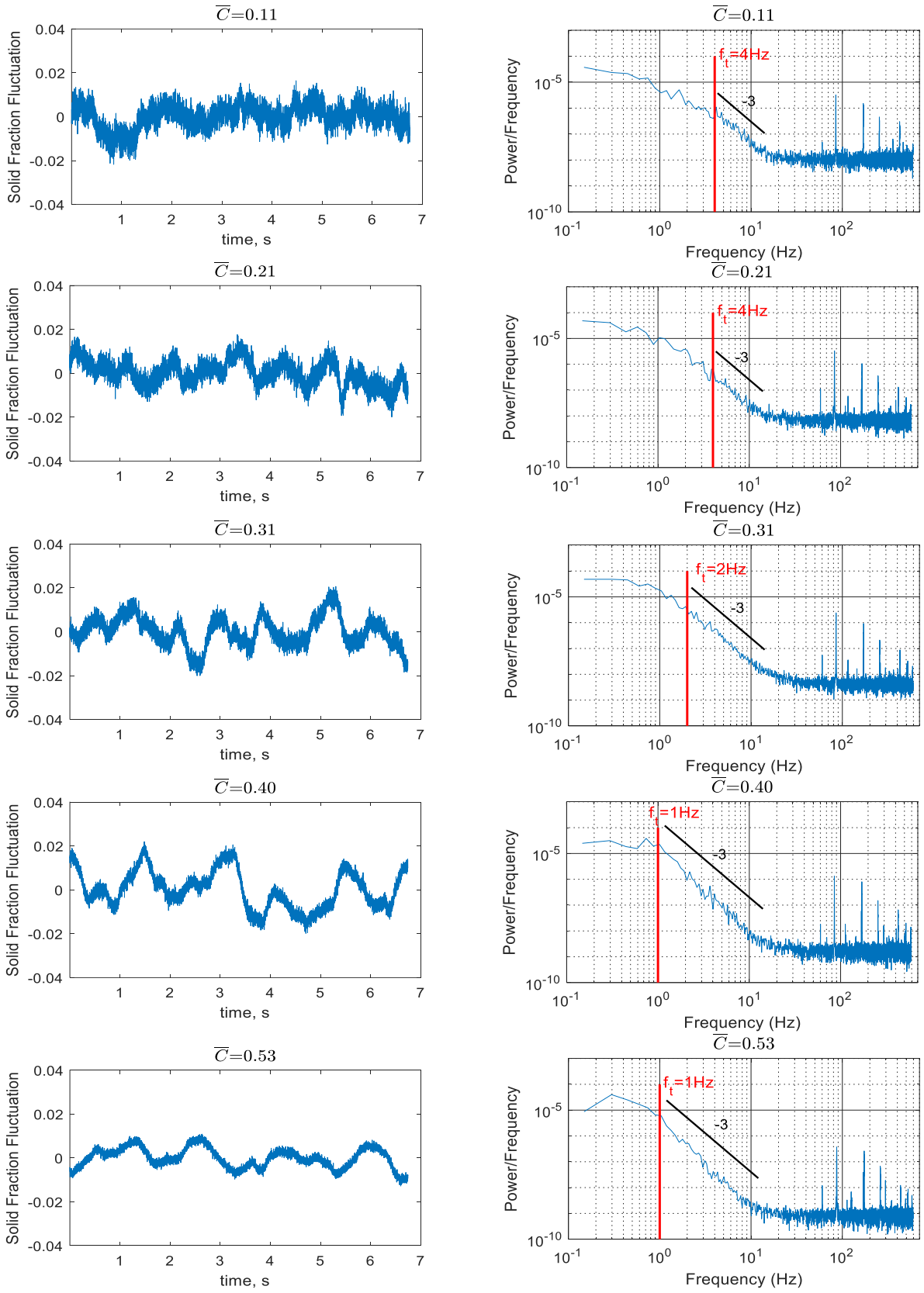

Figure 2. 7. Solid fraction fluctuations, $C_i - \overline{C_r}$, and solid fraction power spectra at r/R=0.55.

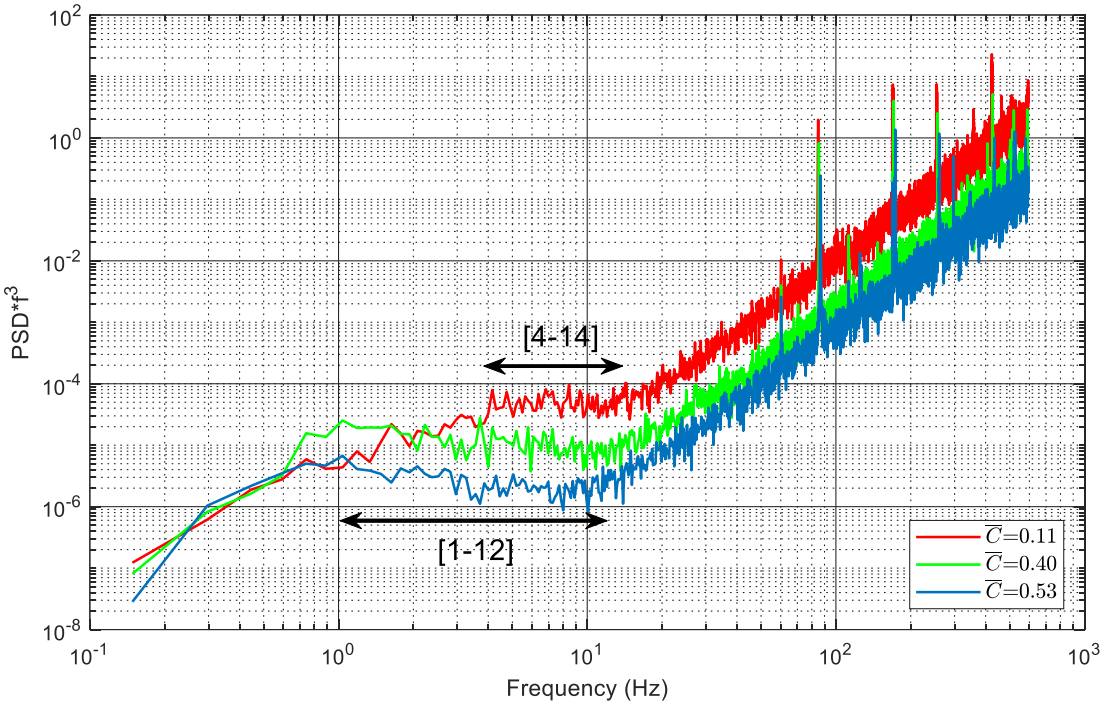

Figure 2. 8. PSD·f^3 product signal for three of the bulk solid volume fractions shown in Figure 2.7. All at r/R=0.55.

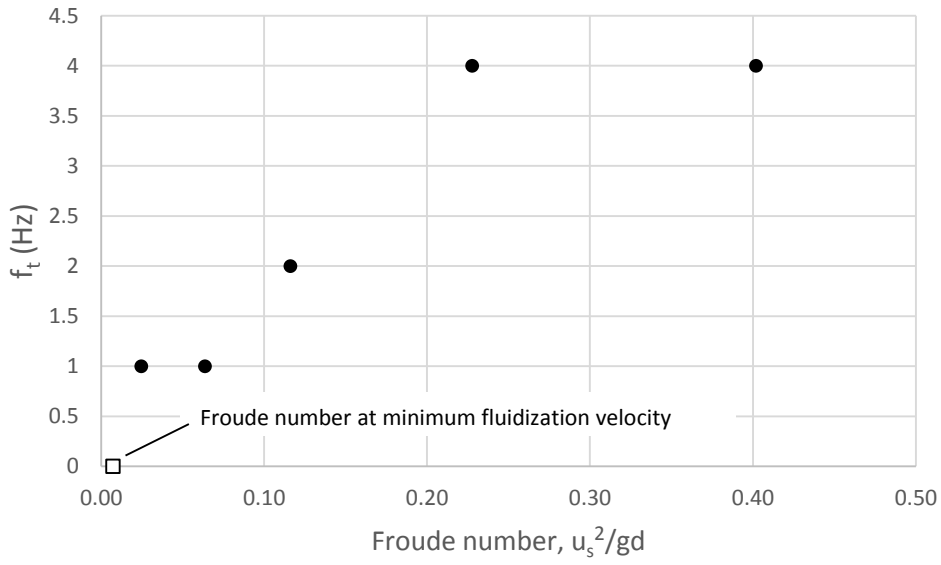

Figure 2. 9. Transition frequency (f_t) vs Froude number (Fr) for the five bulk solid volume fractions shown in Figure *2.*7. All at r/R=0.55.

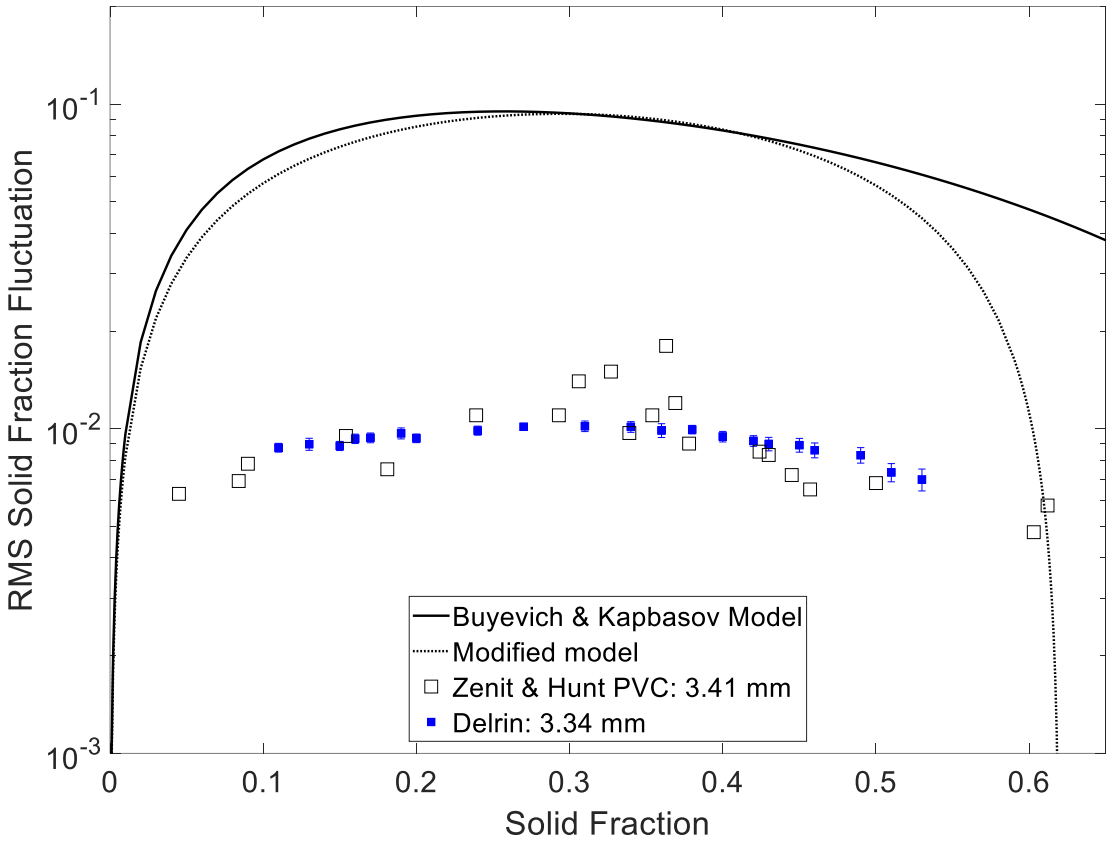

Figure 2. 10. Cross sectional averaged RMS of solid fraction fluctuations: Present study, results for 3.34 mm Delrin (▪); Zenit and Hunt, 2000 (□); Predictions of Eqn (2.7) (solid line) and Eqn (2.8) (dashed line). Error bars shown in this figure illustrate standard errors. For each data point the error bars are calculated from 10 trials.

2.6. References

Abbas, M., Climent, E., Parmentier, J.-F., and Simonin, O. (2010). Flow of particles suspended in a sheared viscous fluid: Effects of finite inertia and inelastic collisions. AIChE J. *56*, 2523–2538.

Azzi, A., Azzopardi, B.J., Abdulkareem, N.H., Hilal, N., and Hunt, A. (2010). Study of fluidization using Electrical Capacitance Tomography. Proceedings of the 7th International Conference on Multiphase Flow ICMF 2010, (Florida, USA).

Azzopardi, B.J., Jackson, K., Robinson, J.P., Kaji, R., Byars, M., and Hunt, A. (2008). Fluctuations in dense phase pneumatic conveying of pulverised coal measured using electrical capacitance tomography. Chem. Eng. Sci. *63*, 2548–2558.

Bolton, G.T., Hooper, C.W., Mann, R., and Stitt, E.H. (2004). Flow distribution and velocity measurement in a radial flow fixed bed reactor using electrical resistance tomography. Chem. Eng. Sci. *59*, 1989–1997.

Buyevich, Yu.A., and Kapbasov, Sh.K. (1994). Random fluctuations in a fluidized bed. Chem. Eng. Sci. *49*, 1229–1243.

Didwania, A.K., and Homsy, G.M. (1981). Flow regimes and flow transitions in liquid fluidized beds. Int. J. Multiph. Flow *7*, 563–580.

Dyakowski, T., Jeanmeure, L.F.C., and Jaworski, A.J. (2000). Applications of electrical tomography for gas–solids and liquid–solids flows — a review. Powder Technol. *112*, 174–192.

El-Kaissy, M.M., and Homsy, G.M. (1976). Instability waves and the origin of bubbles in fluidized beds: Part 1: Experiments. Int. J. Multiph. Flow *2*, 379–395.

Epstein, N. (2002). Applications of Liquid-Solid Fluidization. Int. J. Chem. React. Eng. 1, 1-16

Fangary, Y.S., Williams, R.A., Neil, W.A., Bond, J., and Faulks, I. (1998). Application of electrical resistance tomography to detect deposition in hydraulic conveying systems. Powder Technol. *95*, 61–66.

Gevrin, F., Masbernat, O., and Simonin, O. (2008). Granular pressure and particle velocity fluctuations prediction in liquid fluidized beds. Chem. Eng. Sci. *63*, 2450–2464.

Gevrin, F., Masbernat, O., and Simonin, O. (2010). Numerical study of solid–liquid fluidization dynamics. AIChE J. *56*, 2781–2794.

Gibilaro, L., Foscolo, P., and Felice, R.D. (1990). The Velocity of Dynamic Waves in Fluidised Beds. In Two Phase Flows and Waves, (Springer, New York, NY), pp. 56–69.

Ham, J.M., Thomas, S., Guazzelli, E., Homsy, G.M., and Anselmet, M.-C. (1990). An experimental study of the stability of liquid-fluidized beds. Int. J. Multiph. Flow *16*, 171–185.

Hashemi, S.A. (2013). Velocity and concentration fluctuations in concentrated solid-liquid flows. PhD thesis. University of Alberta.

Hashemi, S.A., Sadighian, A., Shah, S.I.A., and Sanders, R.S. (2014). Solid velocity and concentration fluctuations in highly concentrated liquid–solid (slurry) pipe flows. Int. J. Multiph. Flow *66*, 46–61.

Industrial Tomography Systems (2014). ITS Tomography Toolsuite v7.32 User's manual (Manchester, UK: Industrial Tomography Systems Plc).

Kechroud, N., Brahimi, M., and Djati, A. (2010). Characterization of dynamic behaviour of the continuous phase in liquid fluidized bed. Powder Technol. *200*, 149–157.

Kotre, C.J. (1994). EIT image reconstruction using sensitivity weighted filtered backprojection. Physiol. Meas. *15*, A125–A136.

Kraichnan, R.H. (1967). Inertial Ranges in Two-Dimensional Turbulence. Phys. Fluids *10*, 1417–1423.

Lemmin, U., Scott, J.T., and Czapski, U.H. (1974). The development from two-dimensional to three-dimensional turbulence generated by breaking waves. J. Geophys. Res. *79*, 3442–3448.

Lilly, D.K. (1969). Numerical Simulation of Two-Dimensional Turbulence. Phys. Fluids *12*, II–240.

Norman, J.T., and Bonnecaze, R.T. (2005). Measurement of Solids Distribution in Suspension Flows using Electrical Resistance Tomography. Can. J. Chem. Eng. *83*, 24–36.

Pope, S.B. (2000). Turbulent Flows (Cambridge University Press).

Sommeria, J., and Moreau, R. (1982). Why, how, and when, MHD turbulence becomes two-dimensional. J. Fluid Mech. *118*, 507–518.

Thais, L., and Magnaudet, J. (1996). Turbulent structure beneath surface gravity waves sheared by the wind. J. Fluid Mech. *328*, 313–344.

Wang, M. (2002). Inverse solutions for electrical impedance tomography based on conjugate gradients methods. Meas. Sci. Technol. *13*, 101–117.

Wei, K., Qiu, C., Soleimani, M., and Primrose, K. (2015). ITS Reconstruction Tool-Suite: An inverse algorithm package for industrial process tomography. Flow Meas. Instrum. *46*, 292–302.

Zenit, R., and Hunt, M.L. (2000). Solid fraction fluctuations in solid–liquid flows. Int. J. Multiph. Flow *26*, 763–781.

Zenit, R., Hunt, M.L., and Brennen, C.E. (1997). Collisional particle pressure measurements in solid-liquid flows. J. Fluid Mech. *353*, 261–283.

Zhu, K., Madhusudana Rao, S., Wang, C.-H., and Sundaresan, S. (2003). Electrical capacitance tomography measurements on vertical and inclined pneumatic conveying of granular solids. Chem. Eng. Sci. *58*, 4225–4245.

Chapter 3. Experimental Study of Local Solid Volume Fraction Fluctuations in a Liquid Fluidized Bed: Particles with a wide range of Stokes numbers

Material in this chapter is in preparation for submission as:

Marefatallah, M., Breakey, D., and Sanders, R.S. (2019). Experimental Study of Local Solid Volume Fraction Fluctuations in a Liquid Fluidized Bed: Particles with a wide range of Stokes numbers.

3.1. Introduction

Liquid fluidized beds are a common example of a solid–liquid system used in current industrial units. Examples of their industrial applications are particle classification, sedimentation, biochemical reactors used in wastewater treatment, and electrolysis applied for metal recovery (Epstein, 2002). Despite wide application of liquid fluidization systems, their design, scale-up, and operation are not currently being done based on computational simulations and modeling (Cornelissen et al., 2007). One of the reasons why their operation is still based on empirical methods (Zhang et al., 2012) is that, unlike gas-solid fluidization systems, very little work has been done on the modeling of liquid fluidized beds (Panneerselvam et al., 2007). Developing reliable liquid fluidization models requires an understanding of the particle–particle, particle–fluid and particle–wall interactions at fine scales. This understanding is especially important for the prediction of parameters such as particle distribution, flow pattern, bed expansion, and solid and liquid velocities (Gevrin et al., 2010). Experimental measurements of the instantaneous distribution of particles in the bed cross-section (i.e. local instantaneous solid volume fraction) are required to examine and validate the predictions of any models that attempt to capture the physics of fluidized bed systems. Local instantaneous solid volume fraction (C_r) can be divided into two components by Reynolds averaging: $C_r = \overline{C_r} + C_r'$, where $\overline{C_r}$ and C_r' are the time-averaged and fluctuating components of the solid volume fraction, respectively, and the subscript r, denotes that solid volume fraction is measured at distance r/R (R: bed radius) from the center of the bed. The purpose of this study is to provide local measurements of the fluctuating component of the solid fraction for particles of different sizes and densities. These local measurements can be used to validate liquid fluidization models, specifically those which aim to predict the magnitude of the solid fraction fluctuations. This study also makes such a comparison for models that have gained acceptance in the literature and discusses the performance of each model.

3.1.1. Models predicting solid volume fraction fluctuations in a liquid fluidized bed

Currently, there are four popular models presented in the literature for the prediction of C_r' in liquid fluidization systems. These models are listed in Table 3.1. In this table, C_{max} is solid volume fraction at a close-packed state. C_{D0} is the Schiller and Nauman drag coefficient (for a single particle and based on the slip velocity), $\bar{C}$ is the bulk solid volume fraction, and n is the Richardson-Zaki exponent. Table 3.1 also introduces a short name for each of the models (B, BK1, BK2, and G), which will be used to refer to each model throughout this paper.

Three of the models shown in Table 3.1 were developed by Buyevich (1971); Buyevich and Kapbasov (1994). Gevrin et al. (2010) proposed a semiempirical model for the prediction of these fluctuations. The first model proposed by Buyevich (1971) , here labelled as Model B, was based on a lattice model of dispersed mono-sized spherical particles. This model mainly looked at the statistical positioning of spherical particles in a solid–liquid system.

Table 3.1. Models predicting solid volume fraction fluctuations in a liquid fluidized bed

Model	Equation	Reference
B	$\overline{C_r'^2} = \overline{C_r}^2 \left(1 - \frac{\overline{C_r}}{C_{max}}\right)$	(Buyevich, 1971)
BK1	$\overline{C_r'^2} = \overline{C_r}^2 \left[1 + 2\overline{C}\frac{4 - \overline{C_r}}{\left(1 - \overline{C_r}\right)^4}\right]^{-1}$	(Buyevich and Kapbasov, 1994)
BK2	$\overline{C_r'^2} = \overline{C_r}^2 \left[1 - \left(\frac{\overline{C_r}}{C_{max}}\right)^{1/3}\right]\left[1 + \frac{1}{3}\left(\frac{\left(\overline{C_r}/C_{max}\right)^{1/3}}{1 - \left(\overline{C_r}/C_{max}\right)^{1/3}}\right)\right]^{-1}$	(Buyevich and Kapbasov, 1994)
G	$\overline{C'} \propto \frac{2[C_{D0}\bar{C}\,(1-\bar{C})^{-4.7}]^{1/3}\left(1 - \frac{\bar{C}}{C_{max}}\right)^{nC_{max}}}{3(n-1)(1-\bar{C})^{n-2}}$	(Gevrin et al., 2010)

The next two models developed by Buyevich and Kapbasov (1994), Models BK1 and BK2, were based on the thermodynamic theory of fluctuations. The third model, Model BK2, was a modified version of Model BK1 to account for the cases of high bulk solid fractions in the bed. The magnitudes of the fluctuations predicted by Models BK1 and BK2 deviate significantly from each other at $\overline{C} \geq 0.45$. And at a given bulk solid fraction, Model B predicts higher values of fluctuations compared to Models BK1 and BK2. On the other hand, the Gevrin et al. model, Model G, was based on the relationship between the solid fraction fluctuations and the fluctuating kinetic energy of the solid phase (Gevrin et al., 2010). This model was based on another semiempirical scaling law proposed in their previous work which predicted the fluctuating kinetic energy of the solid phase as a function of bulk solid fraction (Gevrin et al., 2008).

Gevrin et al.'s (2010) model is the only model in Table 3.1 that includes parameters involving particle properties, namely, the scaling factor, n, and C_{D0}. All the other models are a function only of the local mean solid fraction of particles (Model BK1) and the maximum packing concentration (Models B and BK2).

All these models are developed based on the assumption of macroscopically uniform or homogenous flows which is not necessarily applicable to all liquid fluidization systems, especially at high bulk solid fractions (Didwania and Homsy, 1981).

The models shown in Table 3.1 need to be validated with experimental data of the local solid fraction fluctuations measured in a liquid fluidized bed. These measurements are not easy to perform especially for dense and/or opaque suspensions (Derksen and Sundaresan, 2007). The experimental measurements that have been reported so far compared their results to the predictions of these models but were limited to cross-sectional averaged values (Zenit and Hunt, 2000). This paper will compare local values to the predictions of these models for the first time.

3.1.2. Measurements of solid volume fraction fluctuations in a liquid fluidized bed

The first study that measured the solid fraction fluctuations (published in 1981) was mainly focused on quantifying different flow regimes in a solid–liquid fluidized bed (Didwania and Homsy, 1981). Therefore, the authors reported only a few data points of the magnitude of the fluctuations which were limited to the high bulk solid fractions (i.e. $\overline{C} \geq 0.44$). Several years later, Zenit and Hunt (2000) expanded the early work by extensive measurements of the solid fraction fluctuations for five different particle types over a wide range of bulk solid fractions. These measurements were conducted using an Impedance Volume Fraction Meter (IVFM). Although IVFM is a non-invasive technique, it only provides a cross-sectional average of the instantaneous solid fraction (Zenit and Hunt, 2000). Zenit and Hunt's (2000) cross-sectional results showed that St_t has an important effect on the magnitude of the fluctuations. Therefore, models such as Model B, BK1, and BK2 which do not account for particle properties cannot accurately predict the measured values of the fluctuations.

3.1.3. Local measurement of solid volume fraction fluctuations

Initial measurements of the local solid fraction fluctuations in a liquid fluidized bed were conducted by Hashemi (2013) for spherical glass particles in a narrow range of particle sizes (2 to 4 mm). He used Electrical Impedance Tomography (EIT) for his measurements. Electrical tomography is an umbrella term for a group of non-invasive techniques which can provide reliable local information on the phase volume fraction in two-phase flows. In the last few decades, electrical tomography has been used by numerous researchers to characterize the flow parameters of multiphase industrial and research systems (Dickin and Wang, 1996; Dong et al., 2003; Dyakowski et al., 2000; George et al., 2000; Ismail et al., 2005; Wang et al., 2005; York, 2001). The main advantage of EIT over optical techniques is that it can operate on concentrated and even opaque suspensions.

In a recent study (Marefatallah et al., 2019, Chapter 2 of this thesis), we conducted measurements of the local solid volume fraction fluctuations for Delrin spherical particles with a low St_t. The results of this study (Marefatallah et al., 2019), along with earlier work by Hashemi (2013) showed that the distribution of the fluctuations was non-uniform along the bed cross-section.

In the current study, a high-speed EIT system was used to characterize the local volume fraction fluctuations of the solid phase for different types of particles in a liquid fluidized bed. These include particles with a wide range of St_t. To our knowledge, this is the first study that measures local volume fraction fluctuations for a wide range of particle properties in a fluidized bed. Also, the cross-sectional averages of the local measurements of this study are compared with the previous experimental measurements to provide a baseline comparison. Furthermore, the prediction accuracy of the existing models was assessed with the experimental data.

3.2. Experimental procedures

In this study, three different solid particles have been tested to measure the local solid fraction fluctuations in a liquid fluidized bed. All particles were mono-sized spherical beads whose important properties are listed in Table 3.2. The liquid phase was tap water at room temperature. A small amount of NaCl was added to the water to increase the conductivity of the continuous phase. The amount of salt added was [NaCl] = 0.85 g/L and 2.83 g/L for the nonconductive (nylon and glass) and conductive (steel) particles, respectively.

A vertical loop consisting of a circular fluidized bed section with dimensions of 10.16 cm I.D. and 2 m height was used. A schematic of the experimental apparatus is shown in Figure 3.1.

Table 3. 2. Particle properties

Material	d_p (mm)	ρ_s(kg/m^3)	u_t (cm/s)	Re_t	St_t	n
Nylon	6	1150	15.9	957	122	2.4
Glass	6	2540	52.1	3125	882	2.4
Steel	4.5	7950	95.8	4312	3809	2.4

A transparent section made of Plexiglas was located at the bottom of the fluidized bed to allow for visual observation of the flow. The measurement section was located in the middle of the bed with built-in EIT electrodes. Particles were added from the top, and water was pumped to the bed from the tank using a centrifugal pump. Prior to water's entry to the bed, its flow rate and temperature were measured and recorded, using an orifice plate with a Validyne differential pressure transducer and a thermocouple, respectively. A 15 cm tall flow straightener section was also located before the bed entrance.

For the measurement of the solid fraction fluctuations, a dual sensor high-speed EIT system was used: Z8000 ITS (Industrial Tomography Systems Co, Manchester, UK). The size of each EIT electrode is 1 cm by 1 cm (width by height). Electrodes are located at equal distances around the bed periphery. The EIT measurement protocol involves electrical excitation of one pair of electrodes while recording electrical potentials from the remaining pairs. The electrical excitation was then applied to adjacent pairs of electrodes until a full cycle of excitation and voltage measurements were performed at each frame of measurements. After a complete rotation, a conductivity map was reconstructed based on the acquired voltages in each measurement (Dyakowski et al., 2000).

At each desired bulk solid fraction ($\overline{C}$), when the bed of particles was fully fluidized, the instantaneous solid volume fraction was measured. For each data point, 10 consecutive blocks of measurements were recorded. Each block consisted of 8000 frames. The sampling frequencies were 1186 and 600 frames per second (fps) for nonconductive and conductive particles, respectively. For each frame of measurement, a 316-pixel conductivity map was reconstructed. At each pixel, the instantaneous solid volume fraction was obtained using Maxwell's equation (Dyakowski et al., 2000). For each block of measurements, the time-averaged solid fraction was calculated by averaging over the 8000 frames. Then Root Mean Square (RMS) solid fraction fluctuations at each pixel were calculated based on the local time-averaged value. The values reported below were obtained by averaging each of these parameters over the 10 measurement blocks (repeats). For each data point shown in this study the observed white noise in the measurements is subtracted before RMS calculations.

3.3. Results and discussion

3.3.1. Time-averaged and local RMS solid fraction fluctuations

The time-averaged solid fraction distributions were calculated over the 316 pixels of the bed cross-section. Selected bulk solid volume fractions of each particle type are shown in tomograms in Figure 3.2. The time-averaged distribution of the particles was nearly uniform and equal to the bulk solid fraction for all the particles tested (Figure 3.2). It should be noted that for the high-inertia particles at higher bulk solid fractions, the time-averaged distribution of the particles was slightly higher at the bed center resulting in a slight non-uniformity. This is probably because as the solid density increases, the density ratio (solid density to fluid density) increases. This ratio is an important factor in determining the flow regime in fluidized beds (Didwania and Homsy, 1981). By increasing the density ratio, the fluidization regime becomes more inhomogeneous because the density ratio approaches that of gas–solid fluidization (classic bubbly fluidization). And in general, gas–solid fluidizations are more inhomogeneous than liquid fluidizations, e.g. growth rate of voidage disturbance is predicted to be an order of magnitude larger for gas–solid compared to that of solid–liquid fluidized beds (Didwania and Homsy, 1981).

The local distribution of the RMS solid fraction fluctuations is shown in Figure 3.3. For each particle, three bulk solid fractions are presented: the lowest and highest values of $\overline{C}$ tested as well as the bulk fraction at which the highest magnitude of the RMS was observed. Tomograms in this figure show that the magnitude of the fluctuations was not uniform along the bed cross-section. Higher values of the fluctuations near the wall zone were observed for all particles and all bulk fractions tested. A similar trend was observed by Hashemi (2013) and Marefatallah et al. (2019) for glass spheres (2, 3, and 4 mm) and Delrin spheres (3.34 mm), respectively. These trends will be further investigated in the following section by comparing the average radial distribution of RMS fluctuations for the different cases.

3.3.2. Radial distribution of the RMS fluctuations

Figure 3.4 illustrates the radial distribution of the solid fraction fluctuations for the nylon, glass, and steel beads. In these graphs, the X-axis shows the dimensionless radial position, defined as the distance from the center of the bed divided by the bed radius. To obtain each data point shown in these graphs, RMS fluctuations are averaged over all pixels that are located at the same distance from the center (i.e. azimuthal averages). The trend of changes in the RMS by moving from the bed center towards the wall is similar for all particles at all values of $\overline{C}$, i.e. the magnitude of fluctuations increases by increasing the distance from the bed center. For the nylon particles, the magnitude of the RMS fluctuations was 2 to 3 times higher in the near the wall region compared to that at the center of the bed (Figure 3.4.a). This ranges for this ratio were 1.65 to 3 and 1.2 to 2 for the glass and steel particles, respectively (Figures 3.4.b and 3.4.c). The higher magnitude of the fluctuations at the wall zone is most probably because, in addition to the particle–particle and particle–fluid interactions, particle–wall collisions occur in this region. The other trend that is common among the three particle types is that at any given radial position and at the lower range of bulk solid fraction, by increasing $\overline{C}$, the magnitude of the RMS fluctuations increases. It reaches a maximum at $\overline{C}$=0.30, 0.54, and 0.44 for the nylon, glass, and steel beads, respectively. After this maximum, for all the particles, the RMS fluctuations decrease as $\overline{C}$ approaches C_{max}.

A slight increase in the local fluctuations at the bed center, observed for nylon (at $\overline{C} \geq 0.45$) and glass (at $\overline{C}$=0.54), was more recognizable for steel particle at high bulk solid fractions ($\overline{C} \geq 0.44$). This was also seen for Delrin particles at $\overline{C} \geq 0.44$ (Marefatallah et al., 2019). The reason why this slight increase is observed at the bed center for all the particles at high bulk solid fraction is not clear at this stage. It might be connected to the non-uniformity observed for the high-density particles at the bed center at high bulk solid fraction, shown in Figure 3.2.

For a better comparison of the magnitude of the local fluctuations for different particles, Figure 3.5 shows the radial distributions for all three particles tested in the current study along with those of the Delrin beads from our earlier work (Marefatallah et al., 2019). The selected values

for $\overline{C}$ shown in this figure are the ones at which the lowest and highest magnitude of the RMS fluctuations were observed for each type of particle. Therefore, at any given radial position, the lines shown in this graph represent the bottom and top boundaries of the range of changes in the RMS fluctuations for each particle. The magnitude of the fluctuations for steel particle was found to be significantly higher than those of the medium- and low-Stokes particles, i.e. an order of magnitude larger than those of the Delrin beads. At any given radial position, increasing St_t resulted in an increase in the magnitude of the fluctuations. Also, the range of changes in the magnitude of the RMS fluctuations widened as St_t increased. The results shown in Figure 3.5 shows that the particle type (size and density) does not have a significant effect on the shape of the radial distribution of the RMS fluctuations. For all the particle types tested here, RMS had its lowest magnitude around the bed center and highest values at the near the wall zone.

The results shown in Figures 3.3 to 3.5 illustrate that the significant changes to the magnitude of RMS fluctuations happen at $0.45 < {}^{r}/_{R} \leq 0.95$. Based on this observation, two important zones can be identified for the characterization of the fluctuations in the bed cross-section: a wall zone and a core zone. The wall zone is the narrow strip by the wall which has the highest magnitude of fluctuations for all the tested cases. The core zone consists of the pixels located in the ${}^{r}/_{R} \leq 0.45$ region. The magnitude of fluctuations was at its lowest value in this region and did not change significantly with distance from the bed center. It should be noted that the 0.45 value is chosen based on the experimental results of this study for four particles types. The size of the core zone might be different for other fluidization systems, especially when D/d (bed diameter to particle size) are different from the values of this study. We propose that for the modeling and experimental studies of local fluctuations in the bed, for the estimation of the magnitude of the fluctuations at any given radial positions, it would be sufficient to only model/measure the magnitude of fluctuations in these two zones. Further analyses of the ratio of RMS values at these zones are discussed in the next section, which will also support the claim that the RMS fluctuations over the whole cross-section can be estimated by knowing the values at the core- and wall-zone. Figure 3.6 illustrates these two zones in the 316-pixel reconstruction map used in this study.

3.3.3. Comparison with other experimental works

As mentioned earlier, the experimental data published in the literature for the fluctuating component of the solid fraction are spatially averaged over the bed cross-section. In order to compare the results of this study to the experimental work done by Zenit and Hunt (2000) and Didwania and Homsy (1981), the RMS fluctuations are averaged over the 316 reconstructed pixels. The values for these averages are shown in green symbols in Figure 3.7 for all three types of particles. However, because of the significant changes in the RMS values over the bed cross-section (Figures 3.3 to 3.5), a single value (full cross-sectional average) cannot give a complete picture of the fluctuations in the bed. Therefore, the values for the magnitude of the fluctuations at the wall zone and core zone are also shown in Figure 3.7 by red and blue symbols, respectively. These data points are obtained by averaging the RMS fluctuations over the pixels located in each zone (Figure 3.6).

The extra perspective provided by dividing the cross-section into wall and core zones provides insight into an issue observed in Zenit and Hunt's data (2000). When they initially compared their data to the Buyevich and Kapbasov model predictions (Buyevich and Kapbasov, 1994), they found an unsatisfactory match, which they explained by saying that their measurement device was picking up both large- and small-scale fluctuations while the model only predicts small-scale fluctuations. To account for this discrepancy, they applied a high-pass filter to the data and found a much better match with the models. However, the current results, presented in Figure 3.7, show that the wall zone data are close to Zenit and Hunt's (2000) unfiltered data while the core zone results are close to the filtered data. This result implies that Zenit and Hunt's measurement technique, which obtains only cross-sectional averaged data may have been biased toward near-wall fluctuations.

There is also another difference between the trend of the current results and the measurements performed by Zenit and Hunt (2000). Their original data series has a local maximum at $\overline{C} \approx 0.45$ (Figure 3.7). This local maximum was not observed in our measurements for low- and medium-Stokes particles. Zenit and Hunt suggested that this maximum is linked to the large-scale fluctuations traveling in a vertical direction since it disappeared after high-pass filtering (Zenit

and Hunt, 2000). This difference between the two measurements can be related to the different bed sizes used in each study. Although the particle sizes and densities between the two studies were very close, the bed diameter was D= 5.08 cm in the results presented by Zenit and Hunt's (2000), which is half the size of the bed in this study. The parameter D/d (bed diameter to particle size ratio) is especially important for the nylon and glass particles because these two are the largest particles tested in both studies (d= 6 mm). However, for the steel particles (d=4.5 mm), a similar behavior (local maximum) was seen at $\overline{C}$ = 0.45. These observations confirm that some of the large-scale fluctuations observed in their apparatus were probably eliminated from the flow configuration in the current fluidization system due to the higher values of D/d in the current study.

In Figure 3.7(a), the black circles are data points from Didwania and Homsy (1981) obtained for Ballotine spheres ($\rho_s = 3990\ \mathrm{kg/m^3}, d_p = 1.1\ \mathrm{mm}, u_t = 0.25\ \mathrm{m/s}, St_t = 120$). Although the particle size and density of the Ballotine and nylon spheres tested in this study were significantly different, their values of St_t were similar. The observation that these two particle types exhibited similar magnitudes of RMS fluctuations despite their differing paramters supports the hypothesis that RMS fluctuations are primarily driven by St_t alone (Zenit and Hunt, 2000). It should be noted that this hypothesis is only expected to be true when D/d is sufficiently large.

The ratios of the magnitudes of the fluctuations at the wall zone, core zone, and the full cross-section values are shown in Table 3.3. The values shown in Table 3.3 suggest that for all particles at any given $\overline{C}$:

$$\frac{\text{RMS fluctuations}_{\text{wall}}}{\text{RMS fluctuations}_{\text{full cross-section}}} = \frac{\text{RMS fluctuations}_{\text{full cross-section}}}{\text{RMS fluctuations}_{\text{core}}}$$

The importance of this relationship is that if one could measure or model the values of any two paramaters among these three parameters (wall, core, full-cross sectional averaged values of the RMS fluctuations), the third one can be easily calculated. This also supports our proposal presented in previous section that modeling or measurements of RMS at the core- and wall-zone are sufficient to model local RMS flucutaions at ay radial postions.

Table 3. 3. Ratios between the magnitude of RMS fluctuations at different zones

	$\frac{\text{RMS fluctuations}_{\text{wall}}}{\text{RMS fluctuations}_{\text{full cross-section}}}$	$\frac{\text{RMS fluctuations}_{\text{full cross-section}}}{\text{RMS fluctuations}_{\text{core}}}$
Steel	1.3 ± 0.06	1.3 ± 0.10
Glass	1.6 ± 0.14	1.6 ± 0.15
Nylon	1.7 ± 0.07	1.7 ± 0.09
Delrin	1.8 ± 0.04	1.7 ± 0.10

3.3.4. Comparison with the model predictions

Figure 3.8 shows the magnitude of the fluctuations measured for the particles tested in this study along with Delrin spheres (Marefatallah et al., 2019) against the values predicted by the three models proposed by Buyevich and Kapbasov (Buyevich, 1971; Buyevich and Kapbasov, 1994), i.e. Models B, BK1, and BK2.

The maximum packing concentration, C_{max}, is assumed to be equal to 0.6 for plotting Model B and BK2 in this figure. At any given bulk solid fraction, the experimental data points shown in this figure are the full-cross-section averaged values. All three models overpredict the magnitude of fluctuations. However, as particle Stokes number increases, the accuracy of the predictions for all three models improves.

An important assumption in developing Models BK1 and BK2 was that the main contributor to the fluctuations is particle–particle interactions and that the fluid impact is negligible (Buyevich and Kapbasov, 1994). However, in reality, the fluid–particle interactions become more dominant as St_t decreases. Therefore, by increasing St_t the measured values of magnitudes of fluctuations get closer to the values predicted by these models (Zenit and Hunt, 2000). Zenit and Hunt (2000) made this same observation with their experimental data in comparison to the Buyevich and Kapbasov models (1994).

In addition to the difference in overall magnitude, the trend of changes in the RMS fluctuations with $\overline{C}$ is not consistent for all particles. For the medium- and high-Stokes particles, the RMS

fluctuations continuously increase with increasing $\overline{C}$, and there is a sudden decay when $\overline{C}$ gets close to the C_{max} values. However, for the low-Stokes particles, there is a local maximum at $\overline{C} \approx 0.3$ which is similar to the predictions of Model BK1 and BK2. Overall, at low St_t, Models BK1 and BK2 make better predictions, but as St_t increases, experimental data transitions to a trend that is better predicted by the original Buyevich model, Model B (Buyevich, 1971). Although this model was developed based on the assumption of a macroscopically uniform system (Buyevich, 1971), better agreement between predictions of Model B and experimental measurements (compared to Model BK1) were reported for liquid (Buyevich and Kapbasov, 1999) and gas (Sergeev et al., 2004) fluidization systems.

For glass and steel particles, if a scaling factor is incorporated into the Buyevich model (1971), the values predicted by this model will overlap with the majority of data points obtained in this study (Figure 3.9):

$$\overline{C_r'^2} = SF * \overline{C_r}^2 \left(1 - \frac{\overline{C_r}}{C_{max}}\right) \tag{3.1}$$

This scaling factors used in the plots were 0.031 and 0.015 for steel and glass particles, respectively. A non-linear least squares fitting method was used to obtain these scaling factors. One of the reasons why Model B overpredicts the values of the RMS fluctuations is that this model only considers the statistical positioning of the particles at a fine scale and does not account for the effect of flow at large-scales in the bed (Buyevich, 1971; Buyevich and Kapbasov, 1999). However, although statistically there is a certain variation in the positions, large-scale fluctuations tend to re-distribute solid particles in a fairly homogenous manner closer to equilibrium positions, which could result in an effective damping of the statistical effect. Therefore, these scaling factors could represent this damping effect caused by the large-scale flow patterns on the solid fraction fluctuations in a fluidized bed. In Figure 3.9, we only plotted glass and steel particles since the Buyevich model only had a good prediction of the trend of changes of RMS for these two particle types among the four types of particles tested here.

To analyze the performance of Model G in predicting the experimental values of this study, a non-linear least squares fitting method is used to obtain the scaling factor (SF) for each data set.

The values obtained for the scaling factor of the best fit are shown in Figure 3.10(a) to (d). The scaling factor values in this study for nylon and steel are different from those reported by Gevrin et al. (2010). They reported 0.025 and 0.06 for nylon and steel, respectively, while the values found for the best fit in this study are 0.09 and 0.21 for nylon and steel, respectively (for the case of full cross-sectional-average). This difference shows that the scaling factor seems quite sensitive to factors that are not currently understood. So, despite the acceptable match in trend, more information will be needed to predict scaling factors correctly.

To obtain Figure 3.10, C_{max} is set equal to 0.6 in Model G and the drag coefficient of a single particle (C_{D0}) was calculated as follows (Schiller and Naumann, 1933):

$$C_{D0} = \frac{24}{Re_0}\left(1 + 0.15Re_0^{0.687}\right) \tag{3.2}$$

$$\text{where } Re_0 = \frac{\rho_f d_p u_0}{\mu_f} = \frac{\rho_f d_p u_t (1-\overline{C})^n}{\mu_f} \tag{3.3}$$

For low-Stokes particles, predictions by Model G show a good agreement with the experimental results in the range of $\overline{C} \leq 0.45$. However, for the medium- and high-Stokes particles, the model cannot predict the trend of changes or the magnitude of the fluctuations. The scaling factors obtained for each zone for low-Stokes particles are shown in Table 3.4. For both of the particles tested, the ratio of the scaling factors was found to be consistent. Therefore, for low-Stokes particles, the scaling factors for the wall and core zones can be obtained from that of the full cross-section. It should be noted that the values found for the scaling factors increase by increasing St_t. This suggests a possible relationship between this coefficient and St_t that requires further investigation.

Figures 3.8 and 3.10 show that all three BK1, BK2 and G models (Buyevich and Kapbasov, 1994; Gevrin et al., 2010) provide a better prediction of the trend of the RMS fluctuations for low-Stokes particles but lose their accuracy as St_t increases. Both models have the strong assumption that the flow is homogeneous everywhere in the bed (Buyevich and Kapbasov, 1999). To further examine the breakdown of this assumption, the solid fractions of nylon (low St_t) and glass (medium St_t) particles at $\overline{C} \approx 0.45$ are shown in Figure 3.11.

Table 3. 4. Scaling factors obtained for Model G in different zones

	SF_{full} (full cross-section average)	SF_{wall} (wall zone)	SF_{core} (core zone)	$\frac{SF_{wall}}{SF_{full}}$	$\frac{SF_{core}}{SF_{full}}$
Delrin	0.05	0.09	0.03	**1.8**	**0.6**
Nylon	0.09	0.16	0.05	**1.8**	**0.6**

These results show that although the appearance of low-frequency fluctuations at higher $\overline{C}$ is observed for both particles, the magnitude of these fluctuations is significantly higher for the glass particles. This suggests that a fluidized bed of glass particles is more inhomogenous at higher $\overline{C}$ compared to nylon beads. From the results shown so far, the homogeneity assumption is thererfore not necessarily valid for the medium- and high-Stokes particles.

However, Model BK1 and G make better predictions of the trend of RMS fluctuations of low-Stokes particles as these systems are relatively more homogenous. This observation is consistent with Buyevich and Kapbasov's finding that considering the large-scale fluctuations in addition to the small-scale fluctuations improved their models' predictions of the experimental measurements (Buyevich and Kapbasov, 1999). They observed that use of Model B instead of Model BK1 improved their model for the prediction of particulate pressure in a fluidized bed. This suggests that Model B makes a better prediction of fluctuations when the flow is inhomogeneous, which occurs at higher bulk solid fractions when large-scale fluctuations dominate.

3.4. Conclusions

The local instantaneous solid volume fraction for three types of particles with low-, medium- and high-Stokes numbers ($122 \leq St_t \leq 3809$) were measured. The time-averaged concentration profiles showed that the distribution of the particles in the bed was uniform for most of the cases tested. The magnitude of fluctuations was found to be significantly higher in the near-wall region than near the bed's center. Depending on the particle type, this value was 1.2 to 3 times higher

than the values at the center of the bed. Investigating the effect of St_t on the RMS fluctuations showed that particles with higher St_t have higher values of fluctuations at any given local radial position. This finding was in agreement with Zenit and Hunt's (2000) results that St_t plays an important role in the determination of the cross-sectional-averaged RMS fluctuations.

For the characterization of the fluctuating component of the solid fraction, two main zones in the bed cross-section need to be studied: the wall zone and the core zone. The magnitude of the RMS fluctuations was minimum at the core zone and did not change significantly with changing the distance from the center. The wall zone, consisting of locations located near the wall, had the maximum values of fluctuations for all the cases.

Comparison of the cross-sectional-averages of the current data with the existing experimental data in the literature showed an acceptable agreement. For all particles, RMS values in the wall zone were found to be closer to the values reported by Zenit and Hunt (2000) than the core-zone values. This could be an indication of a possible bias in their measurement technique towards the magnitude of the fluctuations at the near the wall zone.

Results of this study were also compared to the prediction of the existing models in the literature. The models proposed by Buyevich and Kapbasov (Buyevich, 1971; Buyevich and Kapbasov, 1994) were found to overpredict the overall values of the RMS fluctuations, which is a well-known result. However, the models were also compared for their ability to predict the trend of changes in the RMS fluctuations. In this regard, the earlier Buyevich model (1971) better predicted this trend for medium- and high-Stokes particles. On the other hand, the recent models by Buyevich and Kapbasov (1994) better predicted this trend for particles with low St_t in the range of bulk solid fraction tested. The comparison with the semiempirical model by Gevrin et al. (2010) suggested that this model prediction is also better for the low-Stokes particles, especially at lower bulk solid fractions. For all models tested, in order to predict the overall RMS magnitudes, a specific scaling factor is required for each particle type. Although this scaling factor seems to be related to the particle properties and increases with increasing St_t, its exact relationship is still not clear. The need for a model that accounts for the particle properties, specifically particle

Stokes number, which can predict the magnitude of the fluctuations at high bulk solid fraction still exists.

Unlike the previous studies, this work provided local information on the fluctuating component of the solid fraction for a wide range of particle properties. Therefore, the results presented here can be used to directly examine the outcomes of the CFD models. Furthermore, by validating different assumptions made for model development, it can contribute to the improvement of the current simulations of the two-phase flows.

3.5. Figures

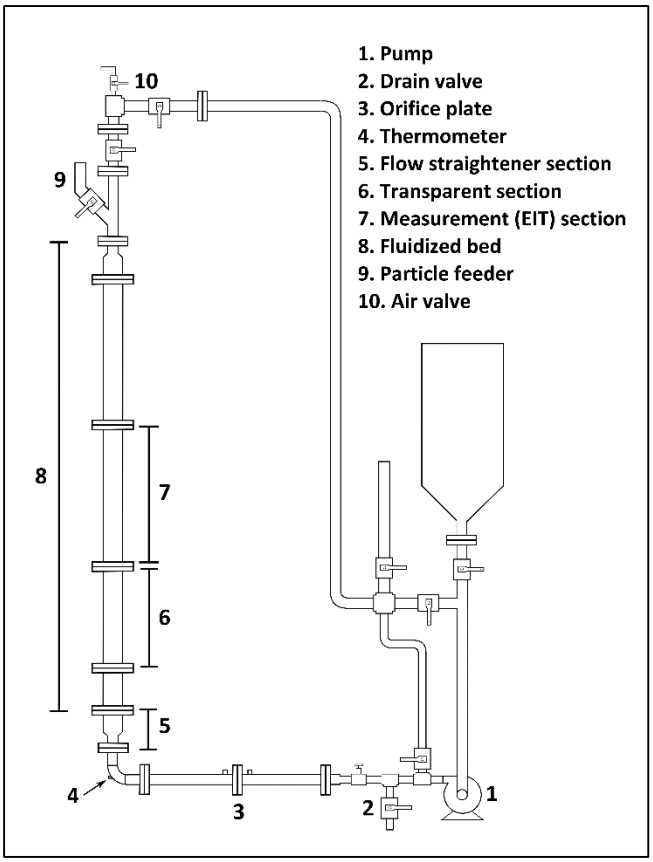

Figure 3.1. Schematic of the experimental apparatus

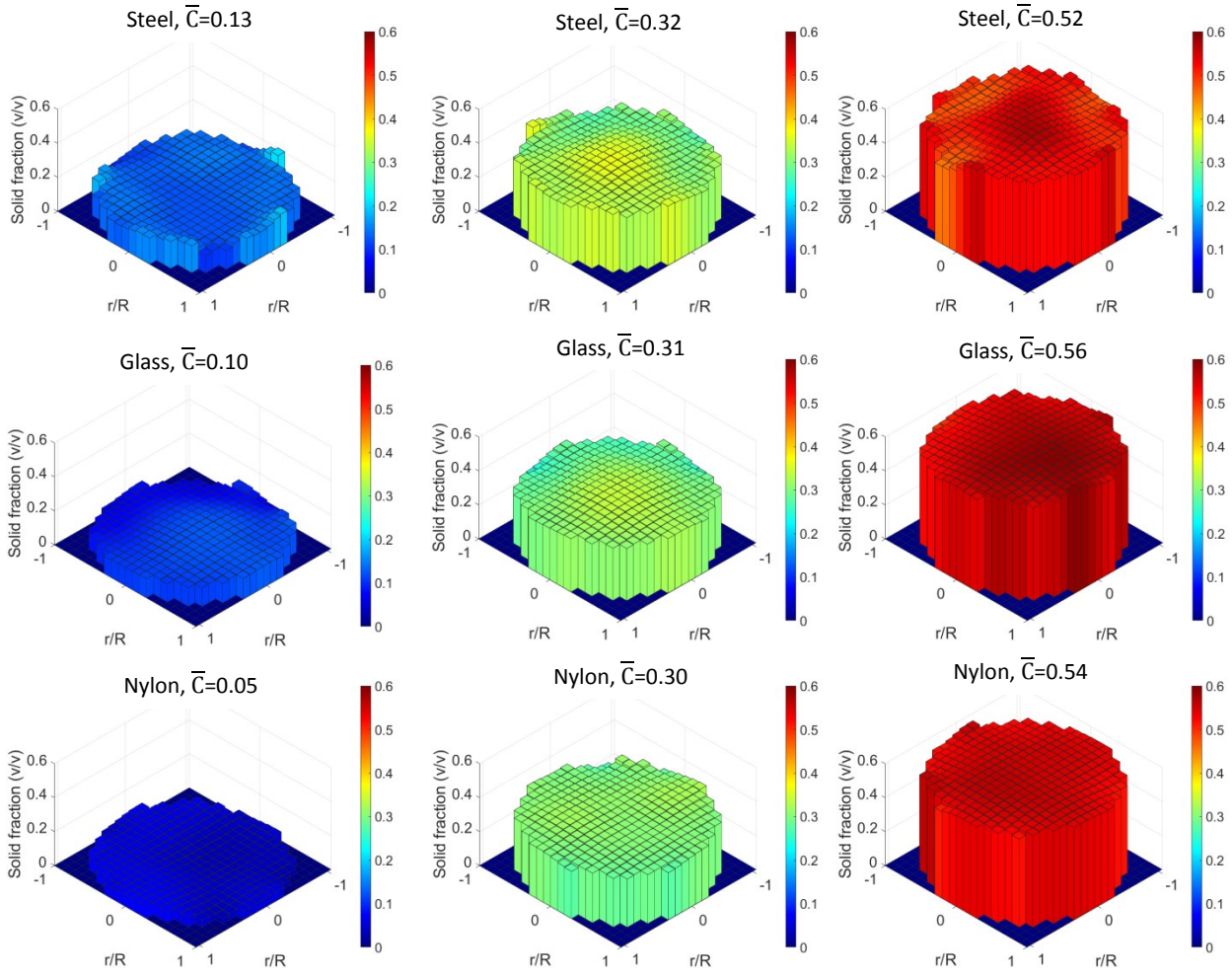

Figure 3.2. Time-averaged solid volume fraction distributions for nylon, glass, and steel particles.

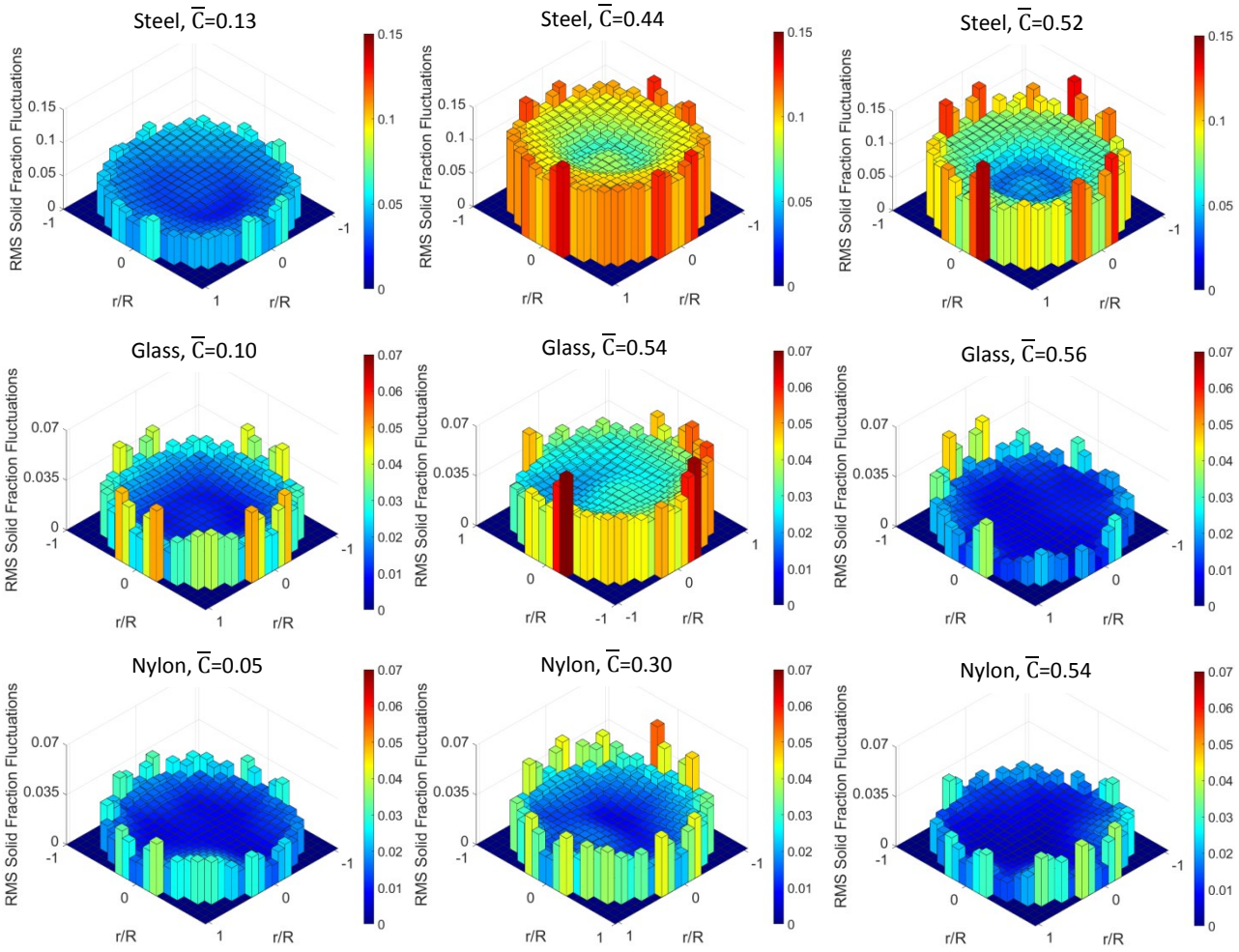

Figure 3.3. Local RMS solid volume fraction fluctuations for nylon, glass, and steel particles. Note that the scales of the z-axis are not the same across all tomograms.

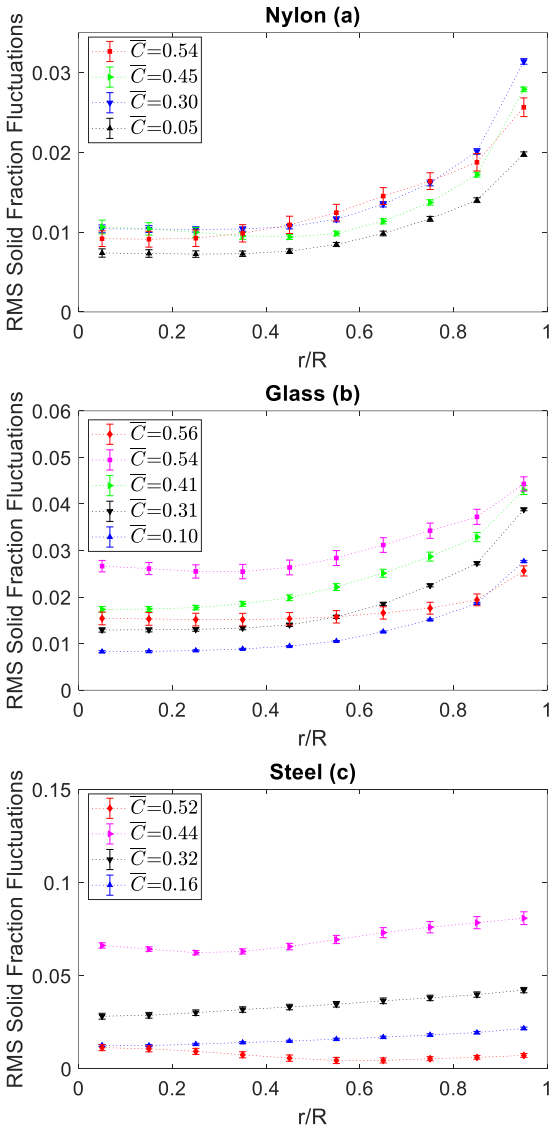

Figure 3.4. Nylon particles (a), glass particles (b), steel particles (c): Radial distributions of the RMS of solid fraction fluctuations for different bulk solid fractions. Error bars shown in this figure illustrate standard errors. Note that the scales of the y-axis are not the same across all plots.

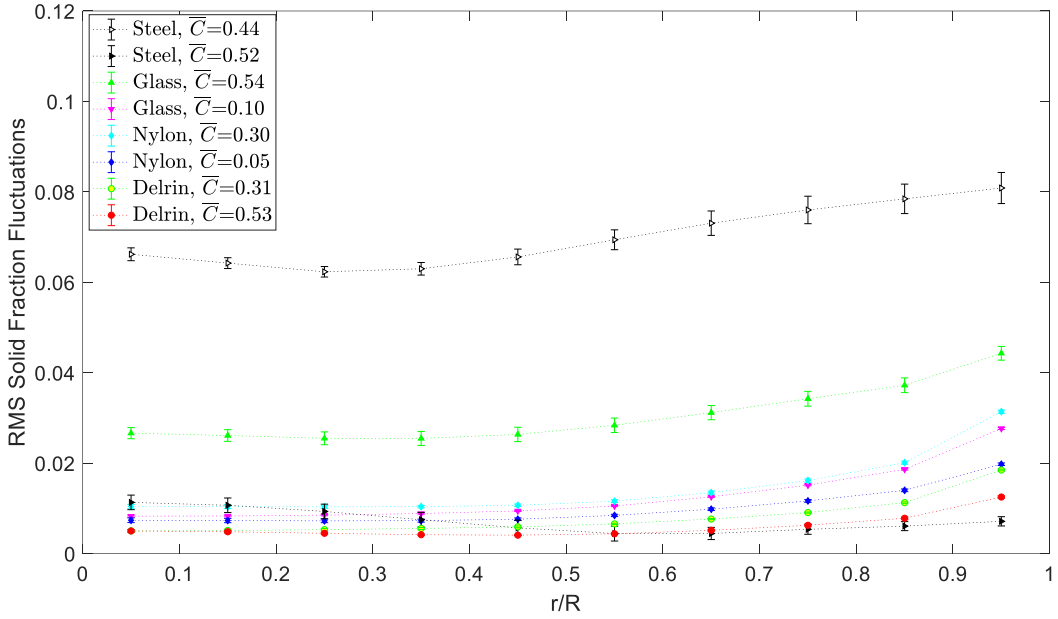

Figure 3.5. Radial distributions of the RMS of solid fraction fluctuations for Nylon, Glass, and Steel particles. Error bars shown in this figure illustrate standard errors. Delrin experimental data is from (Marefatallah et al., 2019)

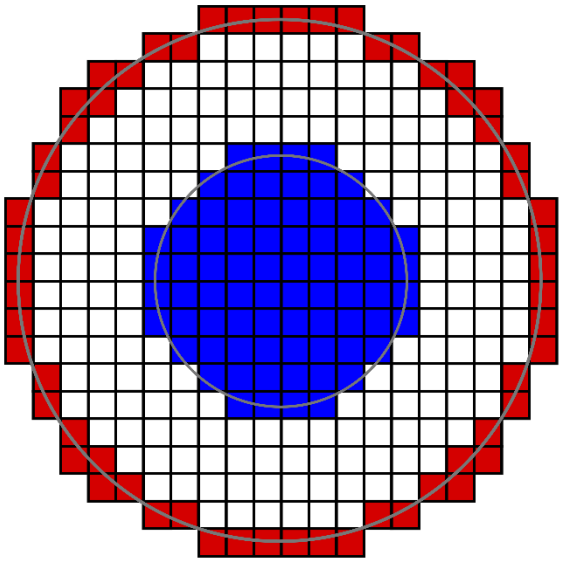

Figure 3.6. Wall zone (red pixels) and core zone (blue pixels) marked in the 316-pixel reconstruction map.

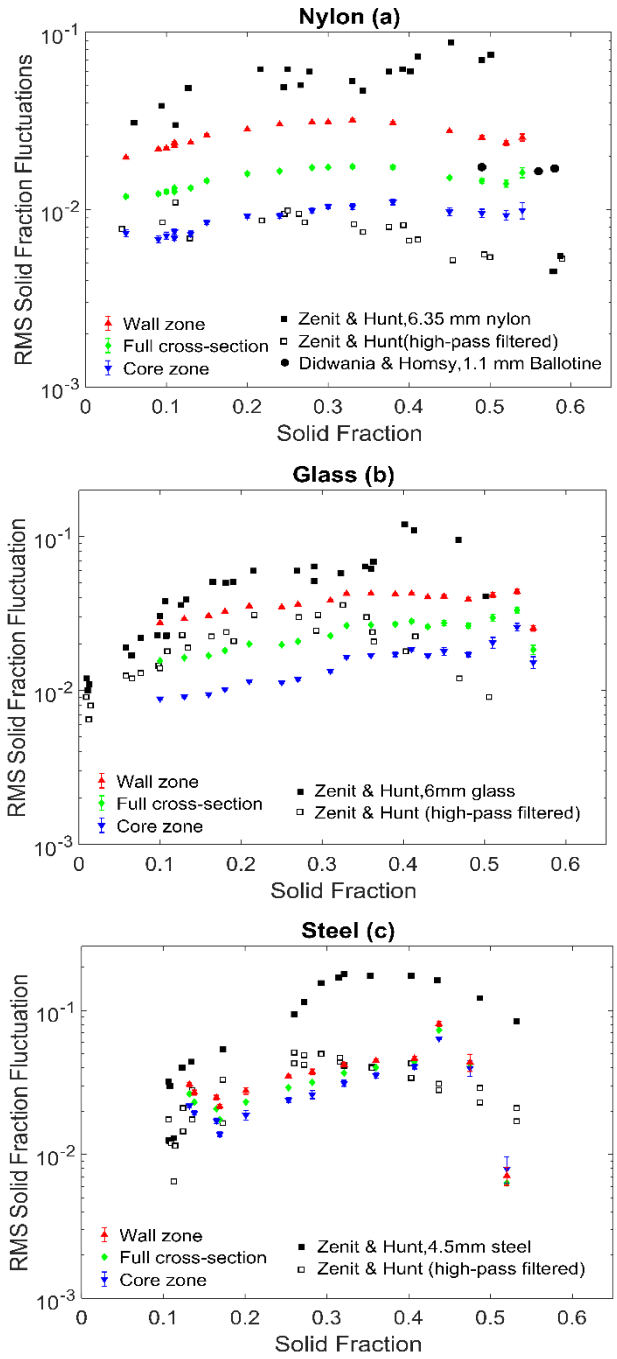

Figure 3.7. RMS solid fraction fluctuations as a function of solid fraction for nylon (a), glass (b), and steel (c) particles. Error bars shown in this figure illustrate standard errors. Experimental data from (Zenit and Hunt, 2000), and (Didwania and Homsy, 1981).

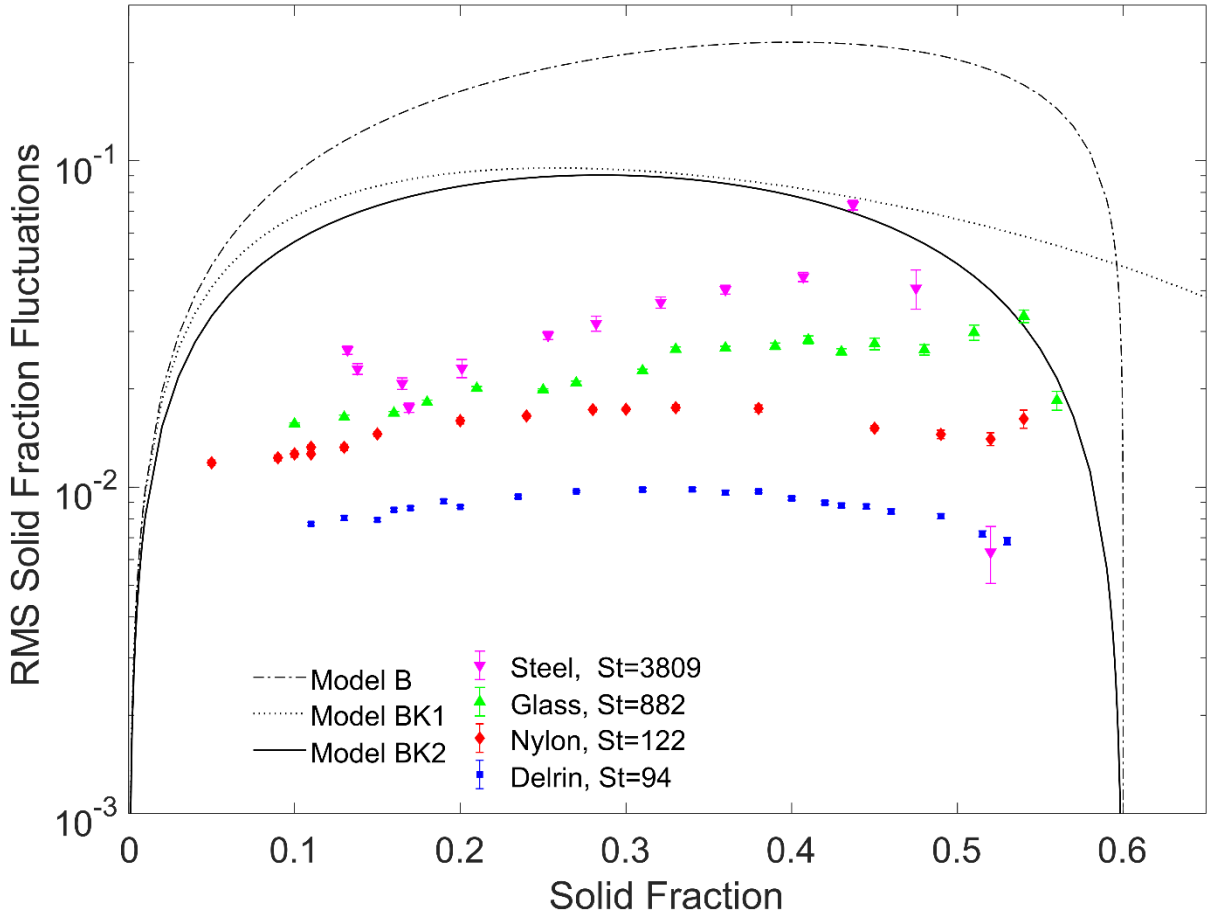

Figure 3.8. Full cross-sectional averaged values of RMS solid fraction fluctuations in comparison to predictions of Buyevich model (1971), Model B, Buyevich and Kapbasov models (1994), Models BK1 and BK2. Error bars shown in this figure illustrate standard errors. Delrin experimental data is from (Marefatallah et al., 2019)

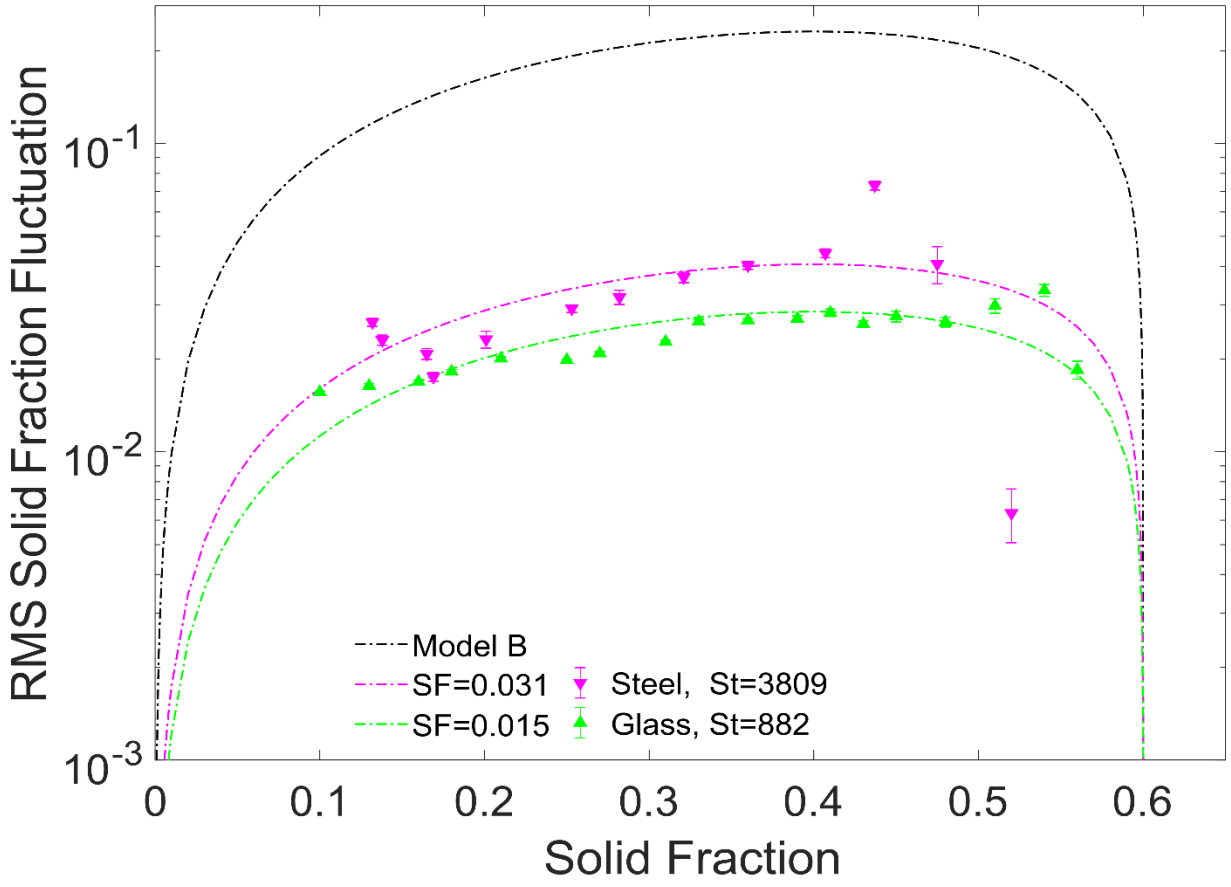

Figure 3.9. Full cross-sectional averaged values of RMS solid fraction fluctuations in comparison to predictions of Buyevich model (1971), Model B, and two scaling factors in Eqn (3.1). Error bars shown in this figure illustrate standard errors.

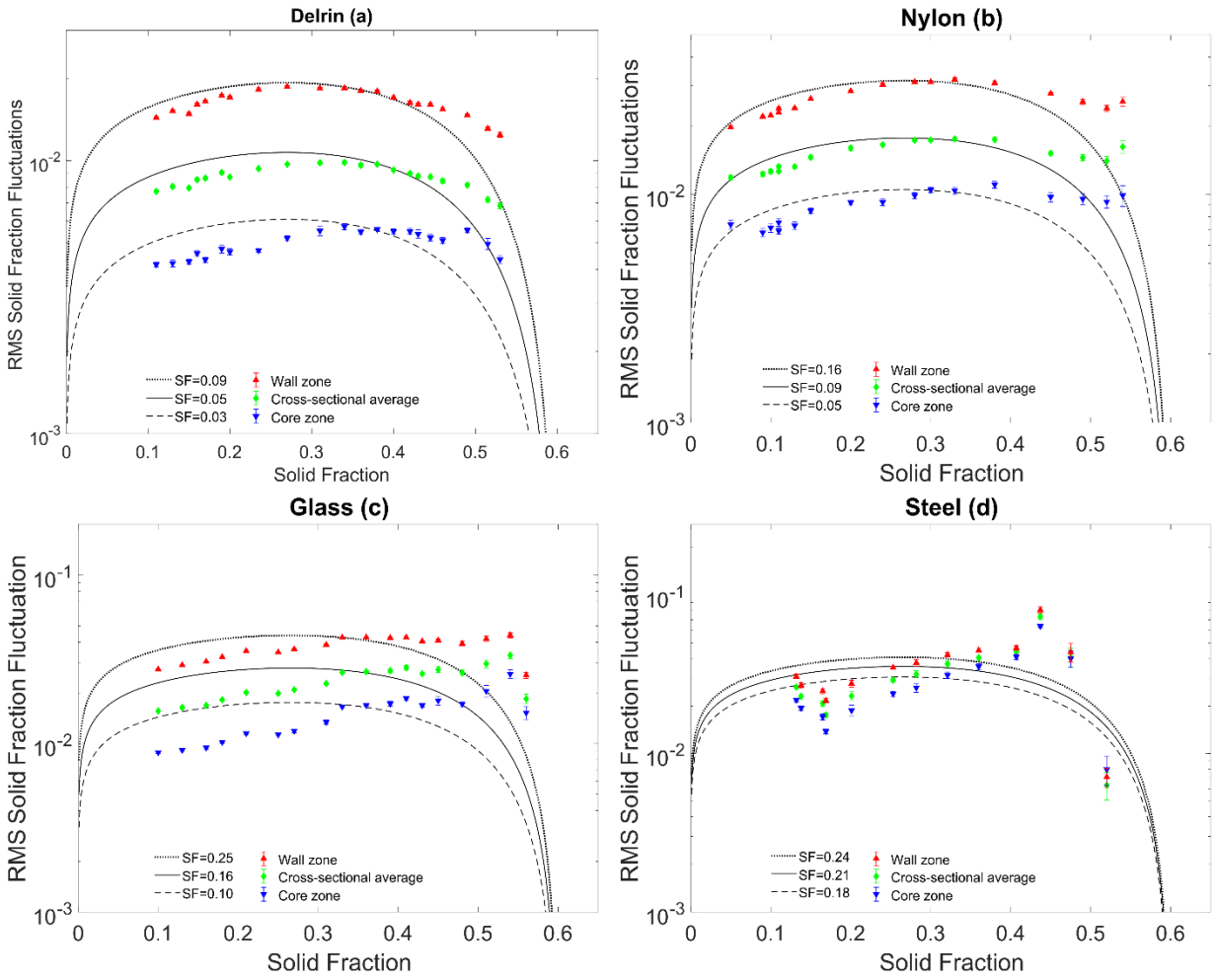

Figure 3.10. RMS solid fraction fluctuations in comparison to predictions of Gevrin et al. model (2010), Model G, applying different Scaling Factors (SF). Error bars shown in this figure illustrate standard errors. Delrin experimental data is from (Marefatallah et al., 2019).

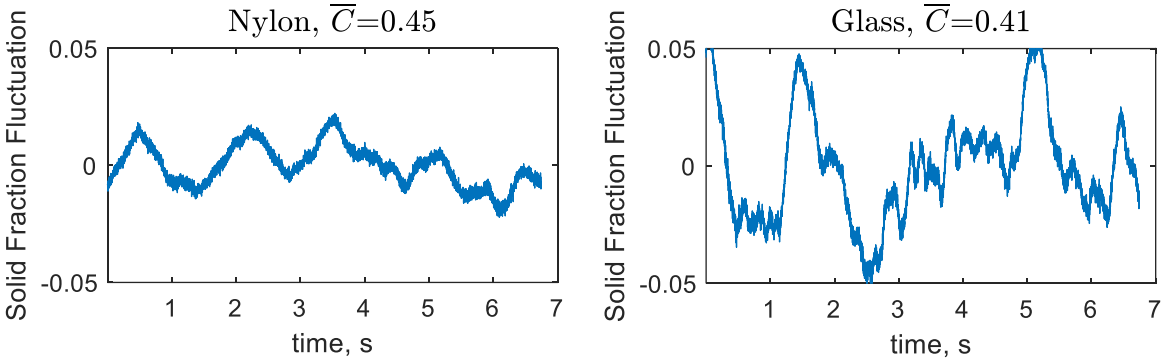

Figure 3.11. Solid fraction fluctuations for nylon (left) and glass particles (right) at r/R=0.55.

3.6. References

Buyevich, Yu.A. (1971). On the fluctuations of concentration in disperse systems The random number of particles in a fixed volume. Chem. Eng. Sci. *26*, 1195–1201.

Buyevich, Y.A., and Kapbasov, S.K. (1999). Particulate Pressure in Disperse Flow. Int. J. Fluid Mech. Res. *26*, 72–97.

Buyevich, Yu.A., and Kapbasov, Sh.K. (1994). Random fluctuations in a fluidized bed. Chem. Eng. Sci. *49*, 1229–1243.

Cornelissen, J.T., Taghipour, F., Escudié, R., Ellis, N., and Grace, J.R. (2007). CFD modelling of a liquid–solid fluidized bed. Chem. Eng. Sci. *62*, 6334–6348.

Derksen, J.J., and Sundaresan, S. (2007). Direct numerical simulations of dense suspensions: wave instabilities in liquid-fluidized beds. J. Fluid Mech. *587*.

Dickin, F., and Wang, M. (1996). Electrical resistance tomography for process applications. Meas. Sci. Technol. *7*, 247–260.

Didwania, A.K., and Homsy, G.M. (1981). Flow regimes and flow transitions in liquid fluidized beds. Int. J. Multiph. Flow *7*, 563–580.

Dong, F., Jiang, Z.X., Qiao, X.T., and Xu, L.A. (2003). Application of electrical resistance tomography to two-phase pipe flow parameters measurement. Flow Meas. Instrum. *14*, 183–192.

Dyakowski, T., Jeanmeure, L.F.C., and Jaworski, A.J. (2000). Applications of electrical tomography for gas–solids and liquid–solids flows — a review. Powder Technol. *112*, 174–192.

Epstein, N. (2002). Applications of Liquid-Solid Fluidization. Int. J. Chem. React. Eng. 1, 1-16

George, D.L., Torczynski, J.R., Shollenberger, K.A., O'Hern, T.J., and Ceccio, S.L. (2000). Validation of electrical-impedance tomography for measurements of material distribution in two-phase flows. Int. J. Multiph. Flow *26*, 549–581.

Gevrin, F., Masbernat, O., and Simonin, O. (2008). Granular pressure and particle velocity fluctuations prediction in liquid fluidized beds. Chem. Eng. Sci. *63*, 2450–2464.

Gevrin, F., Masbernat, O., and Simonin, O. (2010). Numerical study of solid–liquid fluidization dynamics. AIChE J. *56*, 2781–2794.

Hashemi, S.A. (2013). Velocity and concentration fluctuations in concentrated solid-liquid flows. PhD thesis. University of Alberta.

Ismail, I., Gamio, J.C., Bukhari, S.F.A., and Yang, W.Q. (2005). Tomography for multi-phase flow measurement in the oil industry. Flow Meas. Instrum. *16*, 145–155.

Marefatallah, M., Breakey, D., and Sanders, R.S. (2019). Study of local solid volume fraction fluctuations using high speed electrical impedance tomography: Particles with low Stokes number. Chem. Eng. Sci. *203*, 439–449.

Panneerselvam, R., Savithri, S., and Surender, G.D. (2007). CFD based investigations on hydrodynamics and energy dissipation due to solid motion in liquid fluidised bed. Chem. Eng. J. *132*, 159–171.

Sergeev, Y.A., Swailes, D.C., and Petrie, C.J.S. (2004). Stability of uniform fluidization revisited. Phys. Stat. Mech. Its Appl. *335*, 9–34.

Wang, M., Ma, Y., Holliday, N., Dai, Y., Williams, R.A., and Lucas, G. (2005). A high-performance EIT system. IEEE Sens. J. *5*, 289–299.

York, T.A. (2001). Status of electrical tomography in industrial applications. J. Electron. Imaging *10*, 608–620.

Zenit, R., and Hunt, M.L. (2000). Solid fraction fluctuations in solid–liquid flows. Int. J. Multiph. Flow *26*, 763–781.

Zhang, K., Wu, G., Brandani, S., Chen, H., and Yang, Y. (2012). CFD simulation of dynamic characteristics in liquid–solid fluidized beds. Powder Technol. *227*, 104–110.

Chapter 4. Spectral Analysis of Local Solid Volume Fraction Fluctuations in Fluidization of Particles with Low and High Stokes numbers: An Experimental Study

Material in this chapter is in preparation for submission as:

Marefatallah, M., Breakey, D., and Sanders, R.S. (2019). Spectral Analysis of Local Solid Volume Fraction Fluctuations in Fluidization of Particles with Low and High Stokes numbers: An Experimental Study.

4.1. Introduction

Solid–liquid fluidization systems are one of the common industrial and academic cases of multiphase flow systems. Sedimentation, mineral extraction from ores, and oil extraction from seeds in the food industry are examples of their applications (Epstein, 2002). To achieve maximum efficiency and minimum cost, the design and operation of industrial liquid fluidized beds should be based on validated computational models. However, since there are not enough simulation studies on solid–liquid fluidization, their operation is still based on empirical methods (Cornelissen et al., 2007; Panneerselvam et al., 2007; Zhang et al., 2012). Further, due to the lack of available local experimental data, the performance of the few modeling works done on liquid fluidization has only been qualitatively examined. Therefore, there is still a need for high-resolution, time-resolved experimental measurements along with reliable models that can predict the flow behaviour of liquid fluidized beds.

Current and future CFD simulations of liquid fluidization require local instantaneous experimental data to validate the reliability of their predictions. These experimental measurements can be used to examine different assumptions made in such simulations. Examples of these assumptions are the selected drag models, values selected for the coefficients of restitution, etc. (Cornelissen et al., 2007). The distribution of solid particles along the bed cross-section is an example of local instantaneous data that can be used to validate and improve these models.

In a previous study (Marefatallah et al., 2019a), we presented the local Root Mean Square (RMS) values of solid fraction fluctuations and compared the experimental measurements to the existing models. This study showed that the magnitude of the local solid volume fraction fluctuations is dependent on the particle properties, especially particle Stokes number. Since none of the existing models considered particle properties, the values predicted by these models did not match the measurements. In most cases, the models overpredicted the experimental values, especially at high solid volume fractions. Therefore, there is still a need for models that can accurately predict the magnitude of the fluctuations for different particle types over a wide range of bulk solid volume fractions. Developing such models requires local experimental data at

different conditions. In this study, local measurements were further analyzed, and frequency- and time-domain analyses were conducted. In addition to the study of the RMS fluctuations (Marefatallah et al., 2019a), frequency-domain analysis provides more information about the nature of the fluctuations in a fluidized bed. The power density spectrum of solid fraction fluctuations shows the distribution of the energy among fluctuations with different frequencies. From these spectra, dominant frequencies can be identified. Furthermore, fluctuations of different scales can be distinguished and isolated, i.e. large-scale and small-scale fluctuations in the bed. Moreover, the slope of the decay in the turbulence power spectrum can be compared to spectra associated with known flow behaviour to distinguish flow structure.

The power spectra of solid volume fraction fluctuations at different bulk solid fractions have been presented in previous studies (Gevrin et al., 2010; Zenit and Hunt, 2000). However, those results were limited to the cross-sectional average data. The unique opportunity of this study is that the power spectra and time signal analyses can be conducted at different radial positions in the bed cross-section. The obtained patterns of the local power spectra provide more information about the local small and large-scale structure of the flow. Furthermore, the local experimental data of this study can be used to validate the computational modeling of similar systems.

4.2. Methods and analysis

4.2.1. Experimental design

Local instantaneous solid volume fraction was measured for four different types of spherical particles in water. The properties of these particles are listed in Table 4.1. In this table, d_p, ρ_s, u_t are particle size, density, and terminal settling velocity, respectively. Re_t and St_t are calculated as follows:

$$Re_t = \frac{\rho_f u_t d_p}{\mu_f} \tag{4.1}$$

$$St_t = \frac{\rho_s}{\rho_f} \frac{Re_t}{9} \tag{4.2}$$

Where μ_f and ρ_f are fluid viscosity and density, respectively.

Table 4. 1. Properties of the spherical particles

Material	d_p (mm)	ρ_s(kg/m^3)	u_t (cm/s)	Re_t	St_t
Steel	4.5	7950	95.8	4312	3809
Glass	6	2540	52.1	3125	882
Nylon	6	1150	15.9	957	122

A high-speed Electrical Impedance Tomography (EIT) unit along with a vertical fluidized bed of 10.16 cm I.D was used. The electrode array of EIT measurement section was located 75 cm from the bottom of the bed. The electrode array is made up of 16 electrodes mounted around the interior wall of the vertical pipe. Voltage measurements from these electrodes were used to reconstruct a conductivity map of the bed cross-section consisting of 316 pixels. The solid volume fraction was calculated using Maxwell's equations (Dyakowski et al., 2000). More details of the experimental setup and procedures were explained in the previous works (Marefatallah et al., 2019a, 2019b).

4.2.2. Analysis

The electrical impedance tomogram analysis was done in the time and frequency domains. For each data point, ten measurement blocks, each with 8000 frames, were captured. To obtain the local time signals, the time-averaged value of the solid fraction was subtracted from the instantaneous values at each frame. The corresponding power spectral density was calculated using the Fast Fourier Transform (FFT).

An example of a recorded time signal and its corresponding power spectrum is shown in Figure 4.1. All spectra in this study are averaged over the ten measurement blocks. In all measurements, at high frequencies, white noise becomes the dominant part of the signal (Figure 4.1). The white noise power level was identified for each measurement and was subsequently subtracted from the measurements (Fischer et al., 2008). All the subsequent power spectral plots in this study show the spectra after this step.

The sampling frequencies (f_s) for the measurements of the nylon and glass particles were both 1186 frames per second (fps), while 600 fps was used for the steel particles. Lower EIT excitation frequencies were required for the conductive particles. This resulted in the use of a lower sampling frequency for steel particle. Additionally, a series of measurements were conducted for both the glass and steel particles at f_s=191 fps. Since the total number of captured frames was constant (8000 frames) for all the measurements, the sampling time was longer (41.9 seconds) for the measurements with the lower sampling rate. The longer sampling time improved the resolution at lower frequencies. A fourth-order high-pass Butterworth filter with a cut-off frequency of 1 Hz was applied to the time signals to eliminate the large-scale low-frequency fluctuations. The filter was implemented in the time-domain using a convolution.

4.3. Results and discussion

4.3.1. Effect of radial position

Figure 4.2 shows power spectra for different particles at different radial positions (left column). For a clearer visualization of the range of power spectra for each particle, in a separate graph, the spectra at the center and at the wall region are shown (right column). The amplitude of the power spectrum increases by moving from the center of the bed towards the wall zone. This increase occurs over the entire frequency range, as shown in Figure 4.2. However, the magnitude of this increase is not the same at the low frequency and high frequency ranges. In the case of nylon particles, the amplitude of the power spectra at the wall zone is 20 times higher than that of the bed center at low frequency ranges ($f \leq 1$ Hz) while this ratio is 50 for the wall to the center amplitude at the higher frequencies (1 Hz < f). For glass particles, by approaching the wall the amplitude of the power spectrum becomes 50 times higher than that at the bed center for high frequency ranges and 10 times higher for the low frequency ranges. For the case of steel particles, the amplitude at the wall is 2-3 times higher than at the bed center with negligible change in the shape of the spectrum. In summary, the amount of the increase in the magnitude of the power spectra is significant for the low and medium Stokes particles. In the case of the high Stokes particles (steel), although the amplitude of the power spectra increases, the difference between

the power spectra at the bed center and at the wall region is smaller. And, for the lower-Stokes particles in particular, the increase in magnitude is less significant for the lower frequency range.

All power spectra show maximum amplitudes at the frequency ranges of 1 Hz and lower. At frequencies above this maximum, the power spectra decay in all cases. For nylon particles, the slope of this decay does not change with radial position. For glass particles, the slope of the signal at the bed center ($r/R<0.35$) is slightly different from the rest of the radial positions. For $r/R=0.35$ to $r/R=0.95$ slopes of decay do not change by changing the radial position.

Figure 4.3 illustrates a sample of the time signals at four different radial positions for glass particles at $\bar{C}=0.31$. By increasing the distance from the bed center, the appearance of some low-frequency, high amplitude fluctuations can be observed. This is because at the low frequency ranges the amplitude of the wall zone power spectra is 10 times higher than that at the center of the bed. And since the low frequency fluctuations have the highest amplitude in the power spectra this change is magnified and can be visually recognized more easily than the fifty-fold increase in the high frequency range. These increases lead to an increase in the total magnitude of the solid fraction fluctuations at the wall region.

The time signals shown in Figure 4.3 show why it is important to study the solid fraction fluctuations at different locations in the bed cross-section. The peak-to-peak amplitude of the solid fraction fluctuation signal at the wall zone is almost three times higher than that of the bed center. However, the local time signals do not change significantly with changing radial position in the "bed core zone" (Marefatallah et al., 2019a), i.e. $r/R\leq0.55$, shown in the top two graphs in Figure 4.3.

The results shown in Figures 4.2 and 4.3 showed that by increasing the distance from the bed center there is a global increase in the magnitude of the fluctuations. Although the whole frequency domain experience this increase in the amplitude, it is more significant for the higher frequency ranges. It is most likely that the particle–wall collisions cause this increase in the amplitude of the fluctuations, especially at the higher frequency ranges. The reason behind the increase in magnitude of the low-frequency fluctuations is not clear at this stage. It might be due

to the high shear zone at the wall region magnifying the instability waves at this region. Or the presence of the wall intensifying the low frequency global waves in the bed at the wall zone. In either case, the lower-frequency, larger-scale waves would have to be driving an energy cascade in order to account for the significant increase in the high frequency fluctuations.

4.3.2. Effect of bulk solid volume fraction

Figures 4.4 (a), (b), and (c) show the solid fraction power spectra for nylon, glass, and steel, respectively, at different bulk solid fractions. For all the particles and at all bulk solid volume fractions, the power spectra have the maximum amplitude at the lowest frequency ranges. At higher frequency ranges, the spectra decay with a slope of -3. However, the extent of this slope and its range of frequencies shift by changing $\bar{C}$. By increasing $\bar{C}$, the -3 slope moves towards the lower frequency ranges and the extent over which the -3 slope dominates increases. For the low and medium stokes particles at $\bar{C} \approx 0.4$, this slope covers nearly the whole frequency range. At the highest $\bar{C}$ tested, (i.e. $\bar{C}$= 0.54 and 0.56 for the nylon and glass particles, respectively) a -5/3 slope appears at the high end of the frequency range. This region was also observed by Zenit and Hunt (2000) and Gevrin et al. (2010) for 6.35 mm nylon particles at $\bar{C}$=0.56. The possible relationship between the -5/3 slope at the high frequency range and the particle size is discussed in Section 4.3.3.

Figure 4.5 shows that the extent of the -3 slope of power spectra for the high-Stokes particles does not change significantly at the low and medium bulk solid fractions. However, at $\bar{C}$=0.48 this slope slightly moves towards the low-frequency ranges. At $\bar{C}$=0.52, only the magnitude of the lowest frequency range of the signal exceeded the noise level. The resolution of the spectra at these frequencies is not sufficient to measure the decay slope.

The power spectrum with a -3 decay slope represents a flow pattern similar to a 2D turbulent flow (Kraichnan, 1967; Lilly, 1969). Figure 4.4.a and b suggest that by increasing $\bar{C}$ the power spectra become more similar to that of a 2D turbulent flow (at a wider frequency ranges) and at $\bar{C} \approx 0.40$ the -3 slope takes over the whole frequency domain. The reason why the power spectra resembles a 2D turbulent flow can be because of the existence of instability waves acting as an external force coupled with the 3D turbulent flow. This force drives one of the degrees of

freedom so that the resulting flow pattern becomes similar two a 2D flow. This can also be interpreted from the velocity fields shown in Gevrin et al. (2010). The velocity profiles indicate that at the higher solid fractions more velocity vectors are aligned in the vertical direction and the number of circular patterns in the velocity fields is lower compared to the low $\bar{C}$ (Gevrin et al., 2010), indicating that the vertical motions are being constrained to the movement of the propagating waves. For all the power spectra shown in Figures 4.4 (a), 4.4 (b) and, 4.4 (c), at $\bar{C} \leq$ 0.4, the spectra exhibit a different decay slope ($\alpha > -3$) at the lower frequency ranges (prior to the -3 slope of the decay). The slope of the decay for this region is discussed in more details in Section 4.3.4.

Figure 4.6 (a) shows the solid fraction fluctuation time signals at five different $\bar{C}$ for the glass particles. By increasing $\bar{C}$, the peak-to-peak magnitude of the fluctuations increases at the range of $\bar{C} \leq 0.4$ and at $\bar{C}$=0.56 the peak-to-peak amplitude decreases compared to $\bar{C}$=0.40.

4.3.3. Effect of Stokes numbers

To study the effect of particle Stokes number, power spectra of the solid fraction fluctuation signals for four different Stokes numbers are illustrated against each other at different $\bar{C}$ in Figure 4.7. The amplitude of the noise was significantly higher for the case of the steel particles, which have the highest Stokes number. This led to the highest frequency shown in the power spectra for steel particles being smaller than the other three particles.

The RMS fluctuations are equal to the square root of the power density integral over the whole frequency range (Cook, 2012).

$$\sigma = \int_{-\infty}^{+\infty} \Phi(\mathrm{f})\mathrm{df} \tag{4.3}$$

$$\overline{C_r'} = \sqrt{\sigma} \tag{4.4}$$

where $\overline{C_r'}$ is the local RMS fluctuations, σ is the signal variance, and $\Phi(f)$ is the power spectral density. As shown in Figure 4.7, at all the bulk solid volume fractions, the overall amplitude of

the power spectra increases by increasing the particle Stokes number. Therefore, by increasing the particle Stokes number the magnitude of the RMS fluctuations increases.

The power spectra of the Delrin and steel particles have very similar slopes for all $\bar{C}$, but have different amplitudes, as can be seen in Figure 4.7. Comparison between the Delrin and glass spectra at low $\bar{C}$ (Figure 4.7.a) also shows similar decay slopes. In comparison, but the glass power spectrum has a higher amplitude. The nylon power spectra are similar to that of Delrin in amplitude, shape, and frequency range at low and medium $\bar{C}$. At $\bar{C} \approx 0.40$ the amplitude of low-frequency fluctuations is higher in the case of nylon than Delrin.

At high $\bar{C}$, both glass and nylon signals exhibit significantly different shapes in comparison with the Delrin power spectrum, namely the appearance of a -5/3 decay slope at the highest frequency range (Figures 4.4 (a) and 4.4(b)). Since this slope is just seen for the glass and nylon particles and they are the largest particles tested in this study with sizes almost twice the size of Delrin particles, this change in the shape of the power spectra could be related to the D/d ratio (bed diameter to particle size ratio). D/d is basically an indication of the effect of the presence of the wall on the flow behaviour of a solid liquid system in a vessel. Therefore, if the change of shape of the power spectra for glass and nylon is related to D/d, similar shapes might be seen at the wall zone for smaller particles as well. To further study this role (D/d), we looked at the power spectra at the wall zone for all particles. Figure 4.8 shows five different power spectra all at high $\bar{C}$. For steel particles at $\bar{C}$=0.52, only few data points exceeded the noise level which were not sufficient to analyze the slope of decay. Therefore, in addition to the signal at $\bar{C}$=0.52, the power spectra at $\bar{C}$=0.48 is also shown. At the wall region, the shape and amplitude of the Delrin power spectrum gets close to that of nylon and glass. It can be postulated that the shape of the power spectra at high $\bar{C}$ is related to the D/d ratio. While this phenomenon is limited to the wall region for small particles, it is extended to the core zone for the large particles.

Results of this section showed that in addition to the particle Stokes number, as the solid volume fraction reaches the values close to the maximum packing concentration (C_{max}), particle size relative to the vessel size plays an important role in defining power spectral shape and slope (Figure 4.7(d)).

4.3.4. Transition between decay slopes

As mentioned in Section 3.2, all the power spectra shown in Figures 4.4 (a), 4.4 (b) and, 4.4 (c), at $\bar{C} \leq 0.4$, exhibited a larger slope of decay than -3 (i.e. $\alpha > -3$) at the lower frequency ranges, i.e. prior to the -3 slope of the decay. In order to assess the slope of this region more accurately, measurements with lower sampling rate were conducted. This method provided more data points in the lower frequency range. Figure 4.9 shows a sample comparison of the power spectra of the measurements with the two different sampling rates, verifying that the curves overlap as expected.

The decay slopes of the power spectra in the low-frequency region are measured and shown in Figures 4.10 and 4.11 for glass and steel, respectively. For both particles, the power spectra exhibit a -5/3 slope prior to the -3. The extent of this slope decreases as $\bar{C}$ increases. And for $\bar{C} >$ 0.41, -5/3 slope disappears, and -3 slope takes over the whole frequency domain. We have previously referred to the frequency at which the -3 slope region begins as the transition frequency (f_t) (Marefatallah et al., 2019b). Figures 4.4, 4.10 and 4.11 show that similar to the Delrin particles in our previous work (Marefatallah et al., 2019b), f_t decreases by increasing $\bar{C}$.

A -5/3 decay slope prior to the -3 slope suggests a turbulent flow coupled with an external force which acts at a narrow frequency range ($\sim f_t$) (Kraichnan, 1967; Lilly, 1969). We showed in a previous study that in the case of solid–liquid fluidized bed this external force is most probably associated with the void fraction waves (Marefatallah et al., 2019b). From the experimental work done by Ham et al. (1990) it is understood that the dominant frequency of the instability waves in a fluidization system increases monotonically with the Froude number, which is defined as:

$$\mathrm{Fr} = \frac{{u_s}^2}{gd} \tag{4.5}$$

where u_s is the superficial velocity, d is particle size and g is the acceleration due to gravity. Here, we plotted the transition frequency of each particle at bulk solid fraction showed in Figure 4.4.a, 4.b, and 4.5 vs their Froude numbers, shown in Figure 4.12. Please note that the values for f_t are estimated visually here. It can be seen in this figure that by increasing the Froude number the transition frequency increases for nylon and glass, and to a certain extent for steel. These results

are consistent with our findings for the Delrin particles (Marefatallah et al., 2019b). The relationship between the Froude number and f_t confirms the hypothesis that the external force that acts on the turbulent flow and makes the power spectra resemble a 2D turbulent is related to the void fraction waves in the bed. This can also be applied to the case of steel particles since overall there is an increase in the transition frequency at low Froude numbers. However, the transition frequency does not change significantly at higher Froude numbers.

The fact that by increasing $\bar{C}$ (decreasing Froude number) f_t decreases indicates that the dominant frequency of the vertically travelling instability waves is a function of $\bar{C}$ which is consistent with the findings of previous studies (El-Kaissy and Homsy, 1976; Gibilaro et al., 1990; Ham et al., 1990).

4.3.5. Comparison of high-frequency fluctuations to existing models

All the power spectra presented in this study show that the highest amplitude occurs at the lowest frequency ranges. The time signals (Figure 4.6.a) also demonstrate the existence of low-frequency, high-amplitude fluctuations that become more dominant as $\bar{C}$ gets closer to the value of C_{max}.

Existing models such as Buyevich and Kapbasov's modified model (1994) are developed based on the consideration of small-scale fluctuations only. Therefore, to obtain a better comparison between the measurements of this study with this model, we applied a high-pass filter to the power spectra. The cut-off frequency was set to 1 Hz. This cut-off was chosen since in the most cases the power density spectra start to decay at around 1 Hz (Zenit and Hunt, 2000). Therefore, by excluding components of the spectra with frequencies lower than 1 Hz, almost all the fluctuations with the highest amplitude (large-scale fluctuations) are eliminated from the time signal. The time signals before and after the high-pass filter are shown in Figures 4.6.a and 4.6.b, respectively. Time signals at higher $\bar{C}$ are more affected by the filter.

For comparison with the predicted values of Buyevich and Kapbasov (1994), the Root Mean Square (RMS) of the fluctuations are averaged over all 316 pixels of the cross-section and averaged values are shown in Figures 4.13 and 4.14. In addition to the modified model by

Buyevich and Kapbasov, the initial model developed by (Buyevich, 1971) is also illustrated. The initial model by Buyevich (Buyevich, 1971) was developed based on the statistical positioning of the mono-sized spherical particles, while the other model (Buyevich and Kapbasov, 1994) is based on the thermodynamic theory of fluctuations. The initial model has previously been found to have a better prediction of the magnitude of the fluctuations in inhomogeneous systems (Buyevich and Kapbasov, 1999). For low-Stokes particles (Delrin and nylon), the filtered-RMS vs. $\bar{C}$ profile becomes more similar to the trend predicted by the model. The filtered data has its maximum RMS value at $\bar{C} \approx 0.3$, as also predicted by the model. The maximum at $\bar{C} = 0.3$ was also observed by Zenit and Hunt (Zenit and Hunt, 2000). However, the difference between the measured experimental values and the model's predictions increases after filtering. For the medium-Stokes particles (glass), the initial Buyevich model has a better prediction of the trend of the measured values (Marefatallah et al., 2019a). However, the trend of the filtered data is more similar to the prediction of the modified model, especially at higher $\bar{C}$. The trend of variations of RMS fluctuations for low and medium Stokes particles are more similar to the prediction of the Buyevich and Kapbasov's model (Buyevich and Kapbasov, 1994). This was expected because this model only considers the small-scale fluctuations. The significant difference between the original measurements and filtered data at the high solid fractions, especially at $\bar{C} \geq 0.45$, indicates that the large-scale fluctuations are dominant at this region. This is consistent with the findings of Zenit and Hunt (2000) that the local maximum in their results at $\bar{C}$ = 0.45 disappeared after filtering. This finding also confirms the existence of a wavy fluidization regime, introduced by Didwania and Homsy (1981) at the highest $\bar{C}$ ranges, just below C_{max}. This wavy fluidization regime was described as a fluidization state dominated by low-frequency high amplitude instability void fraction waves traveling in the bed (Didwania and Homsy, 1981; Zenit and Hunt, 2000).

For the high-stokes particles (steel), the high-pass filter does not significantly change the trend of the RMS vs. $\bar{C}$ profile. For both filtered and original data, the initial Buyevich model has a better prediction. The initial Buyevich model performed better for the inhomogeneous systems (Buyevich and Kapbasov, 1999) while the modified model had the assumption of the flow being homogenous. This could be indicating that steel fluidized bed is the most inhomogeneous among

the particles tested. Even after filtering the low-frequency, high-amplitude fluctuations, the flow still behaves as an inhomogeneous system and the trend of changes in the RMS fluctuations does not change after high-pass filtering. Furthermore, results of Figure 4.14 show that eliminating low-frequency fluctuations does not significantly change the magnitude of the fluctuations, especially at $\bar{C} \leq 0.45$ for steel particles.

4.4. Conclusions

In this study, we analyzed the local solid fraction fluctuations of particles with a wide range of Stokes numbers in the time- and frequency-domains. The results showed that the amplitude of the power spectra were higher in the wall region compared to the center of the bed for all frequencies. The shape and slopes of the power spectra did not change significantly by changing the radial position in the bed cross-section. At the wall region, the overall amplitude of the power spectra increased significantly (especially at high frequency ranges bellow the noise frequency), which was an indication of the presence of particle–wall interactions in that region. For all the particles tested here, over a wide range of $\bar{C}$, the power spectra always exhibited a -3 decay slope for a large portion of the frequency range, predominantly at higher frequencies. Results obtained at lower sampling rates confirmed the existence of a -5/3 slope prior to the -3 slope at $\bar{C} \leq 0.4$. This combination of slopes is an indication of a turbulent flow coupled with an external force, which drives one of the flow's degrees of freedom, leading to a more 2D-like turbulent spectrum. For the case of a liquid fluidization system, this external force is most probably the instability void fraction waves moving along the bed height. Results of this study confirmed that the dominant frequency of the external force decreases by increasing $\bar{C}$, a result that we already showed for one particle type (Marefatallah et al., 2019b) to be consistent with the fluctuations originating from void fraction instability waves in the bed.

A high-pass filter was applied to the original time signals to eliminate the fluctuations frequencies lower than 1 Hz. The comparison between the filtered RMS fluctuations and two existing models showed that for low- and medium-Stokes particles, the trend of the changes in RMS by $\bar{C}$ is well predicted by the Buyevich and Kapbasov model (Buyevich and Kapbasov, 1994). However, the

magnitude of the fluctuations is overpredicted by the model which was also shown in the past studies (Marefatallah et al., 2019a, 2019c; Zenit and Hunt, 2000). For high-Stokes particle, the trend did not change significantly after the filtering, except at the highest bulk concentrations.

The combination of the effect of filtering and power spectrum analysis suggests that by increasing bulk solid fraction, the fluidization flow behaves more like a two-dimensional flow, i.e. wavy flow regimes with the dominant low-frequency void fraction waves traveling in the bed. Although the -3 slope (associated with 2D turbulent flow) was observed for low bulk solid fractions, it seems that at this solid fraction range the external force is at a high enough frequency to not be immediately apparent. The void fraction waves appearing at this region have lower frequencies compared to the low -and medium-solid fraction systems, but higher amplitude.

Overall, the local time and frequency domain analysis of the solid fraction fluctuations improved our knowledge about the nature of small- and large-scale fluctuations and different regimes (wavy vs turbulent) in the bed. These results, along with the local measurements presented in previous studies, can be used to validate and improve computational models that aim to predict the flow behaviour and particle distribution in the bed cross-section. Improvement in the computational modeling of solid–liquid fluidization system will enhance the modeling of multiphase flows in general.

4.5. Figures

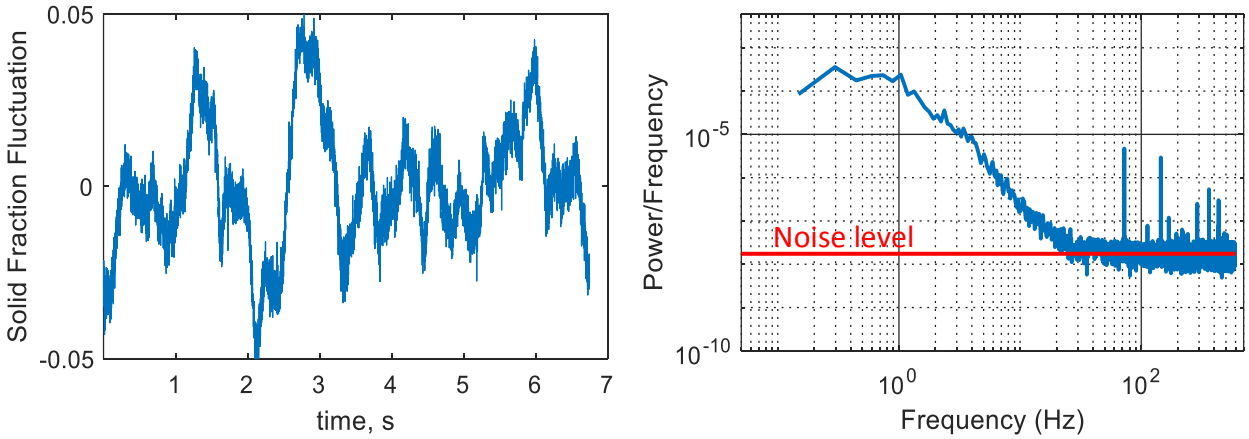

Figure 4.1. Solid fraction fluctuations and solid fraction power spectra for glass particles at $\overline{C}$ =0.31, r/R=0.55, f_s=1186 fps.

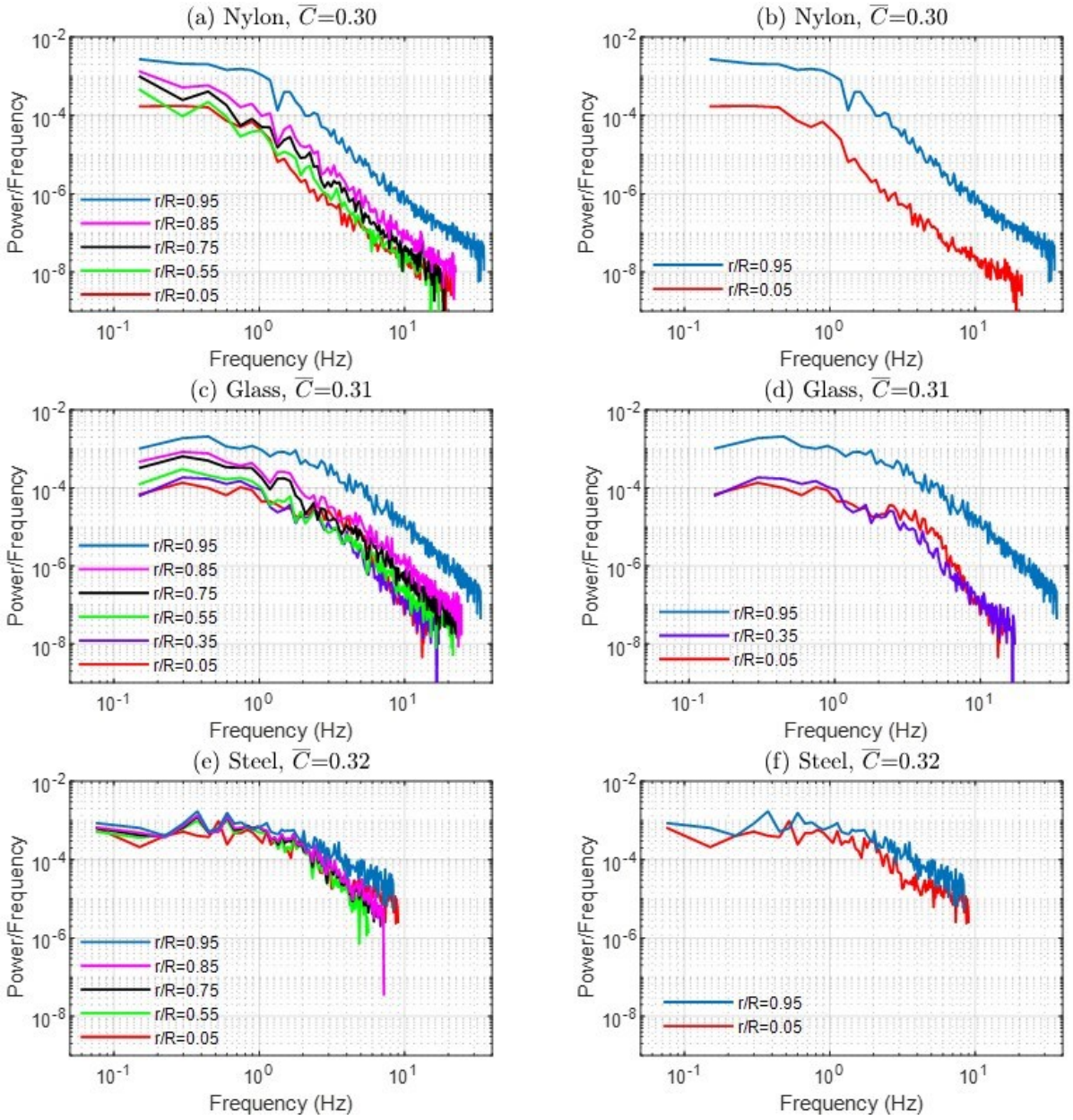

Figure 4.2. Solid fraction power spectra at different radial positions, f_s=1186 fps for nylon and glass and f_s=600 fps for steel.

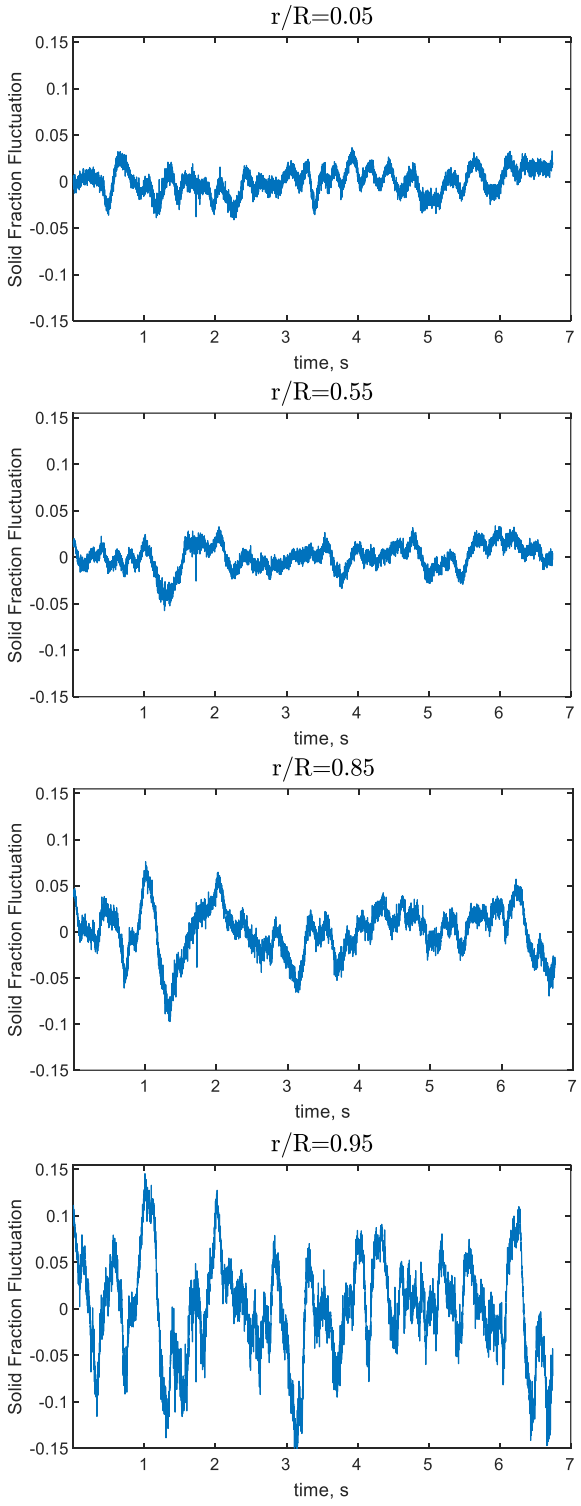

Figure 4.3. Solid fraction fluctuations at different radial positions for glass particles at $\bar{C}$=0.31, f_s=1186 fps

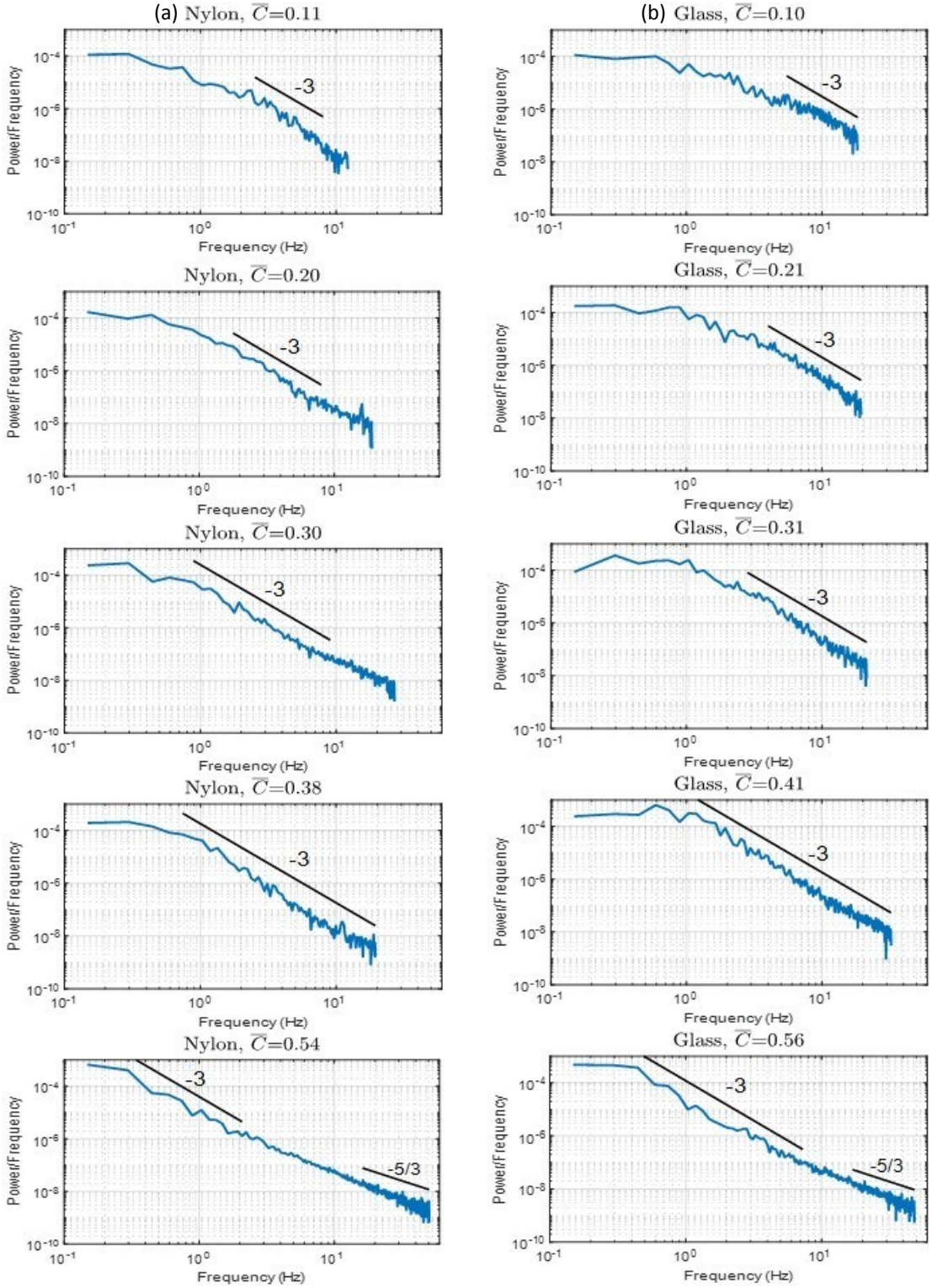

Figure 4.4.a and 4.4.b. Solid fraction power spectra at different bulk solid fractions and at r/R=0.55., f_s=1186 fps: a) nylon (left), b) glass (right)

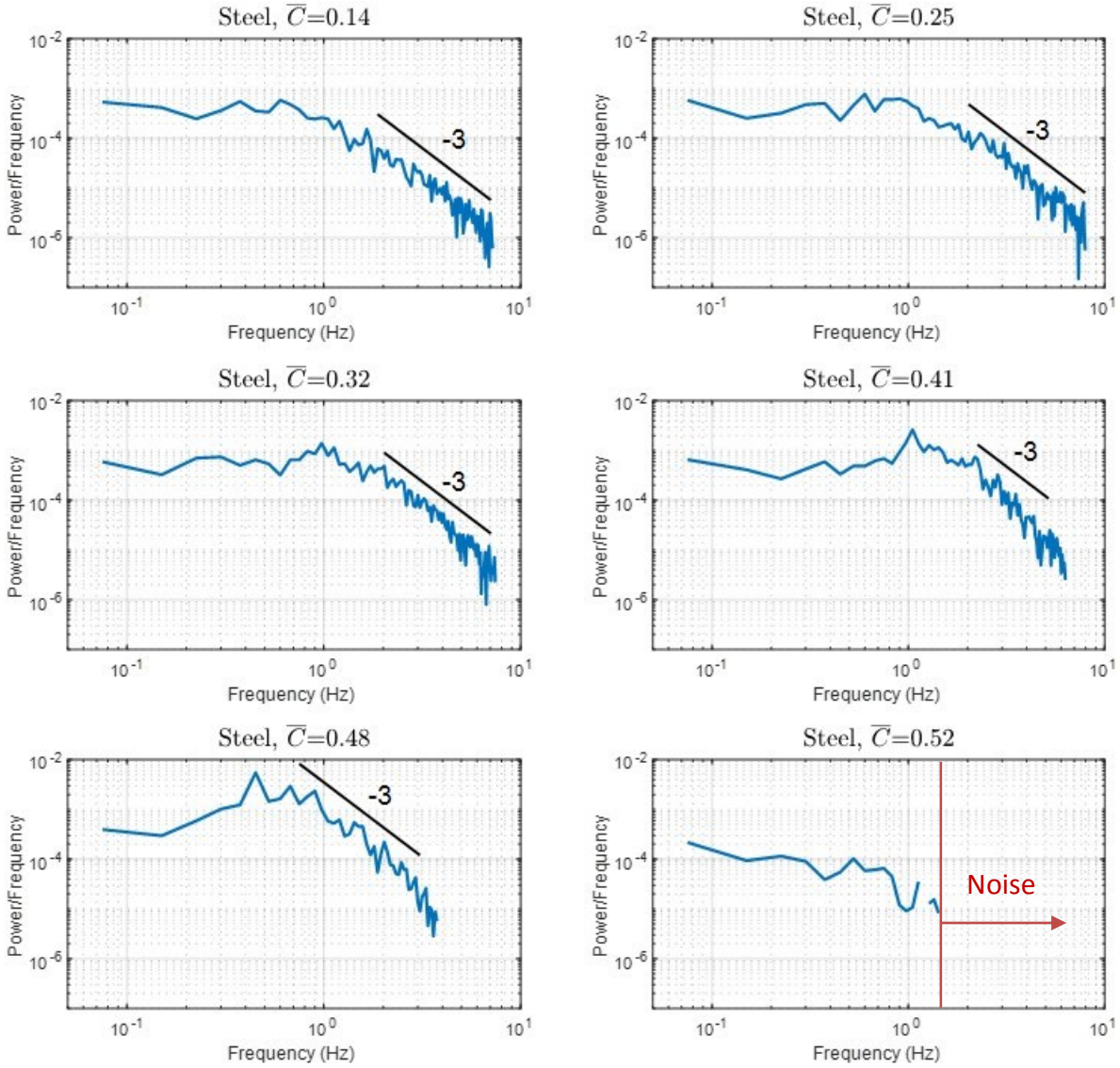

Figure 4.5. Solid fraction power spectra at different bulk solid fractions for steel particles, f_s=600 fps, r/R=0.55.

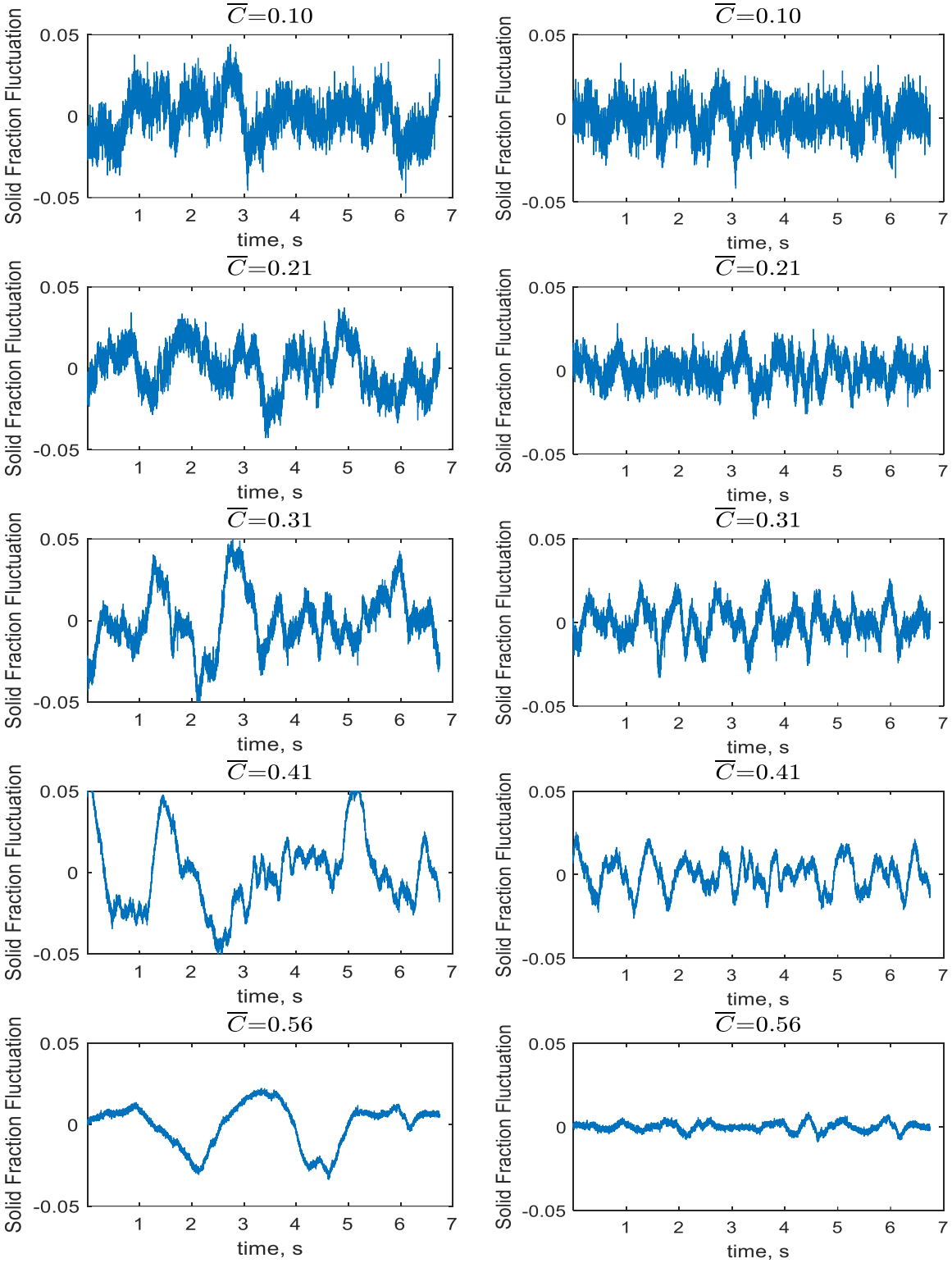

Figure 4.6.a and 4.6.b. Solid fraction fluctuations at different bulk solid fractions for glass particles at r/R=0.55: a) original fluctuation signal (left), b) resulting signal after high-pass filtering (cut-off frequency of 1 Hz) (right)

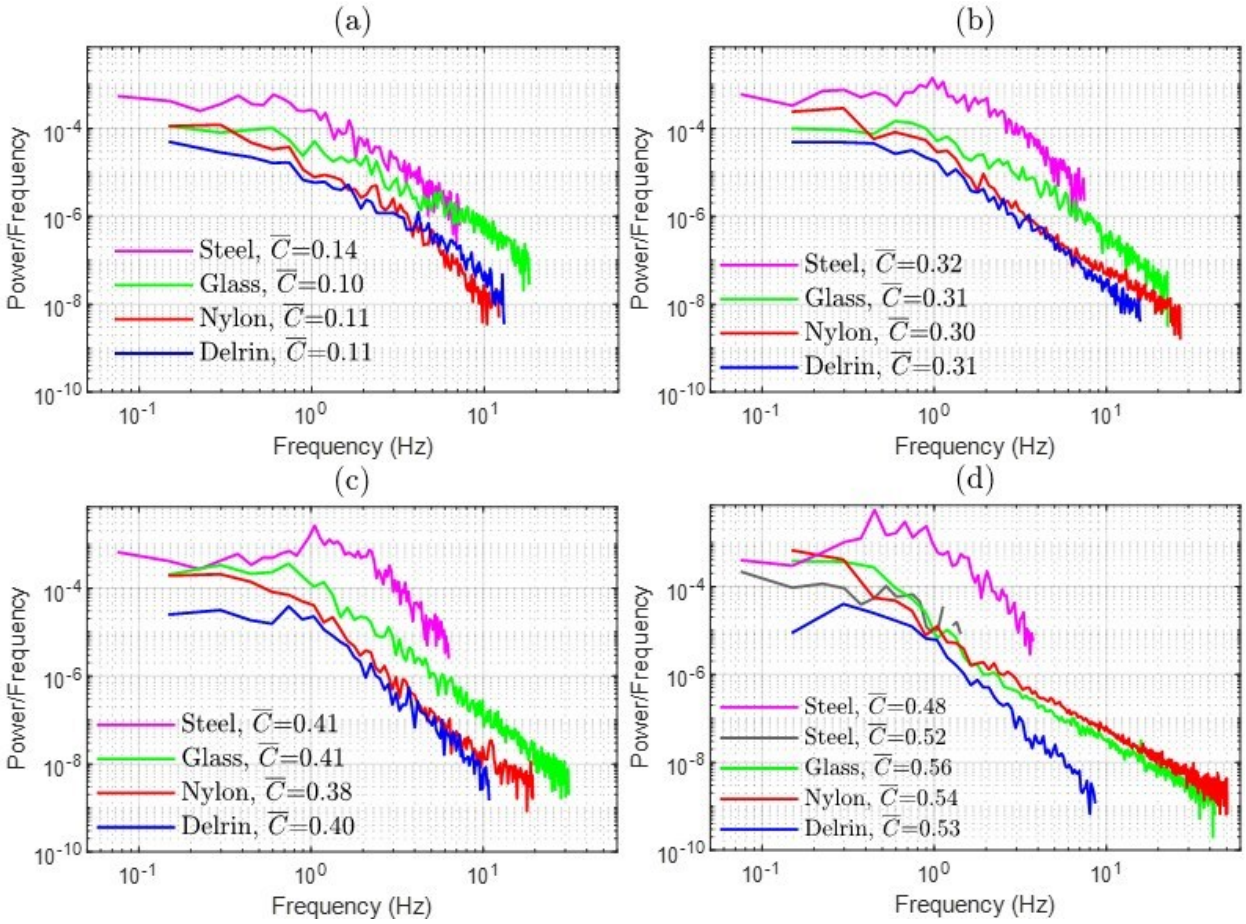

Figure 4.7. Solid fraction power spectra at different bulk solid fractions at r/R=0.55 for steel (St=3809, f_s=600 fps), glass (St=882, f_s=1186 fps), nylon (St=122, f_s=1186 fps), and Delrin (St=94, f_s=1186 fps).

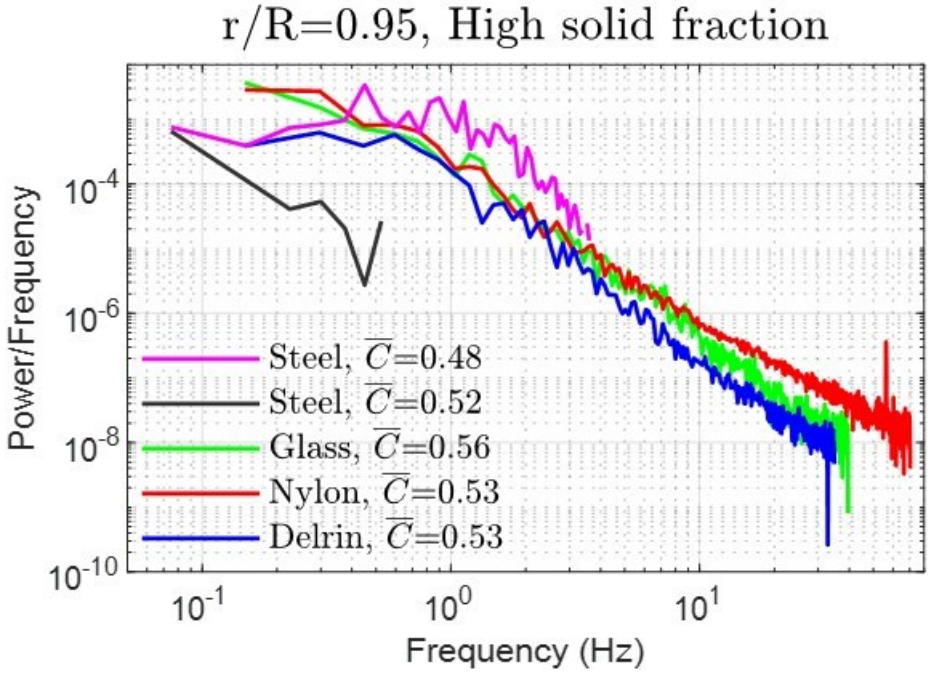

Figure 4.8. Solid fraction power spectra at the near the wall region for steel (St=3809, f_s=600 fps), glass (St=882, f_s=1186 fps), nylon (St=122, f_s=1186 fps), and Delrin (St=94, f_s=1186 fps).

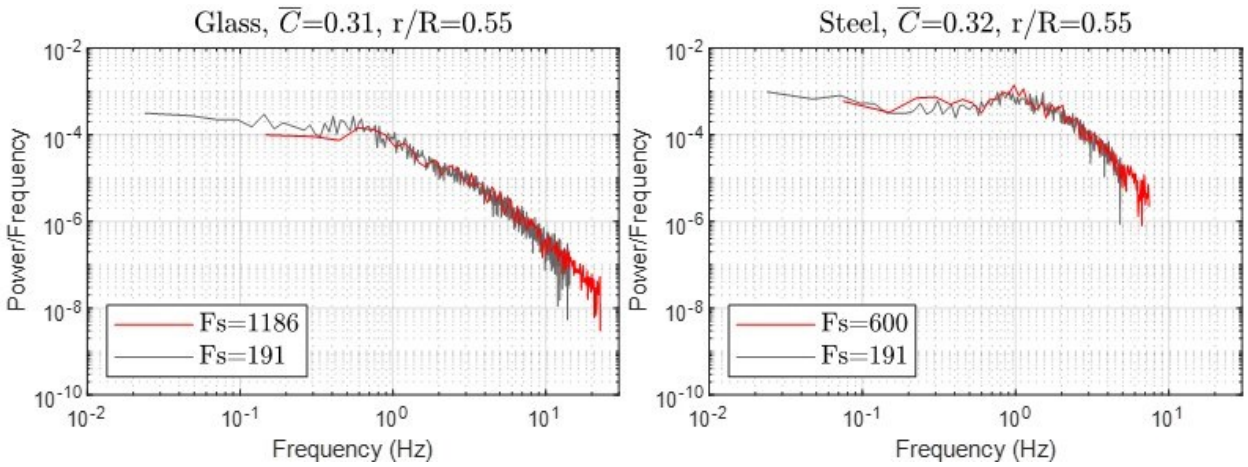

Figure 4.9. Solid fraction power spectra obtained at different sampling rates (f_s) for glass and steel particles

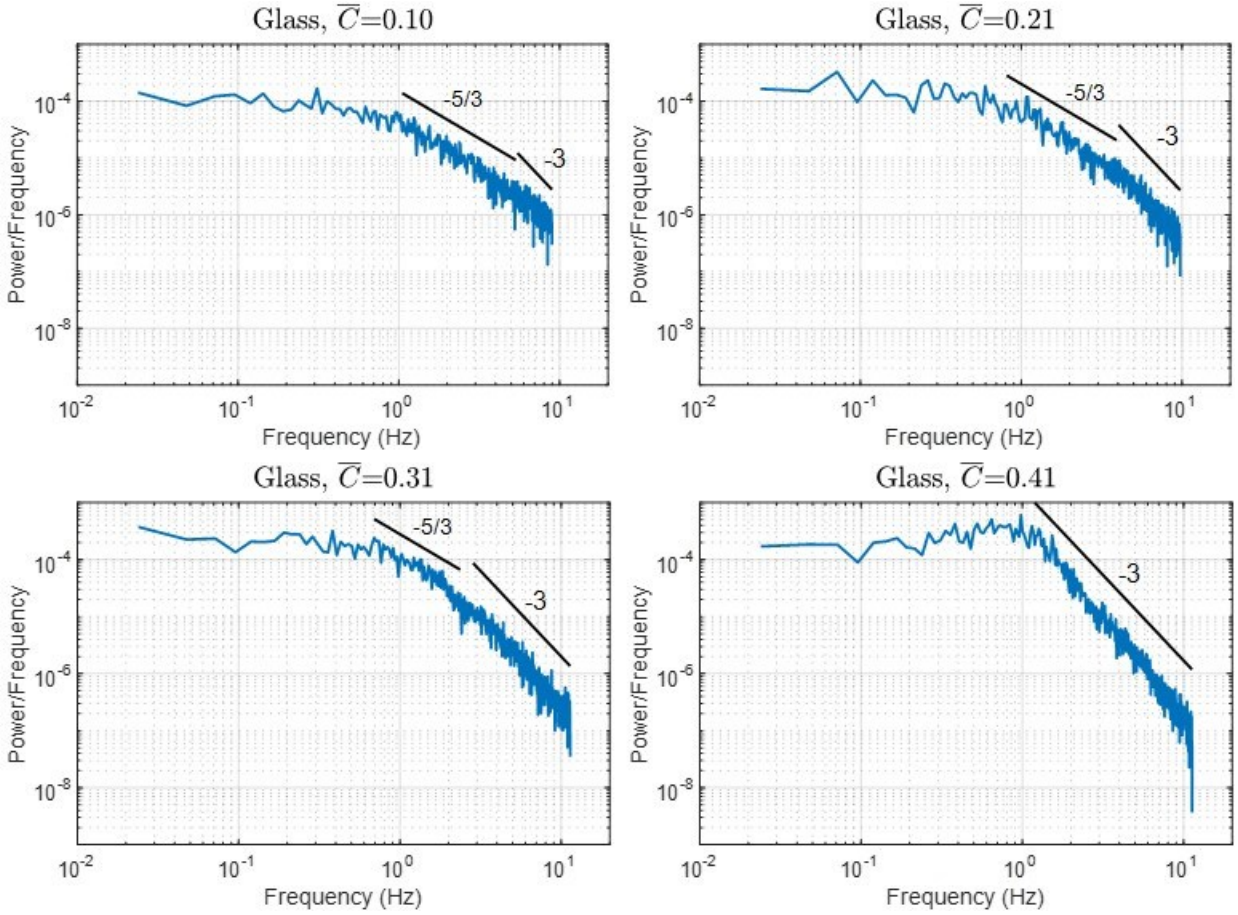

Figure 4.10. Solid fraction power spectra at different bulk solid fractions for glass particles, obtained at f_s=191 fps, r/R=0.55.

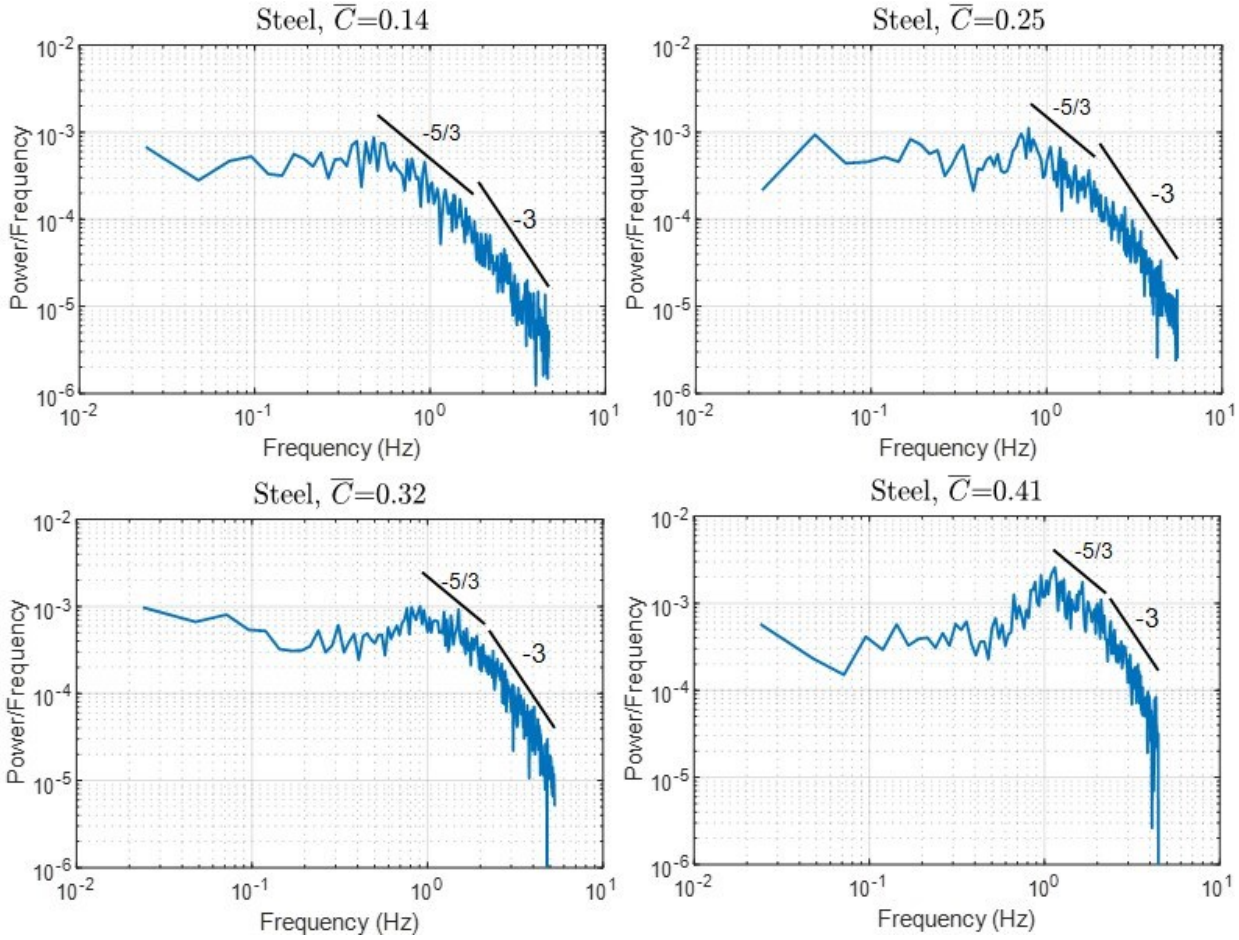

Figure 4.11. Solid fraction power spectra at different bulk solid fractions for steel particles, obtained at f_s=191 fps, r/R=0.55.

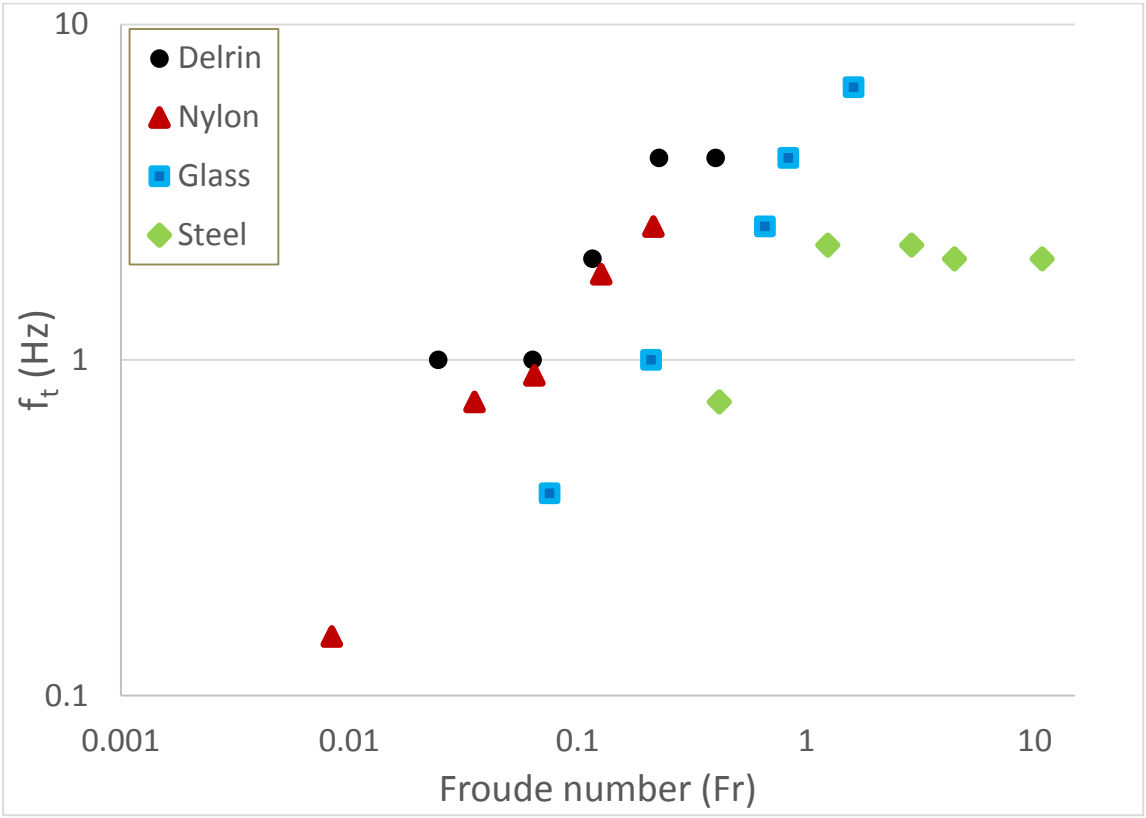

Figure 4. 12. Transition frequency (f_t) vs Froude number (Fr) for four different particle types and at different bulk solid fractions shown in Figures 4.4(a), 4.4 (b) and 4.5. Delrin data point are from (Marefatallah et al, 2019b)

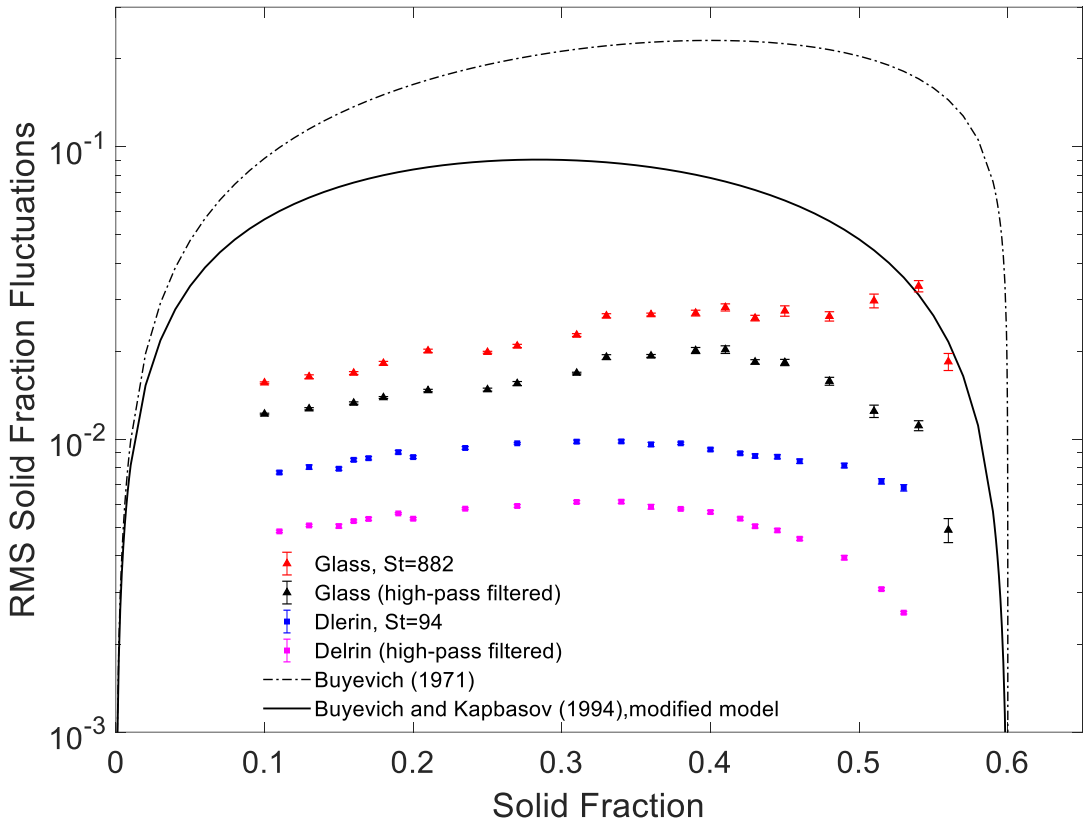

Figure 4.13. Cross-sectional averaged RMS solid fraction fluctuations before and after high-pass filtering in comparison to Buyevich and Kapbasov (1994) modified model and Buyevich (1971) model. Error bars shown in this figure illustrate standard errors. For each data point the error bars are calculated from 10 trials. Delrin experimental data is from (Marefatallah et al., 2019b), f_s=1186 fps.

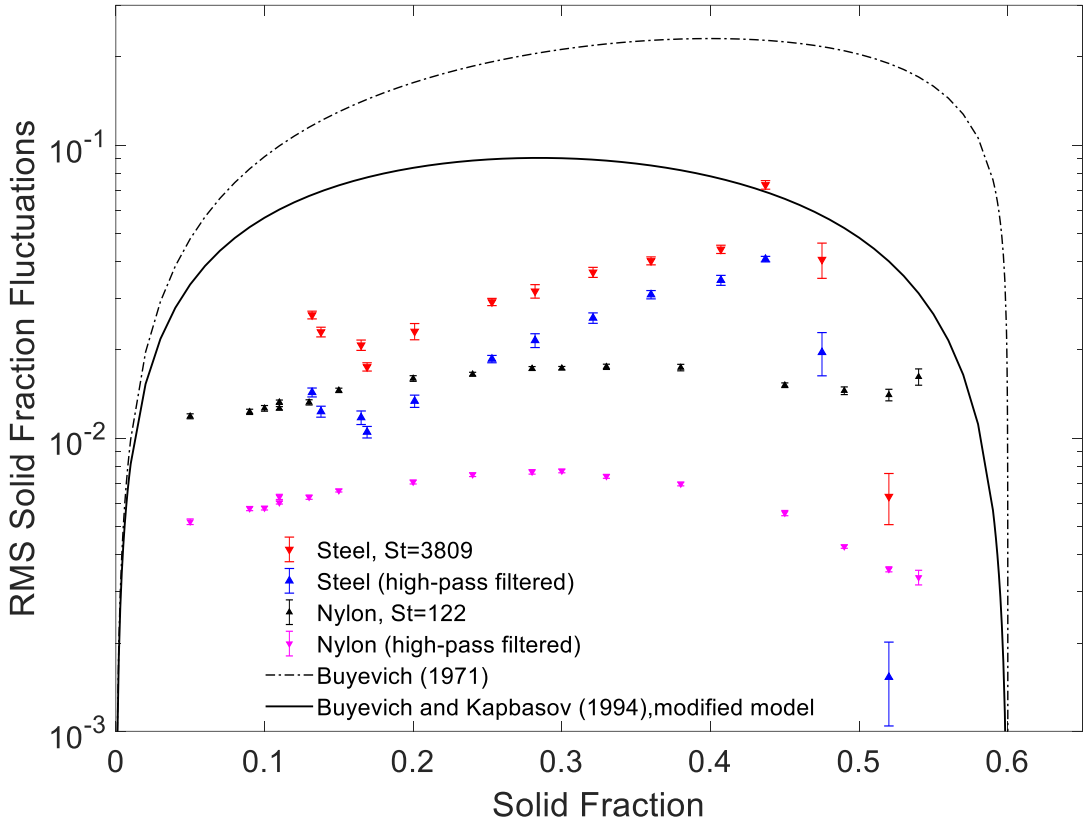

Figure 4.14. Cross-sectional averaged RMS solid fraction fluctuations before and after high-pass filtering in comparison to Buyevich and Kapbasov (1994) modified model and Buyevich (1971) model. Error bars shown in this figure illustrate standard errors. For each data point the error bars are calculated from 10 trials. f_s=1186 fps for nylon and f_s=600 fps for steel.

4.6. References

Buyevich, Yu.A. (1971). On the fluctuations of concentration in disperse systems The random number of particles in a fixed volume. Chem. Eng. Sci. *26*, 1195–1201.

Buyevich, Y.A., and Kapbasov, S.K. (1999). Particulate Pressure in Disperse Flow. Int. J. Fluid Mech. Res. *26*, 72–97.

Buyevich, Yu.A., and Kapbasov, Sh.K. (1994). Random fluctuations in a fluidized bed. Chem. Eng. Sci. *49*, 1229–1243.

Cook, M.V. (2012). Flight Dynamics Principles: A Linear Systems Approach to Aircraft Stability and Control (Butterworth-Heinemann).

Cornelissen, J.T., Taghipour, F., Escudié, R., Ellis, N., and Grace, J.R. (2007). CFD modelling of a liquid–solid fluidized bed. Chem. Eng. Sci. *62*, 6334–6348.

Didwania, A.K., and Homsy, G.M. (1981). Flow regimes and flow transitions in liquid fluidized beds. Int. J. Multiph. Flow *7*, 563–580.

Dyakowski, T., Jeanmeure, L.F.C., and Jaworski, A.J. (2000). Applications of electrical tomography for gas–solids and liquid–solids flows — a review. Powder Technol. *112*, 174–192.

El-Kaissy, M.M., and Homsy, G.M. (1976). Instability waves and the origin of bubbles in fluidized beds: Part 1: Experiments. Int. J. Multiph. Flow *2*, 379–395.

Epstein, N. (2002). Applications of Liquid-Solid Fluidization. Int. J. Chem. React. Eng. 1, 1-16

Fischer, A., König, J., and Czarske, J. (2008). Speckle noise influence on measuring turbulence spectra using time-resolved Doppler global velocimetry with laser frequency modulation. Meas. Sci. Technol. *19*, 125402.

Gevrin, F., Masbernat, O., and Simonin, O. (2010). Numerical study of solid–liquid fluidization dynamics. AIChE J. *56*, 2781–2794.

Gibilaro, L., Foscolo, P., and Felice, R.D. (1990). The Velocity of Dynamic Waves in Fluidised Beds. In Two Phase Flows and Waves, (Springer, New York, NY), pp. 56–69.

Ham, J.M., Thomas, S., Guazzelli, E., Homsy, G.M., and Anselmet, M.-C. (1990). An experimental study of the stability of liquid-fluidized beds. Int. J. Multiph. Flow *16*, 171–185.

Kraichnan, R.H. (1967). Inertial Ranges in Two-Dimensional Turbulence. Phys. Fluids *10*, 1417–1423.

Lilly, D.K. (1969). Numerical Simulation of Two-Dimensional Turbulence. Phys. Fluids *12*, II–240.

Marefatallah, M., Breakey, D., and Sanders, R.S. (2019a). Experimental Study of Local Solid Volume Fraction Fluctuations in a Liquid Fluidized Bed: Particles with a wide range of Stokes numbers. *in preparation for submission*.

Marefatallah, M., Breakey, D., and Sanders, R.S. (2019b). Study of local solid volume fraction fluctuations using high speed electrical impedance tomography: Particles with low Stokes number. Chem. Eng. Sci. *203*, 439–449.

Panneerselvam, R., Savithri, S., and Surender, G.D. (2007). CFD based investigations on hydrodynamics and energy dissipation due to solid motion in liquid fluidised bed. Chem. Eng. J. *132*, 159–171.

Zenit, R., and Hunt, M.L. (2000). Solid fraction fluctuations in solid–liquid flows. Int. J. Multiph. Flow *26*, 763–781.

Zhang, K., Wu, G., Brandani, S., Chen, H., and Yang, Y. (2012). CFD simulation of dynamic characteristics in liquid–solid fluidized beds. Powder Technol. *227*, 104–110.

Chapter 5. Conclusions and Recommendations

5.1. Summary of contributions

This project focused on providing new understanding of the local dynamics of solid–liquid fluidization systems. The main goal was to provide local measurements of the solid fraction fluctuations in a liquid fluidized bed. The measurements were conducted with different particles to study a wide range of Stokes numbers, bulk solid volume fractions and fluidization velocities. These results are a valuable addition to the literature and can be used to validate advanced simulations of fluidized beds. Additionally, the results obtained here enhanced the understanding of the important interactions in a solid–liquid multiphase system: i.e. particle–particle, particle–fluid, and particle–wall interactions. The effect of these interactions on the magnitude of the fluctuations and the relative importance of each at different conditions were considered.

Using a recently introduced measurement technique, instantaneous local solid fractions were measured in a liquid fluidized bed. Electrical impedance tomography (EIT) made it possible to measure the instantaneous solid fraction at sampling frequencies up to 1186 frames per second. The important advantage of this technique over other measurement methods such as optical techniques (Yamazaki et al., 1992) is that it provide results even at the high solid volume fractions, e.g. values close to the maximum packing concentration. Additionally, compared to optical techniques, EIT is not limited by mixture transparency and can also operate on opaque systems.

Previous studies showed that the magnitude of the cross-sectional averaged RMS fluctuations in a liquid fluidized bed change substantially with increasing particle Stokes number (Zenit and Hunt, 2000). A preliminary study of the local RMS fluctuations revealed that the distribution of the fluctuations is not uniform over the bed cross-section (Hashemi, 2013). Based on these previous studies, this focused on the investigation of the effect of particle Stokes number on the local RMS fluctuations of different particles in a liquid fluidized bed. For this purpose, four particle types were studied: Delrin, nylon, glass, and steel. These particles and their sizes were chosen so that the results would cover a wide range of particle Stokes numbers ($94 \leq \mathrm{St_t} \leq 3809$)[1]. Results

[1] The Stokes number definition used here is that used by other researchers who studied solid concentration fluctuations in liquid fluidized beds (e.g. Zenit and Hunt, 2000): $\mathrm{St_t} = \frac{\rho_s}{\rho_f}\frac{\mathrm{Re_t}}{9}$, where $\mathrm{Re_t}$ is the particle Reynolds number at its terminal settling velocity. As described in Ch. 1, this may not be the "correct" or most physically meaningful definition of St.

showed that for all particles tested the RMS fluctuations were not uniformly distributed along the bed cross-section. The highest values of the fluctuations were observed in the near-wall region. The values of the RMS fluctuations in this region were found to be 1.2–4 times higher than those at the bed center. This finding emphasizes the importance of local measurements of the solid fraction fluctuations in comparison with the existing cross-sectional averaged values previously available in the literature.

Analysis of the effect of particle Stokes number on the magnitude of the fluctuations showed that at any given radial position, the local RMS fluctuations were higher for particles with higher Stokes numbers. Therefore, Zenit and Hunt's (2000) observation of an increase in the cross-sectional averaged RMS values occurs throughout the whole cross-section of the bed was found in the present study as well. Furthermore, trends of spatial variations of the local RMS profiles did not change very much with Stokes number, just the overall level of the magnitude of the fluctuations.

Based on the local measurements of this study, it was proposed that the characterization of the local RMS fluctuations can be grouped or classified over two main zones of the bed cross-section: the core zone and the wall zone. This was because the RMS fluctuation profile shapes did not vary significantly with the parameters; only the magnitudes changed. The wall zone was identified as the narrow strip close to the wall where the maximum RMS fluctuations occur. The core zone ($r/R \leq 0.45$) is located at the center of the bed, where the minimum RMS fluctuations occur, and the magnitude of the fluctuations is almost constant over this zone of the bed.

The values of the RMS fluctuations measured in each zone suggested the following relationship:

$$\frac{\text{RMS fluctuations}_{\text{wall}}}{\text{RMS fluctuations}_{\text{cross-section}}} = \frac{\text{RMS fluctuations}_{\text{cross-section}}}{\text{RMS fluctuations}_{\text{core}}}$$

This relationship shows that for the modeling of these three values, prediction or measurements of any two parameters will be sufficient to calculate the third one. This relationship along with the proposal of measurement/modeling of core- and wall-zone simplifies the modeling of local

RMS fluctuations in fluidized beds by introducing a simplified relationship between local fluctuations and radial position.

The comparison between the local RMS fluctuations of this study and the cross-sectional averaged values reported by Zenit and Hunt showed an acceptable agreement (Zenit and Hunt, 2000). However, for all the particles tested, at any given bulk solid fraction the RMS fluctuations at the wall zone were found to be closest to the values reported by Zenit and Hunt (2000). This could be due to their measurement technique being biased by the near-wall region.

In addition to the above-mentioned analysis, the results were used to test existing models that aim to predict the magnitude of the fluctuations in a fluidized bed. Four different models were examined. Each of these models produced a relatively good prediction for certain conditions. The Buyevich (1971) had a better prediction of the trend of the changes in the RMS fluctuations for medium and high Stokes particles ($882 \leq \mathrm{St_t} \leq 3809$). Buyevich and Kapbasov (1994) better predicted this trend for low-Stokes particles ($94 \leq \mathrm{St_t} \leq 122$). However, both of these models overpredicted the values of the RMS fluctuations. The semi-empirical model proposed by Gevrin et al. (2010) performed well for the low-Stokes particles in the lower range of bulk solid fraction. However, this model requires a scaling factor for each particle type. Since the scaling factors increased with increasing particle Stokes number, the results of this study suggested that there is a possible relationship between this scaling factor and the particle properties. More studies will be required to examine this relationship.

Furthermore, to study the nature of small- and large- scale fluctuations the local solid fraction fluctuations were analyzed in both time- and frequency-domains. The power spectra showed that the slope of the decay did not change significantly with changing radial position. However, the amplitude of the power spectra increased in the wall zone. Although the magnitude of the power spectra increased over the whole frequency domain, the increase was significantly greater in the higher frequency ranges. Since higher frequency ranges were more affected by changing the radial position, and all parameters are constant (i.e. the fluidization conditions, and the particle and fluid properties) except the existence of the wall at this zone. It can be tentively concluded

that this change in the amplitude of the power spectra is an indication of the particle–wall collisions occurring in the wall zone.

For all the particles tested in this thesis project, at any bulk solid fraction, the power spectra always exhibited a -3 slope of decay. The extent of this slope changed with the bulk solid fraction. By increasing the bulk solid fraction, the -3 slope moved towards lower frequency ranges and covered the whole frequency domain at the highest bulk solid fractions. Additional measurements conducted at a lower sampling frequency confirmed the existence of a -5/3 slope prior to the -3 slope, especially at low and medium bulk solid fractions ($0.1 \leq \overline{C} \leq 0.4$). A -5/3 slope prior to a -3 slope was interpreted as an indication of three-dimensional turbulent flow coupled with an external force which resulted in a power spectrum resembling a 2D turbulent flow. This external force may be related to the vertical movement of the instability void fraction waves in the fluidized bed. Based on the results obtained in this study, the dominant frequency of the external force decreased with increasing bulk solid fraction. The dominant frequency of the external force is referred to as the 'transition frequency' in this work, since it indicated the frequency at which the -5/3 slope changed to -3 slope. The relationship between the transition frequency and Froude number showed that these parameters are related, i.e. increasing one would result in an increase in the other.

High-pass filtering of the original time signals revealed that the amplitude of the low-frequency high-amplitude fluctuations significantly increased with increasing bulk solid fraction. These fluctuations became dominant in the flow at bulk solid volume fractions greater than 0.4 where it appeared that the flow regime in the bed transitioned to a 2D wavy flow.

This thesis project provided local information on the fluctuating component of the solid fraction, unlike the previous studies which were limited to cross-sectional-averaged values. Therefore, the results presented in this thesis can be used to directly examine the predictions of CFD models of a liquid fluidized bed. Furthermore, different assumptions made for different modeling approaches can be validated using the local experimental data provided here. This will enhance the current simulation works of two-phase systems and thus multiphase flows in general.

5.2. Uncertainties and Challenges

The uncertainties and challenges associated with the experimental measurement and the data interpretation of this study include the following:

1. In the interpretation of the power spectra analysis the main assumption of this study is that the solid fraction fluctuations and the fluctuations of the liquid velocity are fully correlated (over the range of the experimental conditions and particle Stokes number tested here: $94 \leq \mathrm{St_t} \leq 3809$). The conditions at which this assumption is valid might depend on parameters such as particle Stokes number and fluidization conditions (Gevrin et al., 2010). The experimental study of Kechroud et al. (2010) showed that there is strong correlation between these two parameters in a liquid fluidized bed of glass particles in water ($150 \leq \mathrm{St_t} \leq 1600$). The experimental study by Hashemi (2013) confirmed also the idea of a strong connection between the two fluctuating components by comparison between his results of local solid fraction fluctuations for 2 mm and 4 mm glass beads ($150 \leq \mathrm{St_t} \leq 480$) with liquid velocity fluctuations measurements made by Kechroud et al. (2010). Gevrin et al. (2010) also proposed a relationship between these two parameters based on the assumption that macroscopic relations, i.e. Richardson-Zaki equation, are still valid at the small scales in a fluidized bed ($130 \leq \mathrm{St_t} \leq 3700$). While these studies demonstrate a correlation between different fluctuating parameters in a liquid fluidization system, further study is required to determine the exact relationship (and its range of validity) between them.
2. The proposed idea of resemblance of a 2D turbulent flow coupled with an external force was discussed in Chapter 2 and 4. It should be noted that for the range of Stokes numbers and particle properties tested in this study, an increasing Stokes number increased the particle Reynolds number. Particle Reynolds number plays an important role in the dominance of different turbulent kinetic energies in the fluid phase (Fox, 2014). The kinetic energy of the fluid phase is a summation of two components: the turbulent kinetic energy induced by large-scale motions and the pseudo-turbulent kinetic energy induced by particle wakes (Ozel et al., 2017). At high particle Reynolds numbers the role of the

turbulence of the liquid phase (produced at large scale and dissipated at dissipative (Kolmogrov) scales) is more dominant compared to the conditions when the particle Reynolds number is low (Fox, 2014). At low particle Reynolds numbers the liquid-phase turbulence can be considered negligible compared to the small-scale fluid velocity fluctuations due to particle wakes (pseudo-turbulence) (Fox, 2014). The ratio of the turbulent kinetic energy to the pseudo-turbulence changes with the particle Reynolds number (and thus with the Stokes number in this study). Therefore, it is possible that a transition between hydrodynamics regimes in the fluidized bed could occur over the range of particle Stokes and Reynolds numbers studied here. The effect of particle Reynolds number on the magnitude of the local solid fraction fluctuations and the criteria at which the flow regime changes in the fluidized bed require further investigation. This could be accomplished by conducting more experimental measurements using different particle Reynolds numbers (preferably independent of particle Stokes number).

3. The nature of the turbulent flow in a pipe and in a liquid fluidized bed may not be exactly the same depending on the fluid and particle properties (turbulence vs pseudo-turbulence). Therefore, there are more factors that need to be considered in the translation of the knowledge of particle–fluid interactions from the fluidization system of coarse particles to a turbulent pipe flow.

5.3. Recommendations for future work

The experimental data of this study provides new information on local solid fluctuations in a liquid fluidized bed. There is still a long path ahead before it will be possible to fully model all the aspects of multiphase flow systems such as solid–liquid fluidization. In particular, better insight into particle–fluid interactions is required. Based on the findings of this project, future research directions could progress along two avenues: 1. experimental measurements of local solid fraction fluctuations at wider ranges of fluid and particle properties and system conditions; 2. modeling of local solid fraction fluctuations in a fluidized bed with the consideration of particle properties and large-scale fluctuations. Details of each of these directions are discussed below.

5.3.1. Future experimental studies

Based on the findings the current study, the next step should be to obtain more local experimental data to cover a wider range of D/d (bed diameter to particle diameter). This means designing experiments for different bed diameters. These experimental measurements will widen the range of Stokes numbers studied. Additionally, since the effect of large-scale fluctuations on the magnitude of the RMS fluctuations was found to be related to the D/d values, these experiments will enable us to better distinguish small- and large-scale fluctuations. The necessity of isolating large-scale fluctuations for modeling purposes can then also be investigated.

Another avenue of research to continue the work done here is to conduct experiments using fluids with different viscosities. Since almost all the experimental data available for this subject in the literature are for systems of different particle types in water, experiments conducted with other fluids can more specifically investigate the fluid viscosity term in the particle Stokes number along with the particle properties. Furthermore, particles with same Stokes number but different size and densities can also be investigated. These results would assist in isolating the particle Stokes number effect on the magnitude of the local fluctuations.

As discussed in the previous section, there is still a need to investigate the correlation between solid phase volume fraction fluctuations with that of the fluid phase velocity. This analysis can be initiated by local measurement of the liquid phase velocity fluctuations at different particle properties and fluidization condition. These types of measurements will be challenging, specifically for highly concentrated opaque systems such as the fluidized bed of different particles tested in the current study. Additionally, experimental measurements of different fluctuating components within the fluidized bed over a wide range of particle Reynolds number are also valuable. These results, especially if they can isolate the effects of Reynolds number and Stokes number, can enhance our knowledge of the hydrodynamic regimes in the bed. Furthermore, based on the outcome of these studies a criterion might be defined to distinguish the flow configurations at which the agitation induced by the particles (pseudo-turbulence) is dominant

versus the regimes at which the liquid phase turbulence is not negligible and should be considered in the modeling of theses solid–liquid systems.

5.3.2. Future modeling works on solid fraction fluctuations

On the modeling side, the relationship between the scaling factors in the Gevrin semi-empirical model (Gevrin et al., 2010) and particle properties needs more analysis, which can be done by conducting experiments with a wider variety of particles and fluids in the bed. These experiments need to specifically cover a lower range of the particle Stokes numbers since Gevrin et al. (2010) only had an acceptable prediction of the trend in this range.

The results of this project showed that there is still a need for a comprehensive model that can predict the values of the RMS fluctuations at high bulk solid fractions. By the accurate prediction of one of the important dynamic parameters in fluidized beds this model can contribute to different modeling approaches that are employed to predict flow behaviour in fluidization systems. Based on the results of the current study, this model should account for the particle properties that make up the particle Stokes number.

In order to predict the local values of the RMS fluctuations this model should consider the two main zones introduced in this study, i.e. the core zone and wall zone. It should be able to predict the values of the RMS fluctuations in each of these zones. Furthermore, to fully capture the dynamics of the liquid fluidized bed, this model should account for the large-scale (low-frequency, high-amplitude) fluctuations in addition to the small-scale fluctuations.

5.4. References

Buyevich, Yu.A. (1971). On the fluctuations of concentration in disperse systems The random number of particles in a fixed volume. Chem. Eng. Sci. *26*, 1195–1201.

Buyevich, Yu.A., and Kapbasov, Sh.K. (1994). Random fluctuations in a fluidized bed. Chem. Eng. Sci. *49*, 1229–1243.

Fox, R.O. (2014). On multiphase turbulence models for collisional fluid–particle flows. J. Fluid Mech. *742*, 368–424.

Gevrin, F., Masbernat, O., and Simonin, O. (2010). Numerical study of solid–liquid fluidization dynamics. AIChE J. *56*, 2781–2794.

Hashemi, S.A. (2013). Velocity and concentration fluctuations in concentrated solid-liquid flows. PhD thesis. University of Alberta.

Kechroud, N., Brahimi, M., and Djati, A. (2010). Characterization of dynamic behaviour of the continuous phase in liquid fluidized bed. Powder Technol. *200*, 149–157.

Ozel, A., Brändle de Motta, J.C., Abbas, M., Fede, P., Masbernat, O., Vincent, S., Estivalezes, J.-L., and Simonin, O. (2017). Particle resolved direct numerical simulation of a liquid–solid fluidized bed: Comparison with experimental data. Int. J. Multiph. Flow *89*, 228–240.

Yamazaki, H., Tojo, K., and Miyanami, K. (1992). Measurement of local solids concentration in a suspension by an optical method. Powder Technol. *70*, 93–96.

Zenit, R., and Hunt, M.L. (2000). Solid fraction fluctuations in solid–liquid flows. Int. J. Multiph. Flow *26*, 763–781.

Bibliography

Abbas, M., Climent, E., Parmentier, J.-F., and Simonin, O. (2010). Flow of particles suspended in a sheared viscous fluid: Effects of finite inertia and inelastic collisions. AIChE J. 56, 2523–2538.

Azzi, A., Azzopardi, B.J., Abdulkareem, N.H., Hilal, N., and Hunt, A. (2010). Study of fluidization using Electrical Capacitance Tomography. Proceedings of the 7th International Conference on Multiphase Flow ICMF 2010, (Florida, USA).

Azzopardi, B.J., Jackson, K., Robinson, J.P., Kaji, R., Byars, M., and Hunt, A. (2008). Fluctuations in dense phase pneumatic conveying of pulverised coal measured using electrical capacitance tomography. Chem. Eng. Sci. 63, 2548–2558.

Batchelor, G.K. (1988). A new theory of the instability of a uniform fluidized bed. J Fluid Mech 193, 1988, 75–110.

Bolton, G.T., Hooper, C.W., Mann, R., and Stitt, E.H. (2004). Flow distribution and velocity measurement in a radial flow fixed bed reactor using electrical resistance tomography. Chem. Eng. Sci. 59, 1989–1997.

Buyevich, Y.A., and Kapbasov, S.K. (1999). Particulate Pressure in Disperse Flow. Int. J. Fluid Mech. Res. 26, 72–97.

Buyevich, Yu.A. (1971). On the fluctuations of concentration in disperse systems The random number of particles in a fixed volume. Chem. Eng. Sci. 26, 1195–1201.

Buyevich, Yu.A. (1997). Particulate pressure in monodisperse fluidized beds. Chem. Eng. Sci. 52, 123–140.

Buyevich, Yu.A., and Kapbasov, Sh.K. (1994). Random fluctuations in a fluidized bed. Chem. Eng. Sci. 49, 1229–1243.

Campbell, C.S. (2006). Granular material flows – An overview. Powder Technol. 162, 208–229.

Carnahan, N.F., and Starling, K.E. (1969). Equation of State for Nonattracting Rigid Spheres. J. Chem. Phys. 51, 635–636.

Cheng, Y., and Zhu, J.-X. (Jesse). (2005). CFD Modelling and Simulation of Hydrodynamics in Liquid-Solid Circulating Fluidized Beds. Can. J. Chem. Eng. 83, 177–185.

Cook, M.V. (2012). Flight Dynamics Principles: A Linear Systems Approach to Aircraft Stability and Control (Butterworth-Heinemann).

Cornelissen, J.T., Taghipour, F., Escudié, R., Ellis, N., and Grace, J.R. (2007). CFD modelling of a liquid–solid fluidized bed. Chem. Eng. Sci. 62, 6334–6348.

Costigan, G., and Whalley, P.B. (1997). Slug flow regime identification from dynamic void fraction measurements in vertical air-water flows. Int. J. Multiph. Flow 23, 263–282.

Del Pozo, M., Briens, C.L., and Wild, G. (1993). Particle-particle collisions in liquid-solid and gas-liquid-solid fluidized beds. Chem. Eng. Sci. 48, 3313–3319.

Derksen, J.J., and Sundaresan, S. (2007). Direct numerical simulations of dense suspensions: wave instabilities in liquid-fluidized beds. J. Fluid Mech. 587.

Dickin, F., and Wang, M. (1996). Electrical resistance tomography for process applications. Meas. Sci. Technol. 7, 247–260.

Didwania, A.K., and Homsy, G.M. (1981). Flow regimes and flow transitions in liquid fluidized beds. Int. J. Multiph. Flow 7, 563–580.

Dong, F., Jiang, Z.X., Qiao, X.T., and Xu, L.A. (2003). Application of electrical resistance tomography to two-phase pipe flow parameters measurement. Flow Meas. Instrum. 14, 183–192.

Doroodchi, E., Galvin, K.P., and Fletcher, D.F. (2005). The influence of inclined plates on expansion behaviour of solid suspensions in a liquid fluidised bed—a computational fluid dynamics study. Powder Technol. 156, 1–7.

Drew, D.A. (1983). Mathematical Modeling of Two-Phase Flow. Annu. Rev. Fluid Mech. 15, 261–291.

Dyakowski, T., Jeanmeure, L.F.C., and Jaworski, A.J. (2000). Applications of electrical tomography for gas-solids and liquid-solids flows-a review. Powder Technol. 112, 174–192.

El-Kaissy, M.M., and Homsy, G.M. (1976). Instability waves and the origin of bubbles in fluidized beds: Part 1: Experiments. Int. J. Multiph. Flow 2, 379–395.

Epstein, N. (2002). Applications of Liquid-Solid Fluidization. Int. J. Chem. React. Eng. 1, 1–16.

Fangary, Y.S., Williams, R.A., Neil, W.A., Bond, J., and Faulks, I. (1998). Application of electrical resistance tomography to detect deposition in hydraulic conveying systems. Powder Technol. 95, 61–66.

Fischer, A., König, J., and Czarske, J. (2008). Speckle noise influence on measuring turbulence spectra using time-resolved Doppler global velocimetry with laser frequency modulation. Meas. Sci. Technol. 19, 125402.

Fox, R.O. (2014). On multiphase turbulence models for collisional fluid–particle flows. J. Fluid Mech. 742, 368–424.

George, D.L., Torczynski, J.R., Shollenberger, K.A., O'Hern, T.J., and Ceccio, S.L. (2000). Validation of electrical-impedance tomography for measurements of material distribution in two-phase flows. Int. J. Multiph. Flow 26, 549–581.

Gevrin, F., Masbernat, O., and Simonin, O. (2008). Granular pressure and particle velocity fluctuations prediction in liquid fluidized beds. Chem. Eng. Sci. 63, 2450–2464.

Gevrin, F., Masbernat, O., and Simonin, O. (2010). Numerical study of solid–liquid fluidization dynamics. AIChE J. 56, 2781–2794.

Gibilaro, L., Foscolo, P., and Felice, R.D. (1990). The Velocity of Dynamic Waves in Fluidised Beds. In Two Phase Flows and Waves, (Springer, New York, NY), pp. 56–69.

Gidaspow, D. (1994). Multiphase Flow and Fluidization: Continuum and Kinetic Theory Descriptions (Academic Press).

Gidaspow, D., Jung, J., and Singh, R.K. (2004). Hydrodynamics of fluidization using kinetic theory: an emerging paradigm. Powder Technol. 148, 123–141.

Ham, J.M., Thomas, S., Guazzelli, E., Homsy, G.M., and Anselmet, M.-C. (1990). An experimental study of the stability of liquid-fluidized beds. Int. J. Multiph. Flow 16, 171–185.

Hashemi, S.A. (2013). Velocity and concentration fluctuations in concentrated solid-liquid flows. PhD thesis. University of Alberta.

Hashemi, S.A., Sadighian, A., Shah, S.I.A., and Sanders, R.S. (2014). Solid velocity and concentration fluctuations in highly concentrated liquid–solid (slurry) pipe flows. Int. J. Multiph. Flow 66, 46–61.

Hrenya, C.M., and Sinclair, J.L. Effects of particle-phase turbulence in gas-solid flows. AIChE J. 43, 853–869.

Huilin, L., Gidaspow, D., and Manger, E. (2001). Kinetic theory of fluidized binary granular mixtures. Phys. Rev. E 64, 061301.

Industrial Tomography Systems (2014). ITS Tomography Toolsuite v7.32 User's manual (Manchester, UK: Industrial Tomography Systems Plc).

Ishida, M., and Tanaka, H. (1982). An optical probe to detect both bubbles and suspended particles in a three-phase fluidized bed. J. Chem. Eng. Jpn. 15, 389–391.

Ismail, I., Gamio, J.C., Bukhari, S.F.A., and Yang, W.Q. (2005). Tomography for multi-phase flow measurement in the oil industry. Flow Meas. Instrum. 16, 145–155.

Issangya, A.S., Grace, J.R., Bai, D., and Zhu, J. (2000). Further measurements of flow dynamics in a high-density circulating fluidized bed riser. Powder Technol. 111, 104–113.

Jia, J., Wang, M., and Faraj, Y. (2014). Evaluation of EIT systems and algorithms for handling full void fraction range in two-phase flow measurement. Meas. Sci. Technol. 26, 015305.

Jones, O.C., and Delhaye, J.-M. (1976). Transient and statistical measurement techniques for two-phase flows: A critical review. Int. J. Multiph. Flow 3, 89–116.

Kato, Y., Uchida, K., Kago, T., and Morooka, S. (1981). Liquid holdup and heat transfer coefficient between bed and wall in liquid solid and gas-liquid-solid fluidized beds. Powder Technol. 28, 173–179.

Kechroud, N., Brahimi, M., and Djati, A. (2010). Characterization of dynamic behaviour of the continuous phase in liquid fluidized bed. Powder Technol. 200, 149–157.

Koch, D.L. (1990). Kinetic theory for a monodisperse gas-solid suspension. Phys. Fluids A 2, 1711–1723.

Kotre, C.J. (1994). EIT image reconstruction using sensitivity weighted filtered backprojection. Physiol. Meas. 15, A125–A136.

Kraichnan, R.H. (1967). Inertial Ranges in Two-Dimensional Turbulence. Phys. Fluids 10, 1417–1423.

Kremer, D.M., and Hancock, B.C. (2006). Process Simulation in the Pharmaceutical Industry: A Review of Some Basic Physical Models. J. Pharm. Sci. 95, 517–529.

Kumar, S.B., Moslemian, D., and Dudukovic, M.P. (1996). A gamma-ray tomographic scanner for imaging voidage distribution in two-phase flow systems. Int. J. Multiph. Flow 22, 108.

Lee, S.L.P., and Lasa, H.I. de (1987). Phase holdups in three-phase fluidized beds. AIChE J. 33, 1359–1370.

Lemmin, U., Scott, J.T., and Czapski, U.H. (1974). The development from two-dimensional to three-dimensional turbulence generated by breaking waves. J. Geophys. Res. 79, 3442–3448.

Lettieri, P., Di Felice, R., Pacciani, R., and Owoyemi, O. (2006). CFD modelling of liquid fluidized beds in slugging mode. Powder Technol. 167, 94–103.

Lilly, D.K. (1969). Numerical Simulation of Two-Dimensional Turbulence. Phys. Fluids 12, II–240.

Limtrakul, S., Chen, J., Ramachandran, P.A., and Duduković, M.P. (2005). Solids motion and holdup profiles in liquid fluidized beds. Chem. Eng. Sci. 60, 1889–1900.

Lowe, D.C., and Rezkallah, K.S. (1999). Flow regime identification in microgravity two-phase flows using void fraction signals. Int. J. Multiph. Flow 25.

Luo, L.-S. (1998). Unified Theory of Lattice Boltzmann Models for Nonideal Gases. Phys. Rev. Lett. 81, 1618–1621.

Marefatallah, M., Breakey, D., and Sanders, R.S. (2019a). Experimental Study of Local Solid Volume Fraction Fluctuations in a Liquid Fluidized Bed: Particles with a wide range of Stokes numbers, *in preparation for submission*.

Marefatallah, M., Breakey, D., and Sanders, R.S. (2019b). Study of local solid volume fraction fluctuations using high speed electrical impedance tomography: Particles with low Stokes number. Chem. Eng. Sci. 203, 439–449.

Masliyah, J., Zhou, Z.J., Xu, Z., Czarnecki, J., and Hamza, H. (2004). Understanding Water-Based Bitumen Extraction from Athabasca Oil Sands. Can. J. Chem. Eng. 82, 628–654.

Norman, J.T., and Bonnecaze, R.T. (2005). Measurement of Solids Distribution in Suspension Flows using Electrical Resistance Tomography. Can. J. Chem. Eng. 83, 24–36.

Ozel, A., Brändle de Motta, J.C., Abbas, M., Fede, P., Masbernat, O., Vincent, S., Estivalezes, J.-L., and Simonin, O. (2017). Particle resolved direct numerical simulation of a liquid–solid fluidized bed: Comparison with experimental data. Int. J. Multiph. Flow 89, 228–240.

Panneerselvam, R., Savithri, S., and Surender, G.D. (2007). CFD based investigations on hydrodynamics and energy dissipation due to solid motion in liquid fluidised bed. Chem. Eng. J. 132, 159–171.

Pope, S.B. (2000). Turbulent Flows (Cambridge University Press).

Reddy, R.K., and Joshi, J.B. (2009). CFD modeling of solid–liquid fluidized beds of mono and binary particle mixtures. Chem. Eng. Sci. 64, 3641–3658.

Renganathan, T., and Krishnaiah, K. (2005). Voidage characteristics and prediction of bed expansion in liquid–solid inverse fluidized bed. Chem. Eng. Sci. 60, 2545–2555.

Roy, S., and Dudukovic, M.P. (2001). Flow Mapping and Modeling of Liquid−Solid Risers. Ind. Eng. Chem. Res. 40, 5440–5454.

Sanders, R.S., Ferre, A.L., Maciejewski, W.B., Gillies, R.G., and Shook, C.A. (2000). Bitumen effects on pipeline hydraulics during oil sand hydrotransport. Can. J. Chem. Eng. 78, 731–742.

Sergeev, Y.A., Swailes, D.C., and Petrie, C.J.S. (2004). Stability of uniform fluidization revisited. Phys. Stat. Mech. Its Appl. 335, 9–34.

Sommeria, J., and Moreau, R. (1982). Why, how, and when, MHD turbulence becomes two-dimensional. J. Fluid Mech. 118, 507–518.

Tarleton, S., and Wakeman, R. (2005). Solid/ Liquid Separation: Principles of Industrial Filtration (Elsevier).

Thais, L., and Magnaudet, J. (1996). Turbulent structure beneath surface gravity waves sheared by the wind. J. Fluid Mech. 328, 313–344.

Van Wachem, B.G.M., and Almstedt, A.E. (2003). Methods for multiphase computational fluid dynamics. Chem. Eng. J. 96, 81–98.

Wang, M. (2002). Inverse solutions for electrical impedance tomography based on conjugate gradients methods. Meas. Sci. Technol. 13, 101–117.

Wang, M., Ma, Y., Holliday, N., Dai, Y., Williams, R.A., and Lucas, G. (2005). A high-performance EIT system. IEEE Sens. J. 5, 289–299.

Wei, K., Qiu, C., Soleimani, M., and Primrose, K. (2015). ITS Reconstruction Tool-Suite: An inverse algorithm package for industrial process tomography. Flow Meas. Instrum. 46, 292–302.

Xia, B., and Sun, D.-W. (2002). Applications of computational fluid dynamics (CFD) in the food industry: a review. Comput. Electron. Agric. 34, 5–24.

Yamazaki, H., Tojo, K., and Miyanami, K. (1992). Measurement of local solids concentration in a suspension by an optical method. Powder Technol. 70, 93–96.

York, T.A. (2001). Status of electrical tomography in industrial applications. J. Electron. Imaging 10, 608–620.

Zenit, R., and Hunt, M.L. (1999). Mechanics of Immersed Particle Collisions. J. Fluids Eng. 121, 179.

Zenit, R., and Hunt, M.L. (2000). Solid fraction fluctuations in solid–liquid flows. Int. J. Multiph. Flow 26, 763–781.

Zenit, R., Hunt, M.L., and Brennen, C.E. (1997). Collisional particle pressure measurements in solid-liquid flows. J. Fluid Mech. 353, 261–283.

Zhang, K., Wu, G., Brandani, S., Chen, H., and Yang, Y. (2012). CFD simulation of dynamic characteristics in liquid–solid fluidized beds. Powder Technol. 227, 104–110.

Zhu, K., Madhusudana Rao, S., Wang, C.-H., and Sundaresan, S. (2003). Electrical capacitance tomography measurements on vertical and inclined pneumatic conveying of granular solids. Chem. Eng. Sci. 58, 4225–4245.

Appendix A. EIT measurements: Spatial resolution, measurement variance, and validation

A.1. Packed bed measurements

For each particle type tested in this study, the time-averaged solid fraction map of a packed bed of particles was measured. For these measurements the fluidized bed was filled with water (with the appropriate salt addition for each type of particle) and then particles were added up to the height of 150 cm from the bottom screen. The pump was operated at 20 RPM for 10 to 15 minutes to disengage all air bubbles from the bed. The pump was then switched off and 15 minutes later, measurements were made. Figure A.1 illustrates the time-averaged solid fraction maps for each of the four particle types at packed bed conditions. As shown in this figure the distribution of the particles over the bed cross-section is uniform as expected and the solid fraction at each pixel is very close to the expected values of 0.6 (C_{max} for the mono-sized spherical particles).

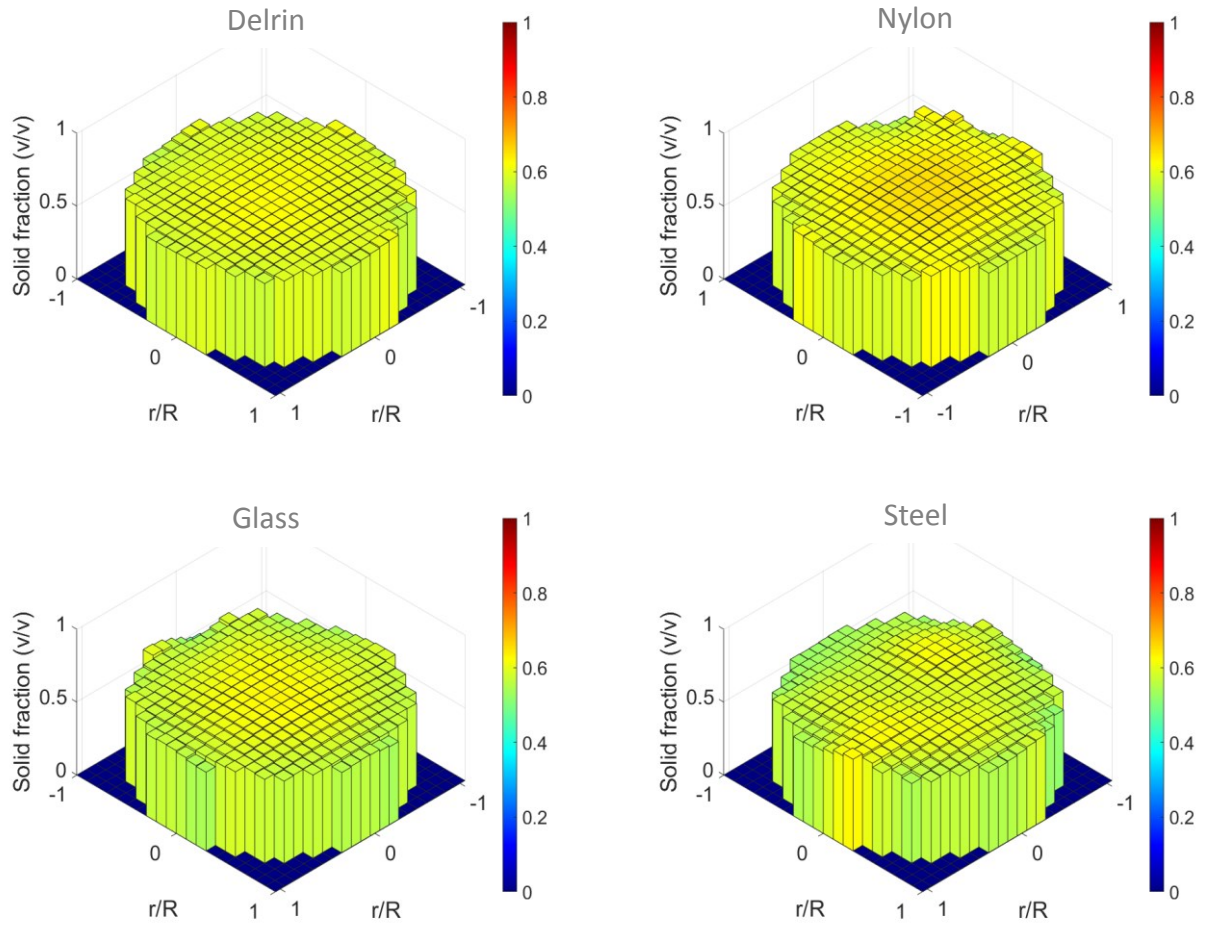

Figure A.1. Time-averaged solid fraction maps for the packed of four particle types

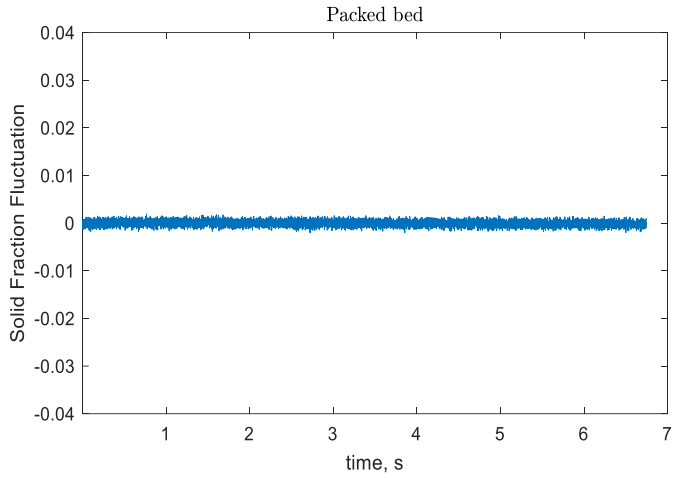

Figure A.2. Cross-sectional averaged solid fraction fluctuations, $C - \overline{C}$, for the packed bed of Delrin particles. In this graph, the global averaged and the standard deviation are $\overline{C}$=0.5999 and 6.1399e-04, respectively.

In order to analyze the magnitude of the measurement error, the standard deviation of the cross-sectional averaged solid fraction of the packed beds was also calculated. Figure A.2. shows the solid fraction fluctuations of a packed bed of Delrin particles. Since the packed bed was stationary the recorded values represent the measurement error. A comparison between the amplitudes of the fluctuations in Figure A.2 and the results shown in Figures 2.4 and 2.7 shows that the error in the measurement of solid fraction fluctuations was sufficiently small.

A.2. EIT spatial resolution

In Chapter 2, the EIT reconstruction grid was discussed and the grid map was shown in Figure 2.2. Since the bed diameter is 101.6 mm and the size of each EIT electrode mounted on the bed periphery is 10 mm by 10 mm, each EIT 3D pixel size is 5.08 x 5.08 x 10 mm (width x length x height). The diameter of the spherical particles used in this study ranged from 3.34 mm to 6 mm which are close to the EIT pixel dimensions.

A.3. Spatial variance of measurements

In Figures 2.3 and 3.3 the local RMS solid volume fraction fluctuations at different bulk solid fractions for four particle types were shown. These figures show that the azimuthal distribution

of the RMS fluctuations is not uniform especially at regions closer to the wall. In some cases large RMS peaks are also observed in this region. This non-uniform distributions may be due to measurement artifacts. To investigate this further, the same RMS maps shown in Figures 2.3 and 3.3 are further analyzed to obtain the spatial variance of the RMS distribution in the azimuthal direction at each radial position (Figure A.3). Figure A.4 demonstrates the relative standard deviations (RSD) of RMS fluctuations as a function of radial position. At each radial position the relative standard deviation is calculated as:

$$\text{Relative standard deviation } \left({}^{r}/_{R}\right) = \frac{\text{standard deviation of RMS fluctuations in azimuthal direction } \left({}^{r}/_{R}\right)}{\text{mean of RMS fluctuations in azimuthal direction } \left({}^{r}/_{R}\right)}$$

For Delrin and nylon particles the RSD was higher at the r/R=0.95 compared to the rest of the bed cross-section. RSD values for glass and steel particles did not follow this trend, i.e. regions near the wall did not show significantly higher RSD values. Larger error bars in Figure A.3.c for glass particles show that the distribution of the RMS in azimuthal direction was more variable over time compared to the other particles.

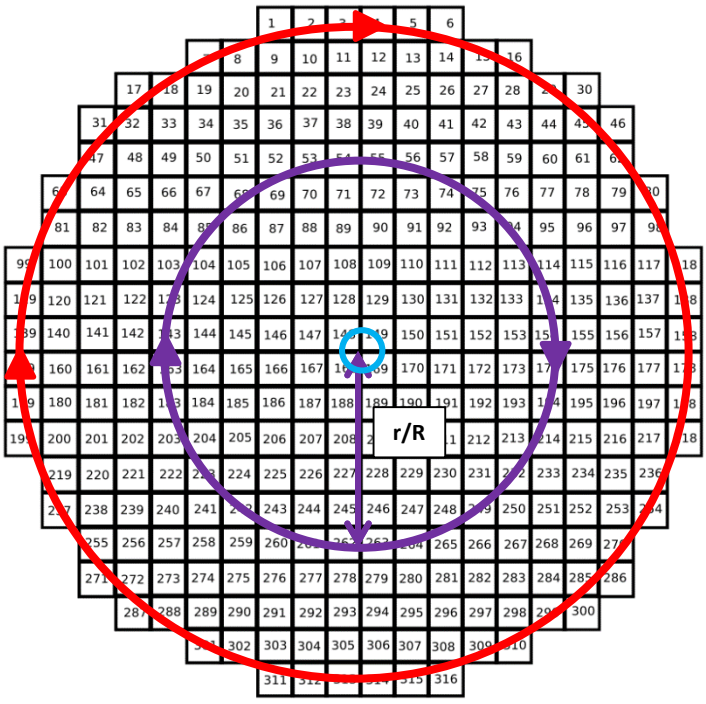

Figure A.3. Azimuthal direction at each radial position (r/R)

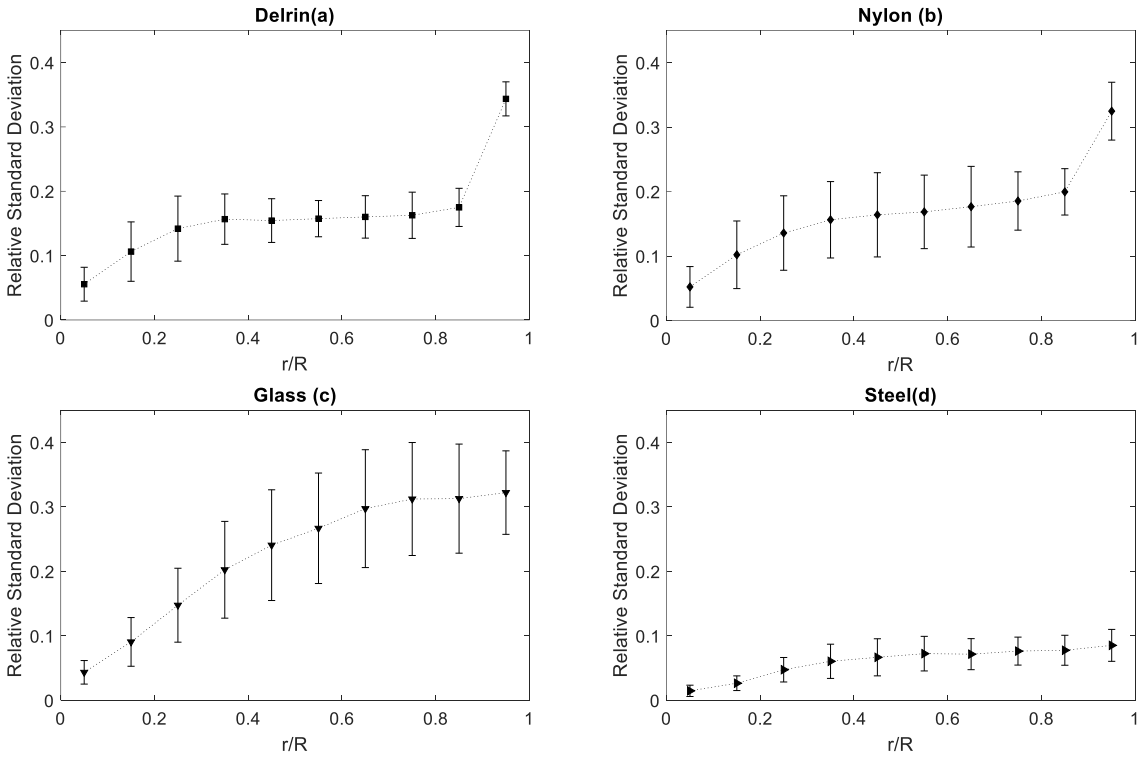

Figure A.4. Relative standard deviations (RSD) of RMS solid fraction fluctuations in azimuthal direction. (a) Delrin at $\overline{C}$ = 0.31, (b) Nylon at $\overline{C}$ = 0.30, (c) Glass at $\overline{C}$ = 0.54, and (d) Steel at $\overline{C}$ = 0.44. Error bars represent standard deviation of RSDs over 10 repeats.

This figure helps describe the uniformity of the RMS fluctuations presented in this study in the azimuthal direction at various radial positions. Lower RSD values represent more uniform distributions. The results shown in Figure A.4 suggest that the RMS fluctuations for steel particles are more uniformly distributed in azimuthal direction compared to the other particles.

The trend of the RSD curves varies for different particles. For instance the RSD values for glass and steel particles at the near the wall region is not different than that of the rest of the bed cross-section. Therefore, the azimuthal distributions of the RMS fluctuations (shown in Figures 2.3 and 3.3) are not dominated by measurement setup artifacts, and are rather more affected by the particle properties or fluidization condition. In the absence of significant measurement artifacts the increase in the magnitude of the RMS fluctuations at the wall zone is likely due to the particle–wall collisions being dominant in this region. This is consistent with the discussions presented in Chapters 2–4.